2010

Experimental study of inhomogeneous deformation in bulk metallic glass and their composite during wedge-like cylindrical indentation

Hui Wang
Iowa State University

Experimental study of inhomogeneous deformation in bulk metallic glass and their composite during wedge-like cylindrical indentation

by

Hui Wang

A dissertation submitted to the graduate faculty

in partial fulfillment of the requirements for the degree of

DOCTOR OF PHILOSOPHY

Major: Engineering Mechanics

Program of Study Committee:
Ashraf Bastawros (Major Professor)
Valery Levitas
Thomas Rudolphi
Alan Russell
Ersan Ustungdag

Iowa State University

Ames, Iowa

2010

To my parents, Jia and Tianrui

TABLE OF CONTENTS

LIST OF FIGURES

LIST OF TABLE

ACKNOWLEDGEMENTS

I would like to take this opportunity to express my thanks to those who helped me with various aspects of conducting research and the writing of dissertation.

I want to appreciate my major professor, Dr. Ashraf Bastawros for his guidance, support and encouragement during my graduate studies at Iowa State University. With his patience, he introduced me a new and exciting field and made me understand how to be a researcher and how to enjoy the frustrating period in my research. It was his encouragement that made me to become more confident and more interest in the micro- and nano- world. The most I want to thank him is his generous support, not only for my research but also for my family. Without his wise advice, I would not stay here with my family and finish my study. I will remember and treasure the knowledge and wisdom that he gave me in my following career and life.

I would also like to thank Dr. Tom Rudophi, Allan Russell, Ersan Ustungdag and Valery Levitas to be my research committees. I learned a lot from their classes. Dr. Rudophi taught me the most important class, continuum mechanics in my graduate study and also his helpful discussions always showed me brightness. Dr. Russell taught me the first material science class and I want to thank him for every moment that he took to help me in his office hour. Dr. Ustungdag taught me the second material science class and help me to expand my understanding about mechanical behavior from material structure aspect. Such wealth of knowledge were greatly helpful in my later research. Also, I would like to appreciate Dr. Levitas. He gave me many valuable advices during my defense.

Finally, I would like to thank my family, my parents, my husband and my lovely son. I appreciate my parents' endless love and encouragement. Especially the most important one is my husband who shared my sadness, frustration, happiness, excitement and everything. It was his accompaniment, support and understanding that I am still standing here today. I thank my son, because he had brought us unexpected happiness and made me brave.

ABSTRACT

Bulk metallic glasses (BMGs) are amorphous metals with impressive mechanical properties, such as high elastic strain up to 2%, high strength (up to 2% of Young's modulus) and high hardness. Their weight normalized properties exceed the high strength to weight ratio of titanium alloys. Because of the lack of crystalline defects such as grain boundaries and dislocations, they have good corrosion resistance and good formability. The unique die molding properties of BMGs render them as excellent candidates for micro-scale machine parts, pressure sensor, golf clubs and casings. BMG's also exhibit enhanced plastic creep resistance, since homogeneous plastic deformation is inhibited at room temperature. Below the glass transition temperature, BMGs exhibit inhomogeneous plastic flow through the formation of localized shear bands. Under unconfined loading geometry, BMGs fails in a brittle material manner with unstable propagation of a single shear band. However, under confined geometry, BMG's show increased ductility due to the ability to nucleate and propagate multiple shear bands.

This dissertation focuses on experimentally analyzing evolution and propagation of the shear bands in BMGs and their composites, by monitoring the deformation mechanisms at the scale of the shear band under confined geometry. Wedge-like cylindrical indentation has been used to provide a stable loading configuration for in-situ observation of the inhomogeneous deformation zone underneath the indenter. High resolution digital camera has been employed to capture surface images of the evolution of the process-zone. An in-house digital image correlation (DIC) program has been developed, utilizing MATLAB commercial software, to calculate the in-plane finite strain distribution at the scale of the

shear band. First, the plastic deformation and flow field under the indenter are studied in both aluminum and copper alloys with different grain sizes to verify and validate the analysis protocol. The measured plastic zone size is comparable with the one predicted by the simplified cavity model and there is a unique correlation of the strain distribution along the radial line with different angular positions originating from the indentation center. The deformation zones developed under indenters with different radii are found to be self-similar. In the elastic domain, the measured strain distribution agree with FEM predictions; in the elastic-plastic domain, extra hardening is observed, which could be the result of constrained deformation.

Second, the inhomogeneous deformation behavior of Vitreloy-1 bulk metallic glass is examined at room temperature. To overcome the resolution limit of the DIC technique to resolve the strain within a single shear band having 10-20nm width, an alternative method is implemented, addressing the strain jump within the band and the surrounding matrix. The results show that the BMG can deform homogenously to a large elastic strain level of about 4-6% before the onset of inhomogeneous deformation via localized shear bands. Such observation indicates the ability of BMG to withstand such high levels of stresses and strains if unstable shear band can be suppressed from the nucleation from the surface, such as the case of tension or bending. Following the perturbation analysis of Hwang et al (2004) and utilizing the same material parameters, it is found that homogenous nucleation strain is of the same order. The experimental measurements show more subtle details about the kinematics of shear band propagations. The shear band propagates intermittently at the expense of the surrounding matrix stored elastic strain energy. The surrounding matrix ceases to deform,

during the activity of the shear band, however, no unloading is observed. The accumulated strain level inside of the shear band is about 3 orders higher than the one in the surrounding matrix. By tracking the strain increments of a single shear band and its surrounding matrix, the deformation filed has been shown to be self-similar, within the surrounding matrix. While the stress state at the observation point is defined by the global indentation filed, the local stress state within the shear band is a simple shear state, with respect to the band propagation direction. Relative to the band-propagation direction and the corresponding normal, the surrounding matrix deforms in a pure shear-state to accommodate shear band deformation.

The experimental protocol is also utilized to study the kinematics of shear band initiation, propagation and arrest or hindrance by a secondary ductile phase. The deformation mechanisms in BMG composite with brass particles are examined. The composite is manufactured by warm extrusion of a mix of gas atomized powders of Ni-based BMG and brass. The resulting composite has an elongated particulate structure in the extrusion direction. The fracture toughness and toughening mechanism of the BMG composites are examined in the parallel and normal directions to the extrusion axis. This composite shows highly anisotropic properties along different loading directions. For the normal direction loading, brass reinforcements not only trigger the initial localized shear band, but also modify the crack propagation by crack bridging mechanisms. Also, microcracking is another important toughening mechanism. For the parallel direction loading, interface debonding is the main failure mechanism. Using FEM simulations, it is shown that local fracture is strain-controlled along the normal loading direction and stress controlled along the parallel loading direction.

The proposed experimental framework is further extended for fracture match applications in forensic science. The likelihood of matching broken pieces, wherein a macroscopic crack trajectory cannot be established is analyzed via spectral analysis of the 3D fracture surfaces. The surface topographies are acquired using a non-contact 3D optical surface profilometer. A quantitative signature of the fracture surface, employing the different length scales of the fracture process zone is derived and used to establish class and sub-class matching. The details of the algorithm and its applications are detailed in the Appendix.

CHAPTER 1: INTRODCUTION

Metallic glass also known as amorphous metals was first produced in the form of a thin ribbon by splat quenching of Au-Si alloys in the 1960's [1]. A number of amorphous metals had been produced [2-6] with mechanical strength that was much higher than that of microcrystalline alloys [7-9]. Following the development of bulk metallic glasses (BMGs), a wide range of mechanical characterization were conducted under different conditions. Because of the lack of crystalline defects such as grain boundaries and dislocations, BMGs show extraordinary mechanical properties, corrosion resistance [10] and good formability.

1.1 BULK METALLIC GLASS AND COMPOSITE

The most impressive advantage of BMGs' mechanical property is their high elastic strain of 2% under unconfined tensile loading [11, 12], high strength (up to 2% of Young's modulus) and high hardness [9]. In Vitreloy 1 ($Zr_{41.25}Ti_{13.75}Cu_{12.5}Ni_{10}Be_{22.5}$), for example, the tensile yield strength is 1.9 GPa and Young's modulus is 96 GPa [13]. The fracture toughness values of Zr-based[14], Cu-based[15], Ti-based[16] and Pd-based[17] glasses are higher (45-85 MPa$\sqrt{m}$) than that of Fe-based[18] or Mg-based [16] glasses (2-4 MPa$\sqrt{m}$). Though, BMGs fracture catastrophically by highly localized shear band in unconfined geometries at ambient temperature, such as uniaxial tension or compression [19, 11, 12]. Fig.1.1 presents some typical stress-strain relation of BMG under uniaxial tension or compression tests with different loading rates at room temperature. It shows that an increased strain rate leads to enhanced ductility in tension and compression [20]. For the BMG deformation behavior, an empirical deformation map has been developed [21], classifying

BMG flow as homogenous and inhomogeneous. The homogenous flow occurs at low stresses and high temperature [22]. Inhomogeneous flow is seen at high stress and low temperatures, where the plastic deformation tends to be highly localized into narrow shear bands as show in Fig.1.2 [23]. The macroscopic observations also showed asymmetric deformation behavior between tensile and compressive loading [11] with moderate pressure dependent macroscopic yielding behavior [24-27]. Under geometric confinement, the BMG deformation exhibit increased ductility, accompanied with stable shear bands propagation. Especially under inhomogeneous loading conditions during ribbon bending [28], crack tip behavior [29] and indentation field, either in 2D [30, 27] or 3D [31, 24, 32].

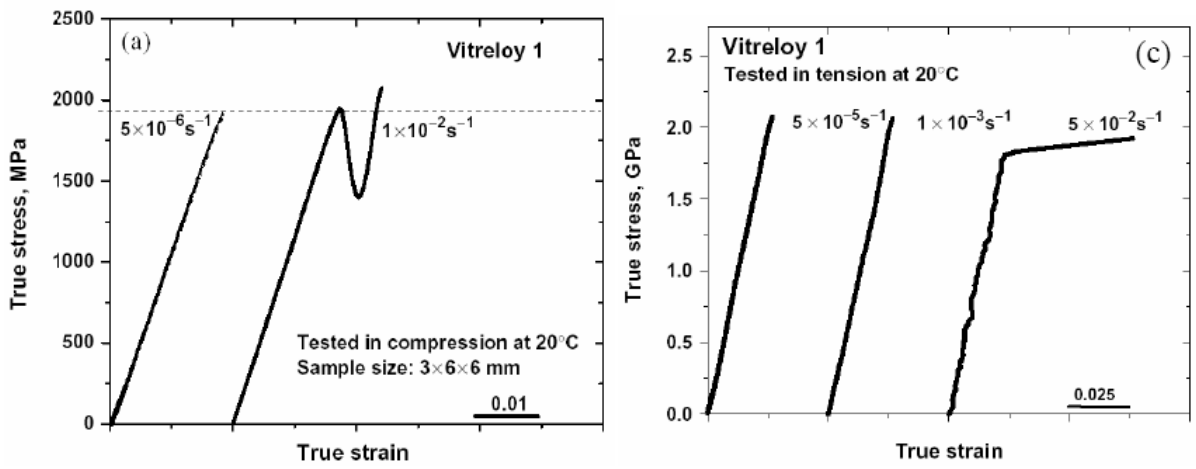

Figure 1.1 True stress-true strain compression and tension curves of alloys at room temperature and at different strain rate.[20]

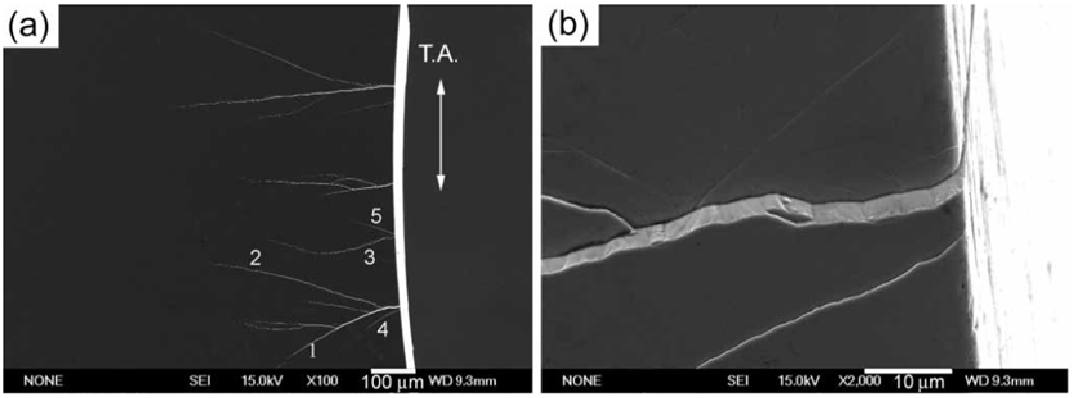

Figure 1.2 Shear bands on the surface of bulk MGs deformed in tension. [23]

To circumvent the limited ductility of BMG alloys, the concept of introducing second phase particles with different length scale into a glassy matrix has developed recently [33-35]. Macroscopic ductility has been observed when the BMG matrix is reinforced with a ductile metal [36-38]. BMG composites can be prepared by similar procedures as those of BMGs, such as, through mechanical alloying and consolidation [39], solidification [5,6] or partial devitrification of amorphous precursors by either thermal treatment [40-42] or severe plastic deformation/high pressure torsion [43,44]. The various processing routes and the evolution of BMG composites with different length scales of second phases are schematically described in Fig.1.3. The microstructures of BMG composites can be classified in two groups: ex situ and in situ formed composites. The length scale of the ex situ composites varies from micrometer to nanometer and these composites consist of either particle [45,36,46,47] or fiber reinforcements (continuous or discontinuous fibers) [47,48,37,49,50]. The microstructure of in situ BMG composites has different shape and size, as shown in Fig. 1.4. Typically, the in situ composites have higher ductility, fracture toughness and fatigue endurance [38,51,52]. It has been observed that the shear bands can transverse the ductile

reinforcement [52], which also would inhibit the propagation of localized shear bands within the BMG. The size and volume fraction of the reinforcements also play an important role on the incremental ductility of BMG composite [36,37].

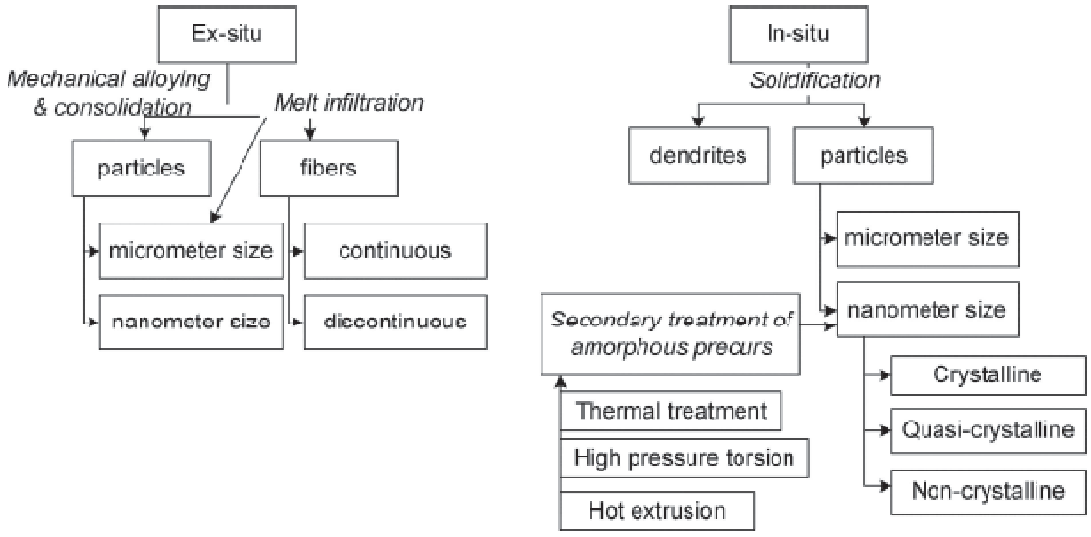

Figure 1.3 different processing routes for obtaining bulk metallic glass matrix composite. [53]

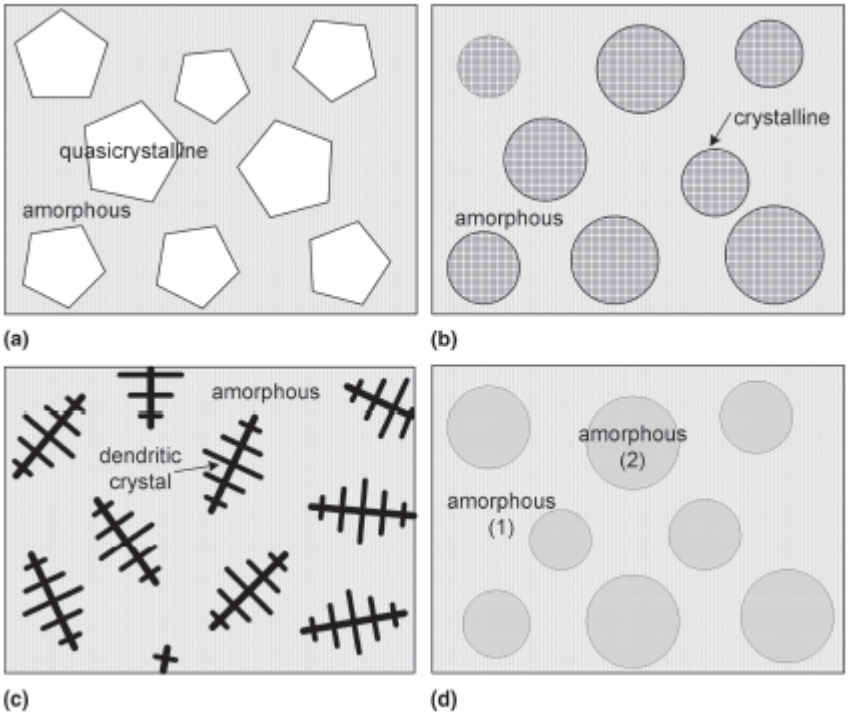

Figure 1.4 schematic representations of microstructures of in situ composite with different second phase dispersions and different length scale with (a) qusicrystalline phase, (b) spherical shaped nano-micrometer-sized crystals, (c) dendritic phase, and (d) two phase amorphous.[53]

1.2 MOTIVATION

The microscopic plastic deformation mechanism of crystalline materials is about the dislocation motion. However, in amorphous metallic glasses, the plastic deformation is fundamentally different to that in crystalline solids because of the lack of long-range order in the atomic structure of these materials. The microscopic mechanisms of the BMG inhomogeneous deformation is phenomenological viewed as a cooperative behavior of small clusters of randomly closed-packed atoms, so called shear transformation zones (STZs) [54]. The STZs are thought to create a localization of displacements in surrounding regions (30~50 atoms) that triggers the evolution of highly localized shear bands during the deformation by

creation of free volume [54]. Such phenomenological view has been further corroborated by molecular dynamic (MD) simulations [55]. In continuum modeling, the free volume is considered to evolve with the applied stress [21]. The BMG plastic flow will occur when the free volume created by the applied stress exceeds the annihilation/diffusion rates. This microscopic view is generalized by Steif *et al*. 1982 [56] , Huang *et al*. 2002 [57] and among many others, to describe the initiation and propagation of shear bands. Transmission Electron Microscopy (TEM) analysis of the shear bands have indeed shown that the amount of voids has increased within a shear band, relative to surroundings [58]. Realizing the differences in length scales between TEM observations, MD simulation and the continuum description of shear band nucleation and propagations, there is a lack in experimental observation of the microscopic deformation evolution for shear bands in BMG.

Therefore, the goal of current research is to understand BMG inhomogeneous deformation evolution over the plastic deformation field and microscopic deformation evolution of single shear band, by experimental measurements and the numerical analysis.

1.3 IMPLEMENTATION PLAN

Wedge-like Cylindrical Indentation

BMG shows some degree of ductility under the confined geometry conditions, which include indentation tests. Various indentation techniques have been fully developed in the past 100 years with widespread use in characterizing the mechanical properties of different materials through hardness measurements. Due to the constrained stress states of the field underneath the indenter, it provides a stable and non-destructive mean to measure the

resistance of a material to plastic deformation. However, the geometrical versatility and complicate strain field under the indenter make it difficult to interpret the force indentation depth measurements into stress-strain relations in a straight-forward way. A number of investigators have pursued the relationship between the mean contact pressure and the macroscopic yield strength of materials by the development of analytical models such as Cavity Expansion model and all kind of experimental measurements. With the advanced instruments invention, the indentation technique has been applied into a wide range of length scales and on different materials, and then more explanations about the indentation have been addressed. A series of experimental techniques like sectioning, etching and micro hardness survey have been utilized to explore the plastic deformation zone under the indenter on various kind of materials, such as single crystal, polycrystalline metals and alloys, and even amorphous bulk metallic glasses. However, the complex strain filed and the evolution of heterogeneous deformation under the indenter still needs a clear statement.

A newly developed experimental methodology [30] has been adapted, which ensures the in-situ observation of the plastic zone evolution and simultaneously imaging records. This research is about an experimental study of the evolution of inhomogeneous deformation field underneath a wedge-like cylindrical indentation, in which the plastic flow characterization and localization evolution will be thoroughly discussed.

Digital Image Correlation Technique (DIC)

Digital Image Correlation (DIC) technique was first proposed and has been developed since early 1980s to compute the surface strains and displacements [59]. DIC technique is

computer based and non-contact measuring full-field surface strains that has been demonstrated to be robust, flexible, applicable to large deformation and over a wide range of size scales and very affordable. The resolution of the measurements is determined by two main factors, those are the magnification of the acquisition system and the characteristics of the image sensing element. The underlying principle of digital image correlation as a deformation measurement technique is not difficult, which provides estimates of the displacement field by correlating the features in a pair of digital images of a specimen surface before and after deformation by a mathematically well-defined function.

Digital image correlation has been used either as a noncontact strain gauge technique to measure the average strains of macroscopically uniform deformation [60,61], or as a whole-field deformation mapping tool to measure highly nonuniform deformation fields such as the ones surrounding a crack tip or perforation [62,63]. The versatility of this technique even includes velocity-field measurement of seeded fluid [64], characterization of soil surface layer cracking [65], detection of plastic deformation patterns in aluminum alloy [66], reliability of microelectronic packages[67] and compression strain measurement of aluminum alloy foams [68].

In this work, an in-house MATLAB program about digital image correlation method has been developed, which is based on subset methodology [69,70]. By this technique, we developed the average measurements that show the strain distribution inside of the plastic deformation zone and also individual measurements that show the strain value evolution inside of the single localization band.

Characterization of Plastic Flow in Ductile Metals by DIC

Ductile metals such as copper and aluminum alloys as typical crystalline metals have been studied by indentation technique for many years. The underlying principle is to correlate the average contact pressure or "hardness" to the flow stress [71,72] and modulus [73] of the material. Despite the improved resolution and accuracy of the indentation technique [74], the details of elastic-plastic process zone remained to be explored via finite element analysis, employing phenomenological constitutive relations and hinges upon macroscopic matching of the force-depth indentation curves [75-77]. Limited details of the deformation field underneath the indenter have been reported via sectioning a macroscopic indentation [78,79] or indent a bonded interface [78], and then reveal the deformation zone by etching.

In this work, we will apply the designed experimental protocol of wedge-like indentation and DIC technique to follow the evolution of the plastic deformation and flow field in ductile metals. Moreover, illuminate the details of plastic deformation mechanism by comparing with the numerical and analytical solutions.

Study of Inhomogeneous Deformation of BMG by DIC

Inhomogeneous deformation behavior of Vitreloy-1 bulk metallic glass has been experimentally studied by wedge-like cylindrical indentation and the process zone evolution has been analyzed by the DIC technique. According to the limitation of DIC technique, the strain levels of the shear bands in strain maps can be used for visualization purpose only. However, by measuring displacement jumps of two selected points on the shear bands,

Lagrangian strain components of the shear band also could be estimated over the entire shear band thickness at different stages of the whole loading cycle. The surrounding matrix strain levels are evaluated by bi-linear surface fitting local displacement distribution. The single shear band evolution has been studied in detail and at the mean time the experimental observation shows the nature of the shear band deformation. Finally, the detailed measurement of single shear band initiation is compared with a numerical model based on continuum mechanics.

Fracture Testing of Ni-based BMG

Recently, the Ni-based BMG and BMG composite containing brass fibers were fabricated by warm extrusion of gas atomized powders [80] and the plasticity of the BMG composites with different volume fractions and powder sizes were studied. The results showed that the BMG composite with 40% volume fraction of the brass phase showed highest ductility and the powder size of the brass is less than 63 μm. The mechanical properties of the BMG and BMG composite have been tested by uniaxial compression test along the extrusion direction and the stress-strain curve is shown in Fig.1.5, in which a monolithic Ni-base BMG by Cu-mold injection casting was compared [81]. As shown in the Fig.1.5, the injection casting BMG has the highest strength with 2% plastic strain to failure and the BMG by warm extrusion didn't show any plastic strain before failure. But the BMG composite has improved ductility compared to the warm extrusion BMG.

In this study, the evolution of the deformation and damage in the BMG/Brass composite system was studied with an experimental set up that enables in-situ observations

during the course of a wedge like cylindrical indentation. By quasi-static loading mode, the BMG/Brass composite was indented in two directions, parallel and normal to the extrusion direction, and more details will be presented in the following sections.

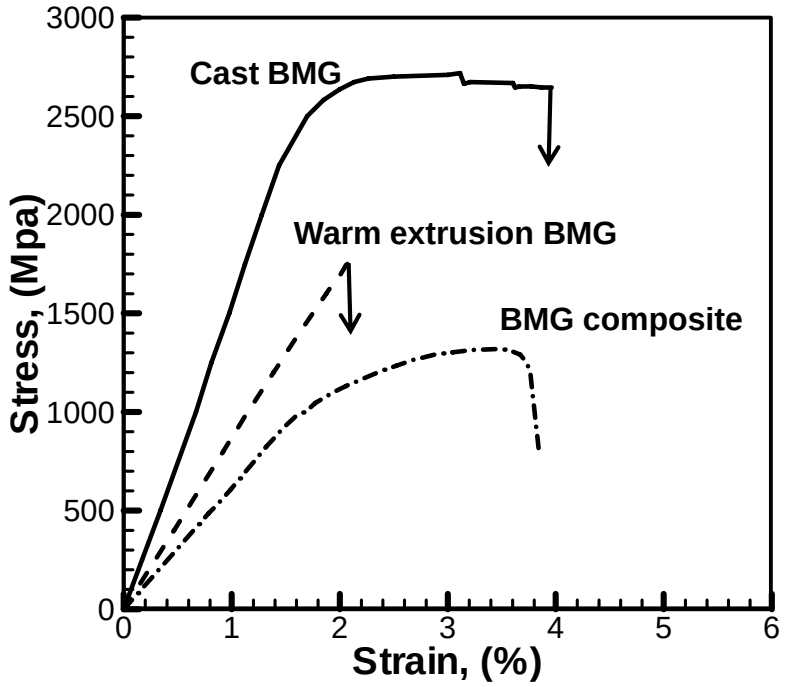

Figure 1.5 Stress-strain curves for the injection cut BMG, warm extrusion BMG and BMG composite reinforced by 40% brass under uniaxial compression test. [81]

1.4 STRUCTURE OF THE DISSERTATION

The goal of this dissertation is to understand BMG inhomogeneous deformation evolution through macroscopic and microscopic scale by experimental measurements and the numerical analysis. Therefore, as indicated in Section 1.3, digital image correlation (DIC) technique will be discussed in Chapter 2. The underlying principle of DIC technique will be

detailed explained and also calibration is conducted by analyzing highly localized deformation band. The displacement and strain level inside and outside of the localized deformation bands have been thoroughly examined. Based on the limitation of this technique, corrected evaluations of the band width and strain of the band have been indicated. To calibrate the validity of DIC technique in 2D indentation test, the deformation and flow characteristics of ductile metals have been studied in Chapter 3. The plastic deformation field of annealed polycrystalline copper and aluminum alloy are examined underneath cylindrical indenter. Also, FEM numerical model and Cavity Expansion model are discussed to evaluate the experimental measurements. Chapter 4 presents the inhomogeneous deformation of BMG under wedge-like cylindrical indentation test. The in-plane maximum shear strain is evaluated by DIC technique over the plastic deformation zone. The evolutions of the shear strain inside and outside of the single shear band have been compared. Also the experimental measurement of the shear band initiation has been confirmed by the numerical model prediction based on continuum mechanics. By the same experimental setup, Ni-based BMG composite has been studied in Chapter 5. The macroscopic deformation has shown the improved the ductility of the BMG composite and the fracture toughness has been evaluated after examining the fracture toughening mechanism. For the anisotropic BMG composite, the fracture initiation has been discussed by two mechanisms, stress control and strain control. Finally, the appendix presents spectral analysis of 3D fracture surfaces for enhanced matching, which is used to determine the likelihood that certain broken pieces would/not match the broken piece found at crime scene. The work in the appendix is an independent project on inhomogeneous deformation of bulk metallic glass that is main research goal during the Ph.D study.

1.5 REFERENCE

[1] W.Klement, R.H.Willens, and P.Duwez, "Non-crystalline structure in solidified gold-silicon alloys," *Nature*, vol. 187, Sep. 1960, pp. 869-870.

[2] P. Duwez, R.H.Willens and R.C. Crewdson, "Amorphous Phase in Palladium-Silicon Alloys," *Journal of Applied Physics*, vol. 36, 1965, p. 2267.

[3] A. Drehman, A. Greer, and D. Turnbull, "Bulk formation of a metallic glass-Pd40Ni40P20," *Applied Physics Letters*, vol. 41, 1982, pp. 7167-717.

[4] A. Inoue, T. Nakamura, N. Nishiyama, and T. Masumoto, "Mg-Cu-Y Bulk Amorphous Alloys with High Tensile Strength Produced by a High-Pressure Die Casting Method," *Mater. Trans. JIM*, vol. 33, 1992, p. 937.

[5] A. Peker and W.L. Johnson, "A highly processable metallic glass: Zr41.2Ti13.8Cu12.5Ni10.0Be22.5," *Applied Physics Letters*, vol. 63, 1993, p. 2342.

[6] A. Inoue, T. Zhang, N. Nishiyama, K. Ohba, and T. Masumoto, "Preparation of 16 mm Diameter Rod of Amorphous Zr65Al7.5Ni10Cu17.5 Alloy ," *Mater. Trans.,JIM*, vol. 34, 1993, p. 1234.

[7] A. Gebert, K. Buchholz, A. Leonhard, K. Mummert, J. Eckert, and L. Schultz, "Investigations on the electrochemical behaviour of Zr-based bulk metallic glasses," *Materials Science and Engineering A*, vol. 267, 1999, pp. 294-300.

[8] L. Davis, "HARDNESS/STRENGTH RATIO OF METALLIC GLASSES.," *Scripta Metallurgica*, vol. 9, 1975, pp. 431-435.

[9] P. Donovan, "Plastic flow and fracture of Pd40Ni40P20 metallic glass under an indentor," *Journal of Materials Science*, vol. 24, 1989, pp. 523-535.

[10] Y. Kawamura, T. Nakamura, and A. Inoue, "Superplasticity in Pd40Ni40P20 metallic glass," *Scripta Materialia*, vol. 39, 1998, pp. 301-306.

[11] H. Bruck, T. Christman, A. Rosakis, and W. Johnson, "Quasi-static constitutive behavior of Zr41.25Ti13.75Ni10 Cu12.5Be22.5 bulk amorphous alloys," *Scripta metallurgica et materialia*, vol. 30, 1994, pp. 429-434.

[12] W.J. Wright, R.B. Schwarz, and W.D. Nix, "Localized heating during serrated plastic flow in bulk metallic glasses," *Materials Science and Engineering A*, vol. 319-321, 2001, pp. 229-232.

[13] W.L. Johnson, "Bulk glass-forming metallic alloys: Science and technology," *MRS Bulletin(USA)*, vol. 24, 1999, pp. 42–56.

[14] R. Conner, A. Rosakis, W. Johnson, and D. Owen, "Fracture toughness determination for a beryllium-bearing bulk metallic glass," *Scripta Materialia*, vol. 37, 1997, pp. 1373-1378.

[15] P. Wesseling, T. Nieh, W. Wang, and J. Lewandowski, "Preliminary assessment of flow, notch toughness, and high temperature behavior of Cu60Zr20Hf10Ti10 bulk metallic glass," *Scripta Materialia*, vol. 51, 2004, pp. 151-154.

[16] X. Xi, D. Zhao, M. Pan, W. Wang, Y. Wu, and J. Lewandowski, "Fracture of brittle metallic glasses: Brittleness or plasticity," *Physical Review Letters*, vol. 94, 2005, pp. 1-4.

[17] H. Kimura and T. Masumoto, "DEFORMATION AND FRACTURE OF AN AMORPHOUS Pd-Cu-Si ALLOY IN V-NOTCH BENDING TESTS - 2. DUCTILE-BRITTLE TRANSITION.," *Acta Metallurgica*, vol. 28, 1980, pp. 1677-1693.

[18] C. Shek, G. Lin, K. Lee, and J. Lai, "Fractal fracture of amorphous Fe46Ni32V2Si14B6 alloy," *Journal of Non-Crystalline Solids*, vol. 224, 1998, pp. 244-248.

[19] C.A. Pampillo, "FLOW AND FRACTURE IN AMORPHOUS ALLOYS.," *Journal of Materials Science*, vol. 10, 1975, pp. 1194-1227.

[20] A. Sergueeva, N. Mara, J. Kuntz, E. Lavernia, and A. Mukherjee, "Shear band formation and ductility in bulk metallic glass," *Philosophical Magazine*, vol. 85, 2005, pp. 2671-2687.

[21] F. Spaepen, "MICROSCOPIC MECHANISM FOR STEADY STATE INHOMOGENEOUS FLOW IN METALLIC GLASSES.," *Acta Metallurgica*, vol. 25, 1977, pp. 407-415.

[22] H. Chen and M. Goldstein, "ANOMALOUS VISCOELASTIC BEHAVIOR OF METALLIC GLASSES OF Pd-Si-BASED ALLOYS.," *Journal of Applied Physics*, vol. 43, 1972, pp. 1642-1648.

[23] A. Vinogradov and V. Khonik, "Kinetics of shear banding in a bulk metallic glass monitored by acoustic emission measurements," *Philosophical Magazine*, vol. 84, 2004, pp. 2147-2166.

[24] M. Patnaik, R. Narasimhan, and U. Ramamurty, "Spherical indentation response of metallic glasses," *Acta Materialia*, vol. 52, 2004, pp. 3335-3345.

[25] U. Ramamurty, S. Jana, Y. Kawamura, and K. Chattopadhyay, "Hardness and plastic deformation in a bulk metallic glass," *Acta Materialia*, vol. 53, 2005, pp. 705-717.

[26] A.C. Lund and C.A. Schuh, "Yield surface of a simulated metallic glass," *Acta Materialia*, vol. 51, 2003, pp. 5399-5411.

[27] A. Antoniou, A. Bastawros, and B. Biner, "Experimental observations of deformation behavior of bulk metallic glasses during wedge-like cylindrical indentation," *Journal of Materials Research*, vol. 22, 2007, pp. 514-524.

[28] R. Conner, W. Johnson, N. Paton, and W. Nix, "Shear bands and cracking of metallic glass plates in bending," *Journal of Applied Physics*, vol. 94, 2003, pp. 904-911.

[29] C. Gilbert, R. Ritchie, and W. Johnson, "Fracture toughness and fatigue-crack propagation in a Zr-Ti-Ni-Cu-Be bulk metallic glass," *Applied Physics Letters*, vol. 71, 1997, p. 476.

[30] A. Antoniou, A. Bastawros, C. Lo, and S. Biner, "Deformation behavior of a zirconium based metallic glass during cylindrical indentation: In situ observations," *Materials Science and Engineering A*, vol. 394, 2005, pp. 96-102.

[31] P. Donovan, "Yield criterion for Pd40Ni40P20 metallic glass," *Acta Metallurgica*, vol. 37, 1989, pp. 445-456.

[32] R. Vaidyanathan, M. Dao, G. Ravichandran, and S. Suresh, "Study of mechanical deformation in bulk metallic glass through instrumented indentation," *Acta Materialia*, vol. 49, 2001, pp. 3781-3789.

[33] C. Hays, C. Kim, and W. Johnson, "Microstructure controlled shear band pattern formation and enhanced plasticity of bulk metallic glasses containing in situ formed ductile phase dendrite dispersions," *Physical Review Letters*, vol. 84, 2000, pp. 2901-2904.

[34] U. Kuhn, J. Eckert, N. Mattern, and L. Schultz, "ZrNbCuNiAl bulk metallic glass matrix composites containing dendritic bcc phase precipitates," *Applied Physics Letters*, vol. 80, 2002, p. 2478.

[35] H. Ma, J. Xu, and E. Ma, "Mg-based bulk metallic glass composites with plasticity and high strength," *Applied Physics Letters*, vol. 83, 2003, pp. 2793-2795.

[36] H. Choi-Yim, R. Busch, U. Koster, and W. Johnson, "Synthesis and characterization of particulate reinforced Zr57Nb5Al10Cu15.4Ni12.6 bulk metallic glass composites," *Acta Materialia*, vol. 47, 1999, pp. 2455-2462.

[37] R. Conner, R. Dandliker, and W. Johnson, "Mechanical properties of tungsten and steel fiber reinforced Zr41.25Ti13.75Cu12.5Ni10Be22.5 metallic glass matrix composites," *Acta Materialia*, vol. 46, 1998, pp. 6089-6102.

[38] F. Szuecs, C. Kim, and W. Johnson, "Mechanical properties of Zr56.2Ti13.8Nb5.0Cu6.9 Ni5.6Be12.5 ductile phase reinforced bulk metallic glass composite," *Acta Materialia*, vol. 49, 2001, pp. 1507-1513.

[39] J. Eckert, M. Seidel, N. Schlorke, A. Kubler, and L. Schultz, "Solid state processing of bulk metallic glass forming alloys," *Materials Science Forum*, vol. 235-238, 1997, pp. 23-28.

[40] L. Xing, J. Eckert, W. Loser, and L. Schultz, "High-strength materials produced by precipitation of icosahedral quasicrystals in bulk Zr-Ti-Cu-Ni-Al amorphous alloys," *Applied Physics Letters*, vol. 74, 1999, pp. 664-666.

[41] L. Xing, J. Eckert, W. Loser, L. Schultz, and D. Herlach, "Crystallization behaviour and nanocrystalline microstructure evolution of a Zr57Cu20Al10Ni8Ti5 bulk amorphous alloy," *Philosophical Magazine A: Physics of Condensed Matter, Structure, Defects and Mechanical Properties*, vol. 79, 1999, pp. 1095-1108.

[42] J. Saida, M. Matsushita, T. Zhang, A. Inoue, M. Chen, and T. Sakurai, "Precipitation of icosahedral phase from a supercooled liquid region in Zr65Cu7.5Al7.5Ni10Ag 10 metallic glass," *Applied Physics Letters*, vol. 75, 1999, pp. 3497-3499.

[43] N. Boucharat, R. Hebert, H. Rosner, R. Valiev, and G. Wilde, "Nanocrystallization of amorphous Al88Y7Fe5 alloy induced by plastic deformation," *Scripta Materialia*, vol. 53, 2005, pp. 823-828.

[44] G. Wilde, N. Boucharat, G. Dinda, H. Rosner, and R. Valiev, "New routes for synthesizing massive nanocrystalline materials," *3rd International Conference on Nanomaterials by Severe Plastics Deformation, NanoSPD3, September 22, 2005 - September 26, 2005*, Fukuoka, Japan: Trans Tech Publications Ltd, 2006, pp. 425-432.

[45] H. Choi-Yim, R. Conner, F. Szuecs, and W. Johnson, "Processing, microstructure and properties of ductile metal particulate reinforced Zr57Nb5Al10Cu15.4Ni12.6 bulk metallic glass composites," *Acta Materialia*, vol. 50, 2002, pp. 2737-2745.

[46] R. Conner, H. Choi-Yim, and W. Johnson, "Mechanical properties of Zr57Nb5Al10Cu15.4Ni12.6 metallic glass matrix particulate composites," *Journal of Materials Research*, vol. 14, 1999, pp. 3292-3297.

[47] R. Dandliker, R. Conner, and W. Johnson, "Melt infiltration casting of bulk metallic-glass matrix composites," *Journal of Materials Research*, vol. 13, 1998, pp. 2896-2901.

[48] C. Kim, R. Busch, A. Masuhr, H. Choi-Yim, and W. Johnson, "Processing of carbon-fiber-reinforced Zr41.2Ti13.8Cu12.5Ni10.0B e 22.5 bulk metallic glass composites," *Applied Physics Letters*, vol. 79, 2001, p. 1456.

[49] H. Choi-Yim and W. Johnson, "Bulk metallic glass matrix composites," *Applied Physics Letters*, vol. 71, 1997, p. 3808.

[50] Z. Bian, R.J. Wang, W.H. Wang, T. Zhang, and A. Inoue, "Carbon-nanotube-reinforced Zr-based bulk metallic glass composites and their properties," *Advanced Functional Materials*, vol. 14, 2004, pp. 55-63.

[51] K.M. Flores and R.H. Dauskardt, "Fracture and deformation of bulk metallic glasses and their composites," *Intermetallics*, 2004, pp. 1025-1029.

[52] K.M. Flores, W.L. Johnson, and R.H. Dauskardt, "Fracture and fatigue behavior of a Zr-Ti-Nb ductile phase reinforced bulk metallic glass matrix composite," *Scripta Materialia*, vol. 49, 2003, pp. 1181-1187.

[53] J. Eckert, J. Das, S. Pauly, and C. Duhamel, "Mechanical properties of bulk metallic glasses and composites," *Journal of Materials Research*, vol. 22, 2007, pp. 285-301.

[54] A. Argon, "PLASTIC DEFORMATION IN METALLIC GLASSES.," *Acta Metallurgica*, vol. 27, 1979, pp. 47-58.

[55] Y. Shi and M.L. Falk, "Atomic-scale simulations of strain localization in a single-component three-dimensional model amorphous solid," *2005 MRS Fall Meeting, November 28, 2005 - December 2, 2005*, Boston, MA, United states: Materials Research Society, 2005, pp. 120-125.

[56] P. Steif, F. Spaepen, and J. Hutchinson, "STRAIN LOCALIZATION IN AMORPHOUS METALS.," *Acta Metallurgica*, vol. 30, 1982, pp. 447-455.

[57] R. Huang, Z. Suo, J. Prevost, and W. Nix, "Inhomogeneous deformation in metallic glasses," *Journal of the Mechanics and Physics of Solids*, vol. 50, 2002, pp. 1011-1027.

[58] J. Li, F. Spaepen, and T. Hufnagel, "Nanometre-scale defects in shear bands in a metallic glass," *Philosophical Magazine A: Physics of Condensed Matter, Structure, Defects and Mechanical Properties*, vol. 82, 2002, pp. 2623-2630.

[59] W. Peters and W. Ranson, "DIGITAL IMAGING TECHNIQUES IN EXPERIMENTAL STRESS ANALYSIS.," *Optical Engineering*, vol. 21, 1982, pp. 427-431.

[60] T. Chu, W. Ranson, M. Sutton, and W. Peters, "APPLICATIONS OF DIGITAL-IMAGE-CORRELATION TECHNIQUES TO EXPERIMENTAL MECHANICS.," *Experimental Mechanics*, vol. 25, 1985, pp. 232-244.

[61] G. Vendroux and W. Knauss, "Deformation Measurements at the sub-micron size scale: II.Refinements in the Algorithm for digital image correlation," Graduate Aeronautical Laboratories, California Institute of Technology,1994.

[62] M. Sutton and Y. Chao, "novel experimental techniques in the fracture mechanics ," *ASME*, vol. 176, 1993, pp. 203-217.

[63] G. Han, M. Sutton, and Y. Chao, "Study of stationary crack-tip deformation fields in thin sheets by computer vision," *Experimental Mechanics*, vol. 34, 1994, pp. 125-140.

[64] Z. He, M. Sutton, W. Ranson, and W. Peters, "TWO-DIMENSIONAL FLUID-VELOCITY MEASUREMENTS BY USE OF DIGITAL-SPECKLE CORRELATION TECHNIQUES.," *Experimental Mechanics*, vol. 24, 1984, pp. 117-121.

[65] J. Cardenas-Garcia, H. Yao, S. Zheng, and R. Zartman, "digital image correlation procedure to characterize soil surface layer cracking," *Agronomy Journal*, vol. 90, 1998, pp. 438-441.

[66] W. Tong, "Detection of plastic deformation patterns in a binary aluminum alloy," *Experimental Mechanics*, vol. 37, 1997, pp. 452-459.

[67] H. Lu, "Applications of digital speckle correlation to microscopic strain measurement and materials' property characterization," *Journal of Electronic Packaging, Transactions of the ASME*, vol. 120, 1998, pp. 275-279.

[68] A. Bastawros, H. Bart-Smith, and A. Evans, "Experimental analysis of deformation mechanisms in a closed-cell aluminum alloy foam," *Journal of the Mechanics and Physics of Solids*, vol. 48, 2000, pp. 301-322.

[69] H. Bruck, S. McNeill, M. Sutton, and W. Peters III, "Digital image correlation using Newton-Raphson method of partial differential correction," *Experimental Mechanics*, vol. 29, 1989, pp. 261-267.

[70] Y. Wang and A.M. Cuitino, "Full-field measurements of heterogeneous deformation patterns on polymeric foams using digital image correlation," *International Journal of Solids and Structures*, vol. 39, 2002, pp. 3777-3796.

[71] D. Tabor, "Hardness and strength of metals," *Institute of Metals*, vol. 79, 1951, pp. 1-18.

[72] K.L. Johnson, "Correlation of indentation experiments," *J MECHANICS PHYSICS SOLIDS*, vol. 18, 1970, pp. 115–126.

[73] I. Sneddon, "Relation between load and penetration in axisymmetric Boussinesq problem for punch of arbitrary profile," *International Journal of Engineering Science*, vol. 3, 1965, pp. 47-57.

[74] W. Oliver and G. Pharr, "Improved technique for determining hardness and elastic modulus using load and displacement sensing indentation experiments," *Journal of Materials Research*, vol. 7, 1992, pp. 1564-1580.

[75] D. Kramer, H. Huang, M. Kriese, J. Robach, J. Nelson, A. Wright, D. Bahr, and W. Gerberich, "Yield strength predictions from the plastic zone around nanocontacts," *Acta Materialia*, vol. 47, 1998, pp. 333-343.

[76] A. Bhattacharya and W. Nix, "Finite element analysis of cone indentation," *International Journal of Solids and Structures*, vol. 27, 1991, pp. 1047-1058.

[77] Y. Wei and J.W. Hutchinson, "Hardness trends in micron scale indentation," *Journal of the Mechanics and Physics of Solids,v51,n11-12 ,*2003, pp. 2037-2056.

[78] T. Mulhearn, "The deformation of metals by vickers-type pyramidal indenters," *Journal of the Mechanics and Physics of Solids*, vol. 7, Mar. 1959, pp. 85-88.

[79] L. Samuels and T. Mulhearn, "An experimental investigation of the deformed zone associated with indentation hardness impressions," *Journal of the Mechanics and Physics of Solids*, vol. 5, Mar. 1957, pp. 125-134.

[80] M. Lee, D. Bae, D. Kim, and D. Sordelet, "Synthesis of Ni-based bulk metallic glass matrix composites containing ductile brass phase by warm extrusion of gas atomized powders," *Journal of Materials Research*, vol. 18, 2003, pp. 2101-2108.

[81] M. Lee, J. Lee, D. Bae, W. Kim, D. Sordelet, and D. Kim, "A development of Ni-based alloys with enhanced plasticity," Intermetallics, 2004, pp. 1133-1137.

CHAPTER 2: MEASUREMENTS OF LOCALIZED DEFORMATION BY DIGITAL IMAGE CORRELATION: UNIAXIAL STRAIN

2.1 ABSTRACT

Highly localized deformation filed under uniaxial loading condition has been studied by digital image correlation (DIC) technique. Different length parameters used in DIC have been investigated to decide their contribution to the apparent width of the localization band estimated by DIC. The width of the localization band and the strain inside of the localization has been examined by the resultant displacement and strain field, respectively. An empirical equation about the estimation of the localization width is summarized by manually study of different situations and it has been successfully applied in the localization investigation of uniaxial deformed aluminum foam.

2.2 INTRODUCTION

Digital Image Correlation (DIC) technique has been developed for many years and it was first proposed in early 1980s to compute the surface strains and displacements [1]. It has been used either as a quantitative tool for average and homogeneous strains of macroscopically uniform deformation[2], or as a whole-field deformation mapping tool to measure highly localized deformation fields such as the ones surrounding a crack tip [3] and characterization of strain bifurcation in foams[4], doctor in details ahead of a particular shear band, detection of microscopic large strain by SEM topography image [6], plastic deformation patterns PLC bands[7] , compression strain measurement of aluminum alloy foams [8].

As a deformation measurement technique, DIC provides estimation of the displacement field by correlating the features in a pair of digital images of a specimen surface before and after deformation by a mathematically well-defined function. DIC technique has different correlation algorithms, such as estimating discrete displacements data by local optimal match of intensity pattern in subsets (Subset method) [9] and obtaining continuous displacement field function by full-field optimal match of the intensity pattern (Continuous method) [10]; different gray value interpolation schemes, such as most commonly used polynomial or B-spline for 2D surface [11] and tricubic interpolator based on 1D Hermitian cardinal basis functions for 3D volume [12]. The continuous method normally predicts more accurate displacements and displacement gradients than subsets method in the deformation field without localization [10], while the disadvantage in the localized deformation filed is that the localization would be smoothed out, especially in the discontinuous deformation field. Recently, for single shear band-like localization, an extended DIC approach has been introduced to partition the field into different parts and estimate the discontinuity [5]. However, in the highly localized heterogeneous deformation field, there would be multiple localizations involved with each other, such as bulk metallic glass under indentation [13], and the localization domain could be wider than a single line. Therefore, understanding the resolution and limitation for the highly localized deformation by DIC technique is critical to adjudge the width and strain level inside of the localization sites.

In this paper, a DIC code has been developed based on subset method [14] [15] and the localized deformation filed has been explored by this technique. In the post DIC

processing, the resolution of displacement and strain has been studied and the dependence of several length parameters has been investigated. At the end of the work, the strain analysis of localization in the compression of aluminum alloy foam is cited as an example.

2.3 IMPLEMENTATION PLAN

Localization creation

One image with the dimension of 200pixel×1200pixel having a well-patterned surface is chosen to generate the artificial localization bands. As shown in Fig.2.1 (a), the positions of the generated localization bands are schematically shown by the black dash lines in the strip of the image. The width of the localization bands, L_0 is from 2pixels to 100 pixels with respect to the strain component ε_{xx} range from 50% to 1% and the image is stretched uniformly inside of the localization bands. The spacing between any two localization bands is large enough, so that there is no neighbor band influence in the DIC analysis of the localizations.

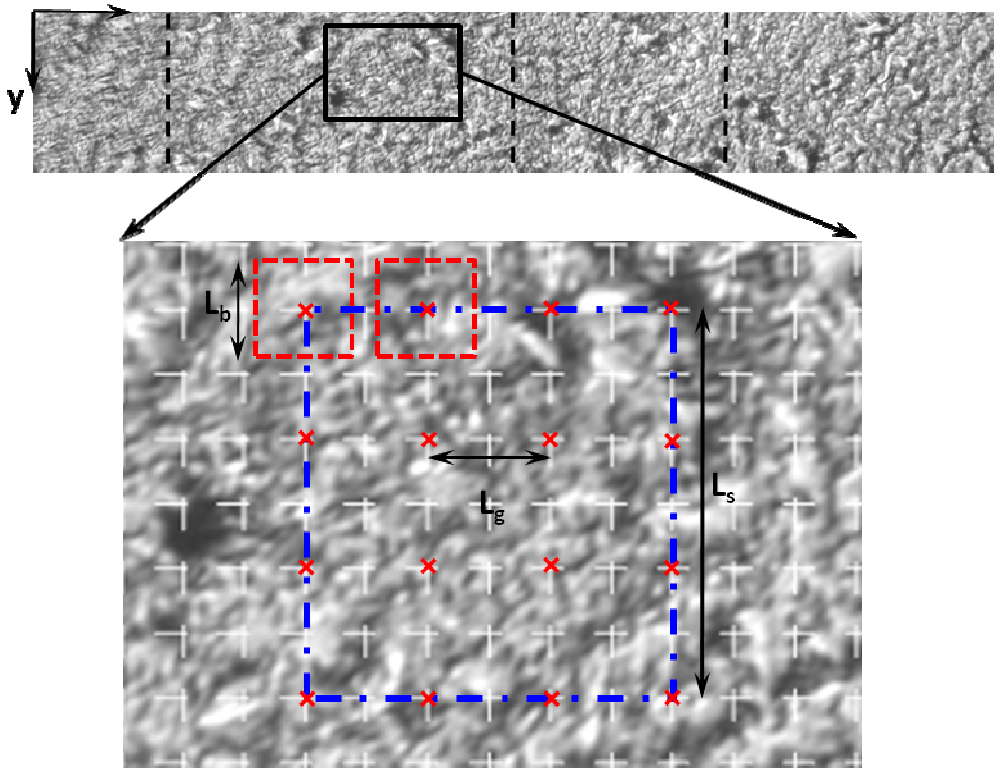

Figure 2.1 (a) A well-patterned image utilized to create artificial localization bands with different width; (b) A schematic figure that shows the parameters involved in the DIC technique.

Digital Image Correlation Local Search Scheme

The pair of images is analyzed by DIC technique code developed in house, involving two main steps: coarse and fine search. The coarse search step is based on maximizing the intensity correlation coefficient between the sub-windows to an integer number pixel, and only displacement components are changed. Central part of the sub-window called correlation window is used in the fine search routine, and the expanded 2-D eignvalues of local match including the displacement gradients, coupled with iterative Newton-Raphson method, are achieved sub pixel's resolution. The gray value distribution in the correlation

window is given at every pixel; however, to obtain sub-pixel accuracy, the estimation of the value and its derivatives between pixels requires an interpolation scheme. Different interpolation schemes have been tried such as bi-linear, bi-cubic, high order polynomials and B-spline method. Based on the accuracy and systematic errors analysis [11] (Schreier *et al*, 2000), B-spline interpolation method is utilized in this study. Since the interpolation is only computed once in the deformed configuration, sub-window is centered in a 20% larger interpolation window leaving a buffer of several pixels at the edge to allow the sub-window movement during the local matching. The acquired nodal displacements from both coarse and fine search represent the average displacement of each sub-window.

After fine search, some post DIC processing steps are required to convert the displacement maps into strain maps. The spatial displacement gradients are evaluated relative to the undeformed configuration by spatial derivative a polynomial fit of the nodal displacement vectors. The gradient tensor **F** is obtained by:

$$\mathbf{F} = \mathbf{I} + \nabla \mathbf{u} \tag{1}$$

where ∇ indicates the spatial gradient. The components of the Lagrangian strain tensor $\mathbf{E}^*$ are evaluated over the undeformed configuration from:

$$\mathbf{E}^* = \frac{\mathbf{1}}{\mathbf{2}}(\mathbf{F}^T\mathbf{F} - \mathbf{I}) \tag{2}$$

The deformation is characterized by the effective strain map, which is defined as the in-plane maximum shear strains, $\boldsymbol{\varepsilon}_{\mathbf{eff}}$:

$$\varepsilon_{eff} = \left|\varepsilon_{22} - \varepsilon_{11}\right| = \sqrt{\left(\varepsilon_{xx} - \varepsilon_{yy}\right)^2 + 4\varepsilon_{xy}^2} \tag{3}$$

2.4 LOCALIZATION ANALYSIS

Band Width Estimation Based on Displacement

In the process of subset method, the pair of images is decomposed into a sequence of sub-windows and the dimension is determined by several factors, like intensity distribution, intensity pattern dimension, and average grain size, etc. The size of square correlation window L_b, spacing between two continuous sub-windows L_g and the strain gauge length L_s are shown in Fig.2.1 (b). In the course of the fine search, the average displacements of the sub-windows are determined by the local optimal intensity match inside of the correlation window, which represents the center nodal deformation of the sub-window. Therefore, if the correlation window contains one or partial of the localization band, the displacement determination in fine search step could be biased. In other words, the displacement starts to show the localization before the center of the sub-window moves to the center of the localization. In that case, the size of the correlation window L_b should be counted into the localization band width calculation. Another important parameter in the subset method is the spacing between the centers of two sub-windows, L_g, which determines how many sub-windows within the resultant localization bands.

Based on previous discussion, it shows that the length parameters in the DIC process are critical for determination of the resultant displacement and strain level inside of the localization band. To explore the dependence of these parameters, different cases have been

studied as shown in Fig.2.2. Firstly, for the DIC displacement results, spacing between two sub-window L_g and size of correlation window L_b are constant with the value of 5 pixels and 16 pixels, respectively. Fig.2.2 (a) has shown the DIC displacement results of artificial localization bands with different width of 3, 7, 20 and 40 pixels, and the results shows that if L_g and L_b are constant, the wider artificial localization the better estimation of the apparent band width L_{app} from DIC method. For constant artificial band width L_0 of 20 pixels and constant L_g of 5 pixels, Fig.2.2 (b) shows the DIC displacements results with different dimension of correlation windows L_b ranging from 10 pixels to 18 pixels. The apparent band width L_{app} increases with the size of the correlation window L_b, which results from the fact that the local match could be affected in the fine search because of the larger size of L_b when the center of the sub-window is far from the center of the localization. In Fig.2.2 (c), the artificial band width L_0 is 20 pixels and L_b is 16 pixels, while the spacing between tow sub-windows is changing from 3 pixels to 10 pixels. The apparent localization band width in the displacement results shows the trend that it increases with the spacing L_g. According to the above DIC displacement results, to estimate the localization bands is complicated since there are three length parameters involved with different contributions.

Summarizing the observation of all results in Fig.2.2, one important phenomenon in the apparent band of the DIC displacement is that the band estimation is always integer number times of the L_g value and the DIC method overestimates the band width. Therefore, in order to organize the dependent relation, all of the length parameters are normalized by the spacing between two sub-windows L_g. There are four L_g length scales have been investigated in this study, those are 3, 5, 7 and 10 pixels. In each case, a range of artificial band width L_0

of 2, 3, 5, 7, 10, 20, and 40 pixels have been analyzed by DIC technique with different correlation window sizes of 10, 14, 16 and 18 pixels. The size of the correlation window is dependent on the pattern size and gray intensity distribution. The variations of the normalized apparent localization bands and normalized artificial band width for all of four cases are plotted in Fig.2.3, which are estimated based on DIC displacements results. According to the relations, one equation could summarize the relation between normalized apparent band width and normalized artificial band width, which is

$$L_{app} / L_g = roundup\left[(L_0 + L_b) / L_g \right] \tag{4.a}$$

or,

$$L_0 / L_g = \left[\left(L_{app} - L_b \right), \left(L_{app} - L_b - L_g \right) \right] / L_g \tag{4.b}$$

The Eq.1.a has been plotted by dash lines in the Fig.2. 3 and it shows that most of the situations follow the relation except some special cases, such as the apparent band width is smaller than the equation prediction one L_g spacing. Since the equation utilizes the function of roundup that would overestimate the band width, there are two limited values for the estimation of exact band width and the resolution is based on the L_g spacing. And most of the exact solutions of the band width are fallen into the region defined by upper and lower bound through Eq.4.b.

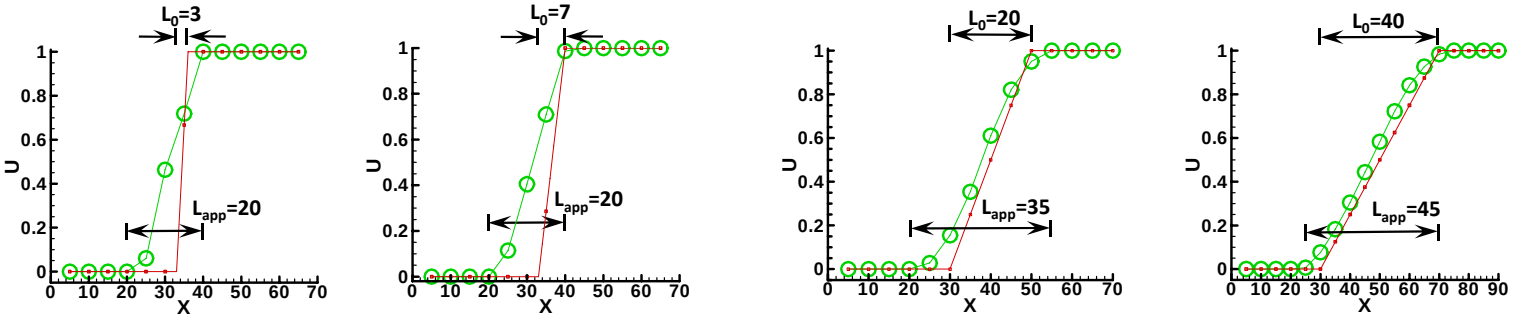

(a) L_g=5 pixels, L_b=16 pixels

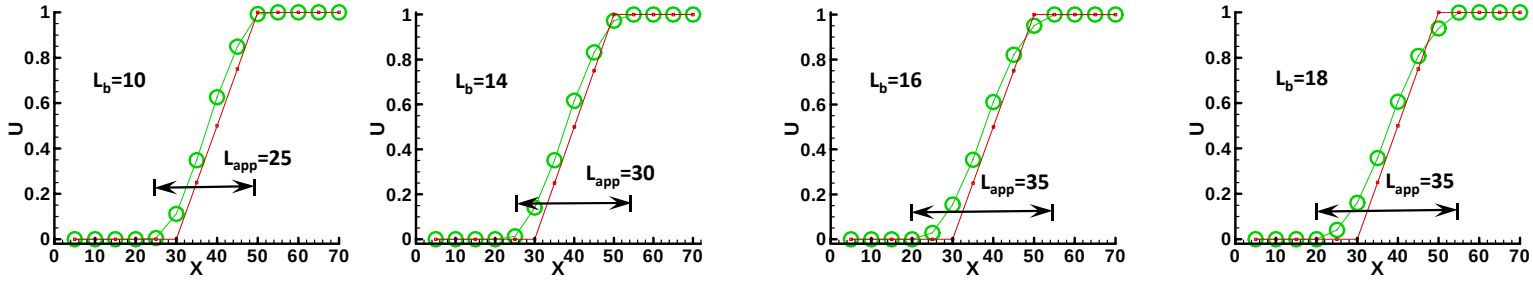

(b) L_g=5 pixels, L_0=20 pixels

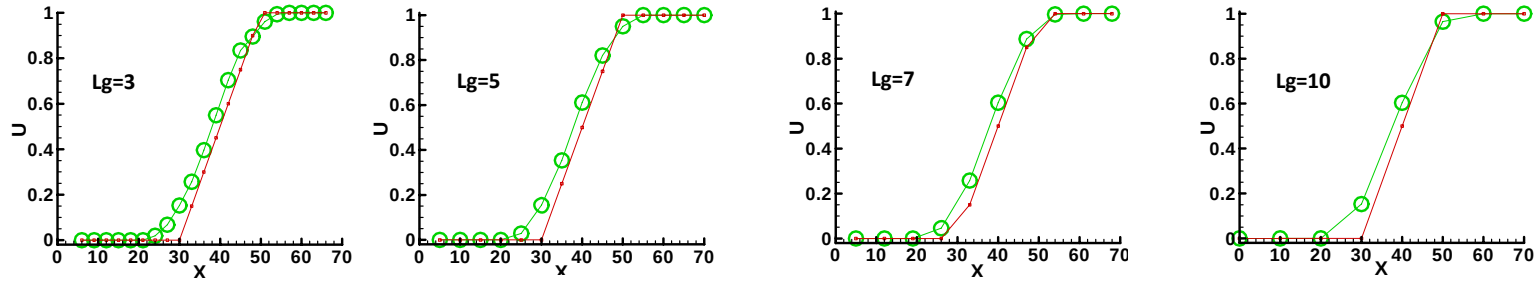

(c) L_b=16 pixels, L_0=20 pixels

Figure 2.2 The measurements of the localization band width by DIC technique with circle symbols and the exact solution of the band width by solid dot line.

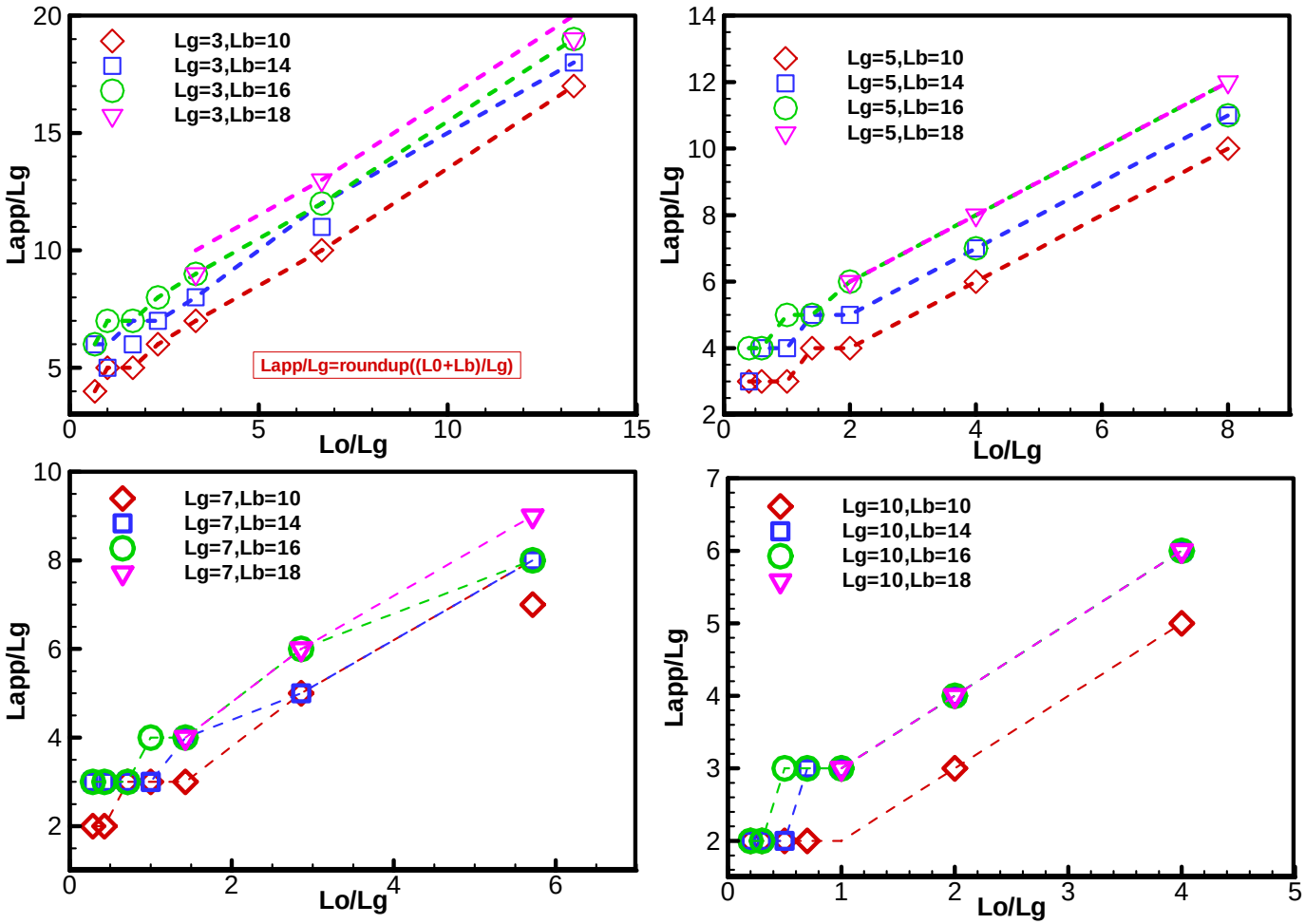

Figure 2.3 The variations of the normalized apparent localization bands and normalized artificial band width for different L_g values. The empirical equation is shown in (a), and the dash lines are followed this equation.

To explore the improvement of the evaluation of the band width by correlation equation, the average strain inside of the localization bands has been defined by:

$$\varepsilon_{avg} = \frac{\Delta u}{L_0} \tag{5}$$

where, Δu is the displacement difference across the localization band and L_0 is the band width which could be the exact width, the apparent width, or the one after correction by Eq.1. The average strain levels of the artificial localization bands are plotted with dash line in Fig.2.4 for all of the parameter combination situations discussed previously. The unfilled symbols represent the average strain levels before correction, which is obtained directly from the apparent band width of DIC displacement results; While, the filled symbols stand for the average strain level after correction that are calculated with the upper bound of Eq.1.b. According to the plots, there are more improvements in the average strain after correction if the grid spacing L_g is small and it also shows that the spacing L_g determines the resolution of the displacement and the average strain level inside of the localization band. However, such improvements are not very obvious by increasing the localization band width L_0, since the DIC displacement results could have better estimation of the wider localization bands by the observation in Fig.2.2.

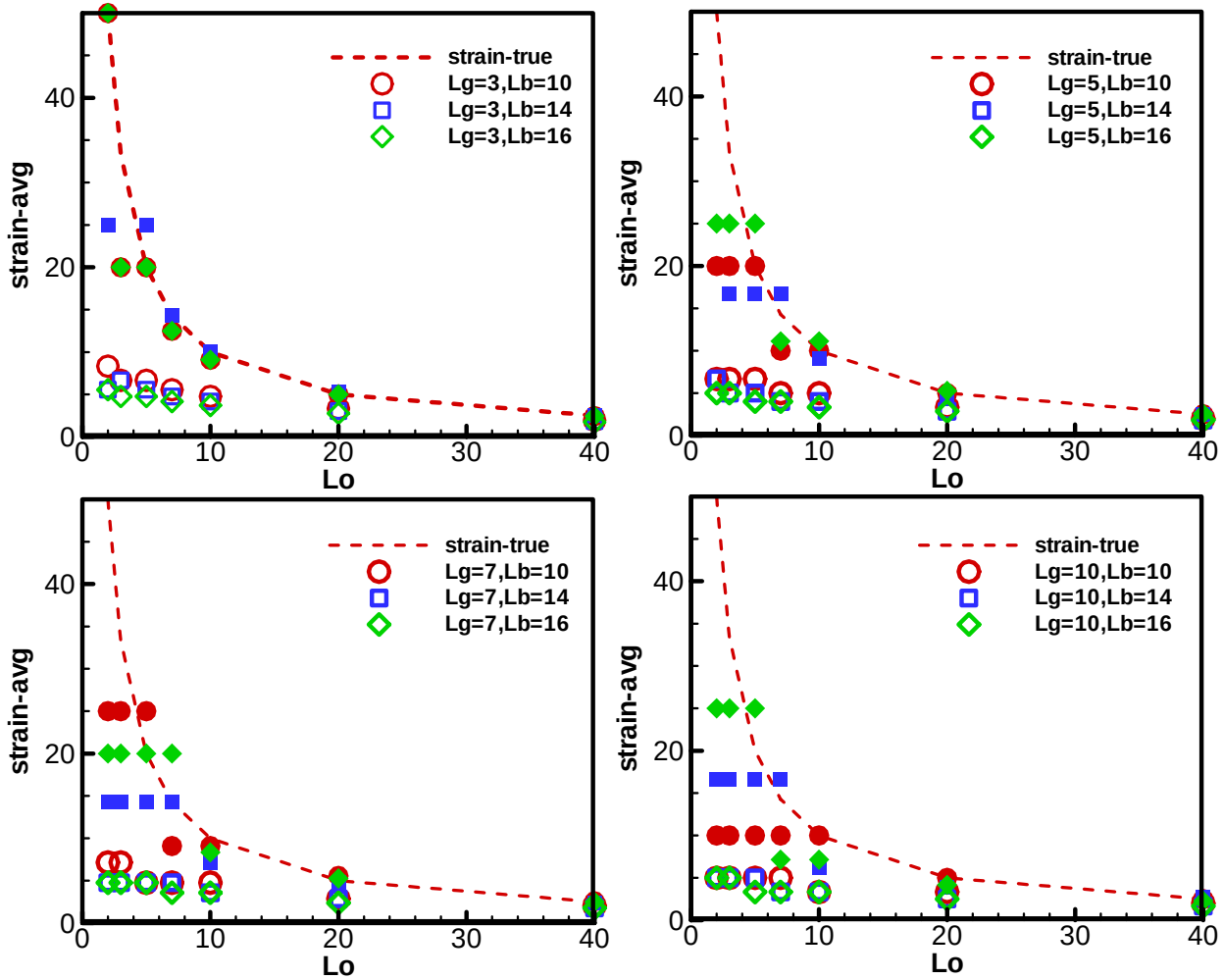

Figure 2.4 The average strain values based on the apparent band width (unfilled symbols) are compared with the ones estimated from the empirical equation (filled symbols) and the later ones are more closed to the actual strain level.

Band Width Estimation Based on Strain

In the post DIC process, the strain gauge length L_s as one more factor will be added into the resultant localization band width in the strain map and different local displacement fit within strain gauge length will result into different magnitude of the strain inside of the localization. In the evaluation the displacement gradients, there always is a tradeoff between closeness of fit and smoothness of fit, which has obvious effect in the case of highly localized deformation filed. For the sake of proper filtering the noise in the discrete displacement data, several smoothing methods have been discussed [7]; while such routines could dilute the localization when the width of the localization bands is thinner than the sub-window size, in which the relation among strain gauge length L_s, dimension of correlation window L_b, grid spacing and localization width L_g plays an important role to achieve reliable displacement gradients.

To adjudge the strain gauge length L_s, Fig.2.5 shows effective strain plots by biquadratic polynomial fit with different L_s value but constant L_0, L_b and L_g. The results indicate that the apparent band width in strain plot increases with the strain gauge length L_s and apparent maximums strain level decreases with the gauge length. From the DIC strain maps, the apparent band width also has been studied. Since the post DIC process is based on the results of the fine search, the bias of the band width from the DIC displacement results are added into the one from DIC strain maps. Therefore, in this step, we need to investigate the contribution of the strain gauge length by understanding the apparent band width of DIC displacement result. There are two cases: (1) Ls/L_g =4, and L_g spacing is 3 pixels with correlation window size from 10 pixels to 18 pixels; (2) Ls/L_g =2and L_g is 7 pixels with the

same rang of correlation window size. The normalized apparent band width relation between the one estimated from the DIC displacement and the one from strain indicates that there is a constant difference between these two method estimations that is equal to the value of Ls/L_g. The apparent band width from the strain result could be expressed by,

$$L_{app} / L_g = roundup\left[(L_0 + L_b) / L_g \right] + L_s / L_g \tag{6}$$

To summarize the above observation of the DIC technique application in the case of localization, the apparent band width from both displacement and strain results overestimates the exact value. It is a result from different parameters with different contribution involved in this technique. As what have been studied, the different parameters' contribution in the band width evaluation is closely related to the band width, and the DIC technique could provide a better solution, if the localization band is wide enough. The range of exact band width could be predicted from the apparent band width of DIC method by an empirical equation. However, it is impossible to convert the apparent band width by DIC method into exact solution for the whole deformation field automatically, because of the complexity of the localization in the deformation zone. In the post DIC process, the strain map is obtained by proper fitting the discrete displacement data over a certain gauge length L_s. The apparent band width of strain map is based on the one of DIC displacement evaluation and the critical parameter to determine the resolution is the grid spacing L_g, especially for the thin localization band situation. Therefore, to study the localization band width and the average strain level within a band, the displacement result of DIC technique is very important in the evaluation.

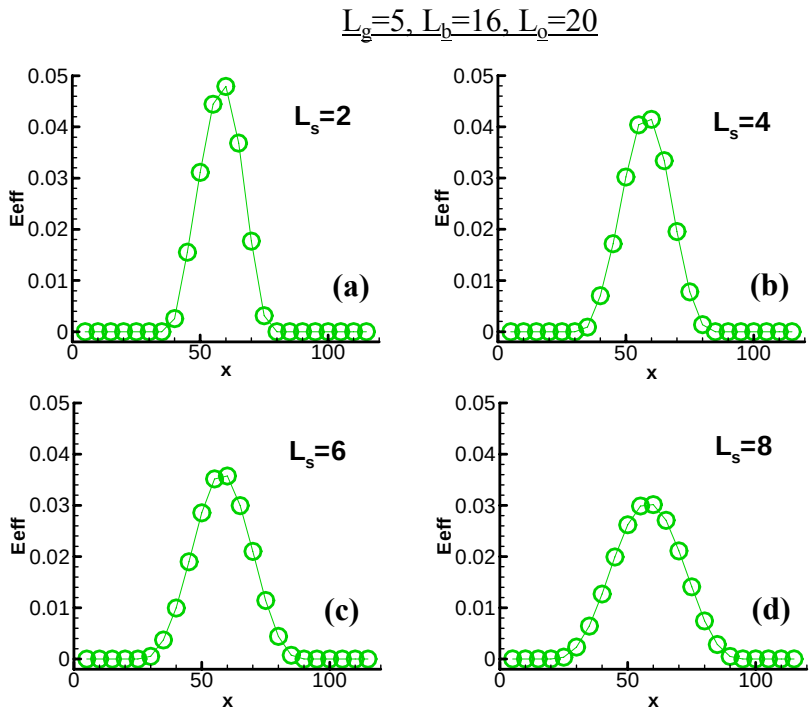

Figure 2.5 The variation of effective strain with increasing strain gauge length L_s.

2.5 CASE STUDY

Uniform Compression of Closed Cell Foam

The specimen used in this study is closed cell aluminum foam (ALPORAS) (Akiyama S. US patent no.4713277), with a 7.5% relative density. The cells are relative equiaxed polyhedral cells (Fig.2.6) and microscopic response is approximately isotropic. The compressive Young's modulus upon unloading is: $E = 0.7 \sim 1.0 GPa$ and the nominal plateau stress, designated as the first peak in the stress/strain curve (Fig.2.7) is around 1.2 *MPa*. Compression specimens have been cut from a cast block, by using electro-discharge machining to minimize membrane damage. The cross section of the sample is 52mm×27mm and the length of the sample is around 99mm. The foam sample was loaded in a

servohydraulic testing machine (Instron 8501) under displacement control at 50μm/s. The macroscopic stress and strain relation is based on the engineering stress and logarithmic strain definitions shown in Fig.2.7.

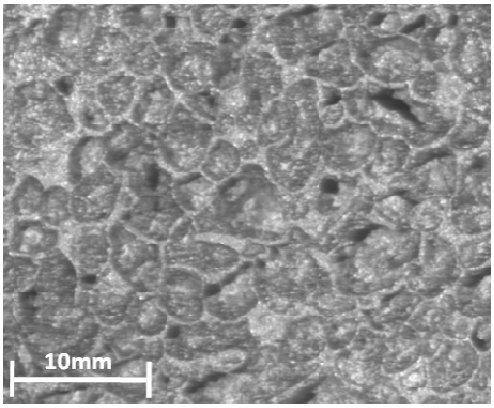

Figure 2.6 Microstructure of the closed cell aluminum foam (ALPORAS).

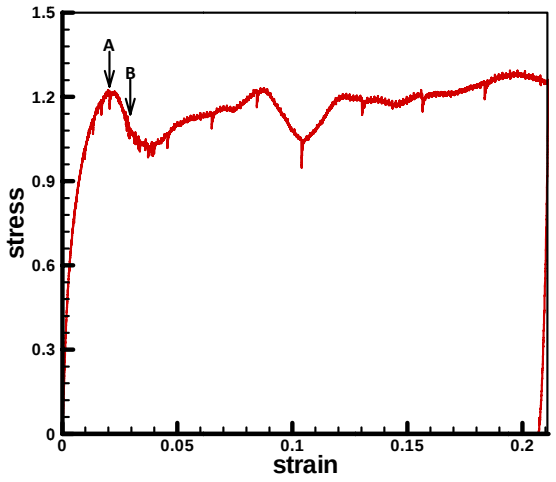

Figure 2.7 The stress and strain curve of the uniaxial compression test of aluminum foam (ALPORAS).

Surface images were recorded by a commercial video camera with a CCD array of 1024×1528 pixels. A wide aperture lens (F1.4) with extended depth of field was used with the camera. Two fiber optic light sources were used to provide oblique white light illumination and shadow reduction. The deformation process of the foam is recorded by a sequence of images with resolution of 60μm/pixel. The captured images are analyzed by the DIC subset method described in previous sections. The average size of the cellular is around 3 ~4mm and the material exhibits non-uniform, heterogeneous deformation during the compression test.

As shown in the Fig.2.7, the stress has a sudden drop with incremental strain at the stage A-B following the nominal plateau stress, and both the stress/strain relation and the corresponding effective strain map (Fig.2.8.a) have indicated that highly localized deformation occurred at this stage. The details of such phenomena and deformation mechanism are given elsewhere [8]. The stage A-B has been marked in Fig.2.7 by two arrows and the effective strain map is obtained by analyzing the images at stage A and B. Based on the gray intensity distribution and the cellular size, the sequence parameters in DIC technique are chosen as: L_g=10pixels, L_b=16pixles, L_s=40pixles. In the post DIC process, the biquadratic polynomial is utilized to fit the discrete displacement fields over the strain gauge length. As shown in the Fig.2.8.a, most of the high strain domains are located on the left side of the image, which means the localizations. One part of the localization region has been marked in the Fig.2.8.a with a rectangle, and the relative partial images of these two stages are shown in Fig.2.8.b and c, which are larger than the domain marked in Fig.2.8.a. By observing these two pieces of images and the effective strain map, the localization occurs as

the cavities on the left side collapse during the deformation. Therefore, one of the cavities has been selected to study, which is shown in Fig.2.9. This part of the image is the localization region marked in Fig.2.8.a, corresponding to which the partial images of stage A is shown in Fig.2.9.a and the one of stage B is shown in Fig.2.9.b. The coordinates in X and Y directions are used to oriented the domain in the effective strain map Fig.2.8.a. As shown in the images, the contours of the cavity and the surrounding characters are plotted for both stage A and B. To confirm that the localization occurs at the cavity collapse, Fig.2.9.c shows the contour of stage B is on the top of stage A image and the characters are aligned on the right side of the cavity; while, the Fig.2.9.d shows contour alignment on the other side of the cavity.

According to these two character alignments, it indicates that the localization is because of the deformation of the cavity. The contours of the cavity in stage A and B are plot together and shown in Fig.2.9.e, in which the background grid spacing represents the pixel unit. There is a rectangular window marked in the Fig.2.9 and the height of this window is one correlation window height L_b and the width of the window is the apparent localization width L_{app} by DIC displacement result, which is along the sequence sub-windows in this row. Based on the contour in Fig.2.9.e, the cavity inside of the marked window has around 20 pixels difference between stage A and B. Therefore, we could assume the exact localization width L_0 is 20pixels. The DIC displacement components along this row of sub-windows have been plotted in Fig.2.10.a and b, in which the X coordinates same as the one in Fig.2.8.a and Fig.2.9, are used to track the site and width of the apparent localization. The displacement results indicate that the band width is 4 L_g and the estimated lower and upper bound of the band width should be 14~24 pixels, which is the result from Eqn.1.b by plugging the other

parameters into the equation. This evaluation is much closed to the width observed from the images. The displacement jump across the localization is approximately 6.7 pixels and the average strain inside of the localization should be 33.5%, if we assume that parameter L_0=20pixels and ε_{xx} is the dominant strain component inside of the localization. However, the effective strain of this region is shown in Fig.2.10.c with maximum strain level of 14% lower than the actual strain, and the apparent width of this localization band about 80 pixels, which follows the estimation of Eqn.6.

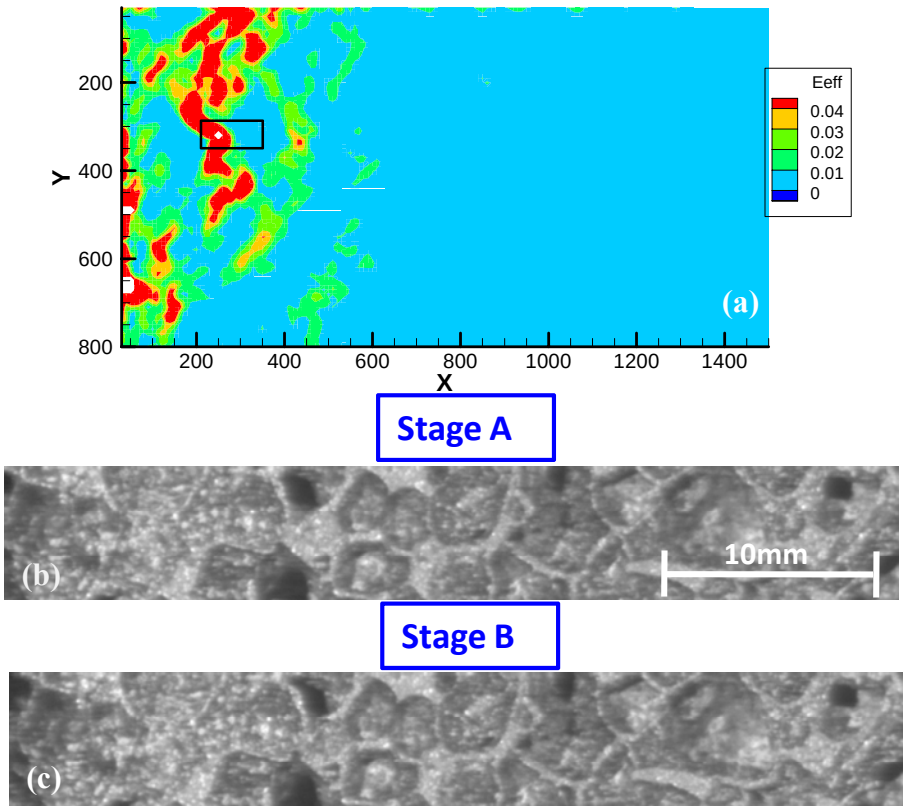

Figure 2.8 (a) incremental strain map of the loading stage A-B, at which highly localized deformation occurred. (b) and (c) are the image of the localization at stage A and B, which is marked in (a).

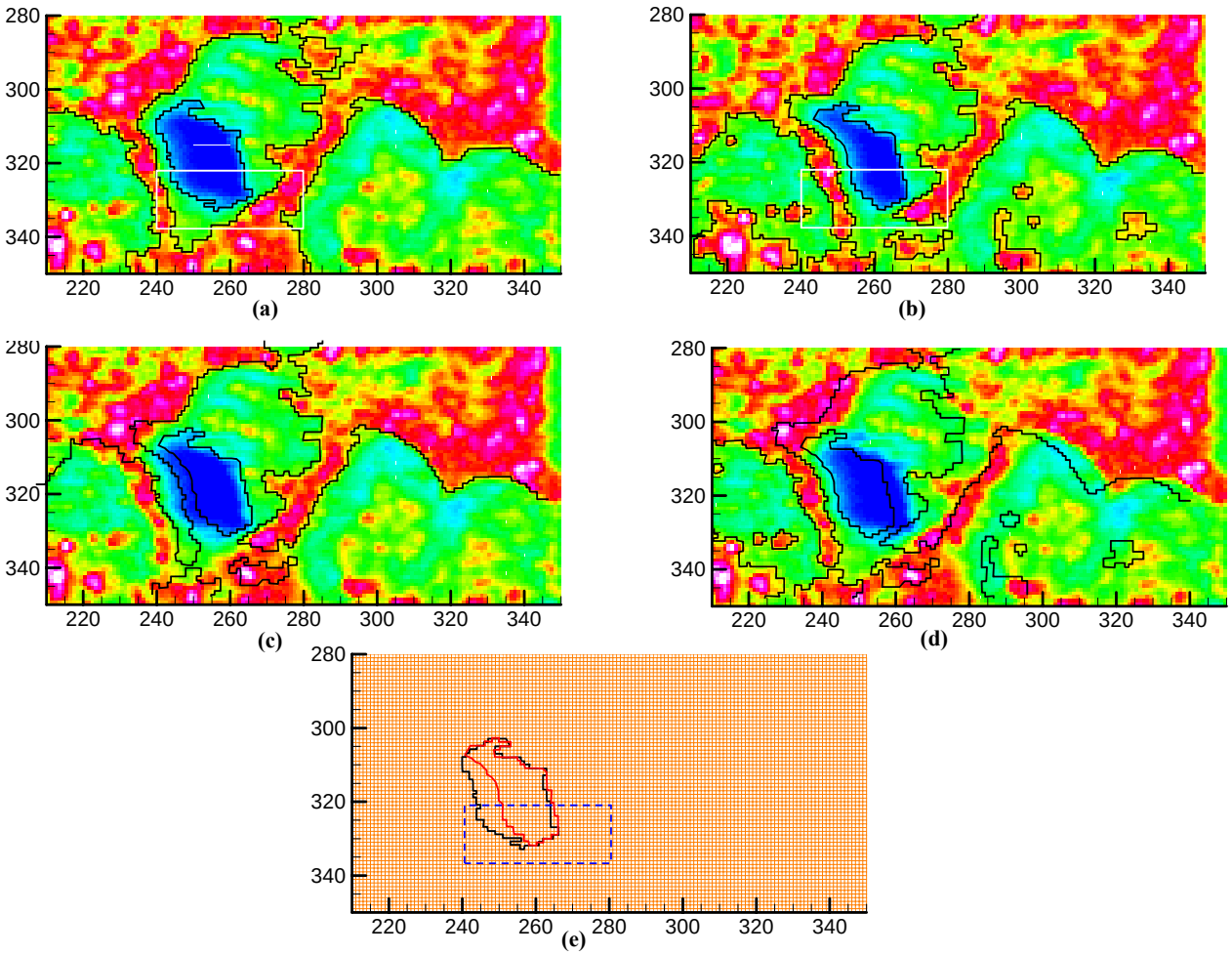

Figure 2.9 Partial image of highly deformed localization: (a) The partial image at stage A; (b) the partial image at stage B; (c) and (d) the contour of stage B is aligned with both sides of the localization at stage A. (e) Highly deformed cavity at stage A and B is plotted on top of each other; inside of the marked window, it shows that there around 20 pixels difference.

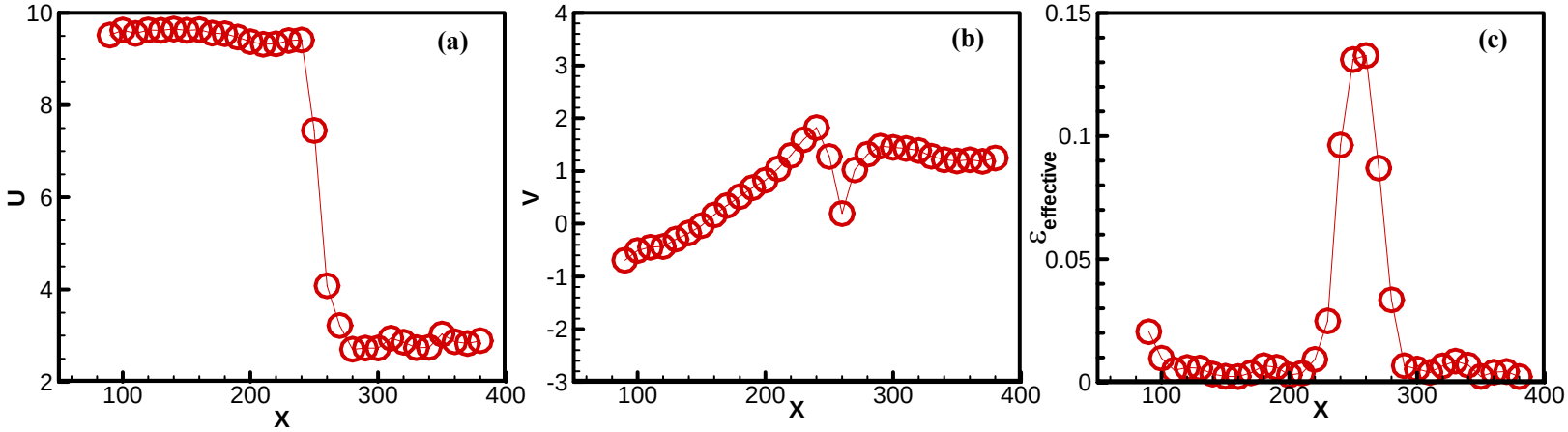

Figure 2.10 The displacement components along the row of sub-windows shown in Fig.9 are presented in (a) and (b). The effective strain and apparent band width is shown in (c), which follows the estimation of Eqn. 6.

Based on this case, it shows that the DIC displacement result is critical to evaluate the localization width and the resolution of this method depends on the grid spacing L_g. The apparent band width from the strain result is based on the strain gauge length and the evaluation from the displacement results. The strain level is determined by several factors, such as the strain gauge length, the fit function and the noise level. Usually, it is difficult to evaluate the apparent width of localization by DIC strain result, because the noise or the choice of the strain gauge length could introduce fluctuations in the strain plot, which could result into errors in the evaluation process.

2.6 CONCLUSION

The measurement of localized deformation by DIC subset method has been studied in this work. Based on the investigation of a sequence of localization bands with different artificial width, it indicates that DIC technique overestimates the width of the localization, which is the result from several length parameters used in this technique. By exploring the parameters' contribution during the DIC process, an empirical equation has been summarized and the spacing between two continuous sub-windows L_g is very important to determine the resolution. The width and strain level within the localization are biased in the strain map obtained by post DIC process, in which the width evaluation has been effected by the strain gauge length and the strain level is much lower than the exact value. Also, the strain map just could qualitatively highlight the localization but over estimate the band width especially for the thin localization band. Generally, to understand the localization character by DIC technique, we have to focus on specific localization and analyze the DIC result manually to explore the corresponding properties.

2.7 REFERENCE

[1] W.H. Peters and W.F. Ranson, "DIGITAL IMAGING TECHNIQUES IN EXPERIMENTAL STRESS ANALYSIS.," *Optical Engineering*, vol. 21, 1982, pp. 427-431.

[2] T.C. Chu, W.F. Ranson, M.A. Sutton, and W.H. Peters, "APPLICATIONS OF DIGITAL-IMAGE-CORRELATION TECHNIQUES TO EXPERIMENTAL MECHANICS.," *Experimental Mechanics*, vol. 25, 1985, pp. 232-244.

[3] A. Antoniou, P. Onck, and A.F. Bastawros, "Experimental analysis of compressive notch strengthening in closed-cell aluminum alloy foam," *Acta Materialia*, vol. 52, 2004, pp. 2377-2386.

[4] Y. Wang and A.M. Cuitino, "Full-field measurements of heterogeneous deformation patterns on polymeric foams using digital image correlation," *International Journal of Solids and Structures*, vol. 39, 2002, pp. 3777-3796.

[5] J. Rethore, F. Hild, and S. Roux, "Shear-band capturing using a multiscale extended digital image correlation technique," *Computer Methods in Applied Mechanics and Engineering*, vol. 196, 2007, pp. 5016-5030.

[6] J. Kang, T. Schmidt, M. Jain, and D. Wilkinson, "Microscopic material characterization using SEM topography images correlation," *SEM Annual Conference and Exposition on Experimental and Applied Mechanics 2006, Jun 4-7 2006*, pp. 1389-1395.

[7] W. Tong, "Detection of plastic deformation patterns in a binary aluminum alloy," *Experimental Mechanics*, vol. 37, 1997, pp. 452-459.

[8] A. Bastawros, H. Bart-Smith, and A. Evans, "Experimental analysis of deformation mechanisms in a closed-cell aluminum alloy foam," *Journal of the Mechanics and Physics of Solids*, vol. 48, 2000, pp. 301-322.

[9] M.A. Sutton, W.J. Wolters, W.H. Peters, W.F. Ranson, and S.R. McNeill, "DETERMINATION OF DISPLACEMENTS USING AN IMPROVED DIGITAL CORRELATION METHOD.," *Image and Vision Computing*, vol. 1, 1983, pp. 133-139.

[10] P. Cheng, M.A. Sutton, H.W. Schreier, and S.R. McNeill, "Full-field speckle pattern image correlation with B-spline deformation function," *Experimental Mechanics*, vol. 42, 2002, pp. 344-352.

[11] H.W. Schreier, J.R. Braasch, and M.A. Sutton, "Systematic errors in digital image correlation caused by intensity interpolation," *Optical Engineering*, vol. 39, 2000, pp. 2915-2921.

[12] B. Bay, T. Smith, D. Fyhrie, and M. Saad, "Digital volume correlation: Three-dimensional strain mapping using X-ray tomography," *Experimental Mechanics*, vol. 39, 1999, pp. 217-226.

[13] A. Antoniou, A. Bastawros, and B. Biner, "Experimental observations of deformation behavior of bulk metallic glasses during wedge-like cylindrical indentation," *Journal of Materials Research*, vol. 22, 2007, pp. 514-524.

[14] H. Bruck, S. McNeill, M. Sutton, and W.I. Peters, "Digital image correlation using Newton-Raphson method of partial differential correction," *Experimental Mechanics*, vol. 29, 1989, pp. 261-267.

[15] Y. Wang and A.M. Cuitiño, "Full-field measurements of heterogeneous deformation patterns on polymeric foams using digital image correlation," *International Journal of Solids and Structures*, vol. 39, 2002, pp. 3777-3796.

CHAPTER 3: EXPERIMENTAL CHARACTERIZATION OF PLASTIC FLOW IN DUCTILE METALS BY WEDGE-LIKE INDENTATION

3.1 ABSTRACT

A wedge-like cylindrical indentation experiment is employed to study the deformation and flow characteristics in ductile metals. Two sets of materials, annealed polycrystalline copper with 17~37μm grain sizes, and aluminum 6061-T6 alloy are examined to represent a wide range of FCC metals with different hardening exponent, and flow stress. Digital image correlation technique is used to follow the evolution of the deformation and flow field underneath the indenter. The distribution of the effective strain in the plastic zone has unique correlation with the radial distance and the self-similarity manner has been observed. FEM numerical model and Cavity expansion model are discussed to evaluate the experimental estimation.

3.2 INTRODUCTION

The instrumented depth-sensing indentation technique has been used to probe the mechanical properties of bulk materials at the microscopic scale [1,2] or at the submicron scale [3,4] for many years. The underlying principle is to correlate the average contact pressure or "hardness" to the flow stress [2,5] and modulus [6]of the material. Despite the improved resolution and accuracy of the indentation technique [4], the details of elastic-plastic process zone remained to be explored via finite element analysis, employing phenomenological constitutive relations and hinges upon macroscopic matching of the force-depth indentation curves [7-9].

Limited details of the deformation field underneath the indenter have been reported via sectioning a macroscopic indentation [10,11] or indent a bonded interface [11] then reveal the deformation zone by etching. The deformation field underneath spherical pyramidal indenter on annealed brass was shown to be radial and hemispherical [10]. Such deformation pattern is in agreement with the simplified Johnson cavity expansion model [5] for the indentation field, employing Hill's solution [12]. Alternatively, the sectioned surface is probed by an array of micro- or nano-indentation to map the spatial distribution of the current level flow stress and the corresponding plastic strain (given that a correlation between the measured flow stress and the effective plastic strain is available). The iso-strain contours underneath the pyramidal indentations showed that the deformation zone has been elongated along the loading direction [13,14] and materials' mechanical properties play different roles in the shape of the strain contours [14]. Additionally, using the orientation imaging method inside SEM on a sectioned surface of Vickers indentation on a single grain copper [15] showed that the evolution of crystal lattice rotation was not self similar, with the maximum lattice rotation occurring at the flanks of the indenter.

However, none destruct measurement of the deformation filed underneath indenter has been reported. This work applies the recently developed experimental protocol [16,17] of wedge-like indentation and digital image correlation to record the evolution of the plastic deformation and study the flow field in ductile metals. First, details of the experimental setup and the test materials are given in section2. Summary of the analytical and numerical models is shown in section 3. Experimental observations compared with FEM simulation results are

indicated in section 4. Discussion section elaborates the details of the plastic flow and deformation mechanisms.

3.3 EXPERIMENTS

Material Models

Two sets of FCC metals are utilized to represent a broad range of material properties including flow stress and hardening characteristics. The first set is a commercial aluminum alloy 6061-T6, having an average grain size of 85μm. The second set is oxygen free polycrystalline copper with 17 μm grain size. A beam type configuration is utilized with cross section of 3.3mm wide and 7.5mm deep in the indentation direction, and length of 25mm. The Al6061 alloy specimen was tested in the as received condition. The copper specimens were tested in the as the received conditions (Cu-I) as well as after annealing to 400 °C (Cu-II) and 600 °C (Cu-III) for 2 hrs to modulate the grain size and the hardening characteristics. Summary of the tensile and/or compressive test results are summarized in Table 1 for elastic modulus, yield stress, stain hardening exponent, and the average grain size for each treatment condition.

The specimen front surface, normal to the indent plane is mechanically polished to 0.5 μm finish. Light etching in 5% Nitric acid is used to reveal the surface grains and decorate the surface for the digital image correlation technique. The light etching has provided excellent random speckle pattern on the specimen surface.

Experimental Setup

An Instron 8862 servoelectric loading frame is used to do the cylindrical indentation experiments, with loading rate of 1 μm/s. The loading fixture, shown in Fig.3.1 [17], ensures that the contact line between the indenter and specimen top surface is perpendicular to the front plane of the sample. A SiC wedge like cylindrical indenter with root radius, R= 0.8 mm is used in the experiment. A travelling microscope having 5x objective lens and a progressive-scan camera (SPOT Insight CCD array of 2048x2048) is utilized to image the surface evolution of the process zone underneath the indenter. The corresponding field of view is 2 mm×2 mm with 1 pixel/μm resolution. A combination of through the lens and external oblique unpolarized white light are used to illuminate the specimen surface. Images are collected every 0.5 s during the loading and unloading phase.

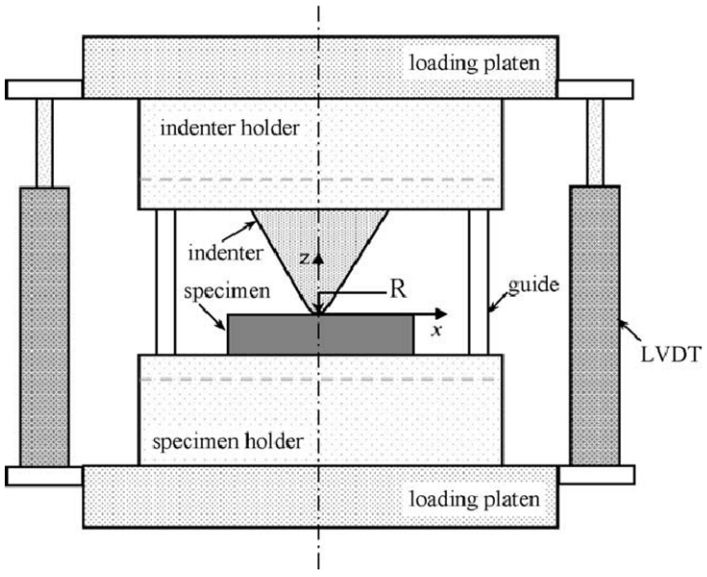

Figure 3.1 Schematic of the loading fixture for cylindrical indentation test.

Digital Image Correlation Technique

A Digital Image Correlation (DIC) technique, developed in house, is used to analyze the deformation field on the surface underneath the indenter. Pairs of images of the current deformed configuration and the original undeformed configuration are correlated together to find the nodal displacement over a uniform grid points. Each pair of images was divided into a set of 40-pixel square sub-windows, with a 10-pixel overlap. The developed technique has two step searches; (1) a coarse search is based on maximizing the intensity correlation coefficient between the sub-windows to within one pixel, and (2) a fine search routine, using expanded 2-D eignvalues of the local match, coupled with iterative Newton-Raphson method to achieve 0.01 pixel resolution. Details of the technique could be found elsewhere [18,19]. The acquired nodal displacement represents the average displacement of each sub-window. Spatial displacement gradients relative to the unreformed configurations are acquired from a bilinear fit of the nodal displacement over 5x5 local nodal grid, or the width of the correlation window to eliminate the high frequency digital noise, without obscuring any displacement localization. The selection of such local nodal grid defines the local strain gage length is about 40 μm, over which the strain is averaged. Therefore, while we acquired nodal displacement and strain values every 10□m, however each of these values represents an average over 40μm window. The acquired displacement gradients are used to calculate the in-plane Lagrangian strain components at the nodal grid.

3.4 ANALYTICAL AND NUMERICAL MODEL:

A modified cavity expansion model has been developed [5] (Appendix 1) about the wedge indentation in an infinite elastic perfectly-plastic body, which is based on the von-

Mises yield criterion. By considering both material parameters and the geometry of the indenter, it derived the relation that

$$\frac{2\sqrt{3}E}{\pi Y}\tan\beta = (5-4\nu)(c/a)^2 - 3(1-2\nu) \tag{1}$$

And about incompressible material $\nu = 0.5$, it yields the expression:

$$\frac{\bar{p}}{Y} = \frac{F}{2atY} = \frac{1}{\sqrt{3}}\left[1 + \ln\left(\frac{2E\tan\beta}{\sqrt{3}\pi Y}\right)\right] \tag{2}$$

where E is the Young's modulus, Y is the uniaxial yield strength, $\bar{p}$ is the mean pressure in the core , c is the plastic zone size, a is the contact radius, β is the angle between the indenter flank and the surface, t is the thickness of the specimen and ν is the Poisson's ratio.

Based on the force equilibrium, the relation of the applied force and plastic zone size has been developed, in which the plastic zone is assumed to be semi cylindrical cap and boundary conditions has been substituted. More details are shown in the Appendix 2.

$$F = 2\bar{p}at = 2\int_0^{\pi/2}\sigma_r \cdot \cos\theta \cdot t \cdot c \cdot d\theta = 2 \cdot c \cdot t \cdot \sigma_r = \frac{2cYt}{\sqrt{3}} \tag{3}$$

where F is the load level , c is the elastic-plastic boundary and t is the thickness of the specimen.

A closed-form analytical solution for the elastic-plastic stress, strain, and displacement component of an internally pressurized open-ended thick-walled cylinder is developed [20] by utilizing Hencky's deformation theory and von-Mises yield criterion. This analytical solution has following assumptions: (1) the material homogenous and

incompressible,(2) isotropic hardening, (3)small strain, (4) no body force acting, (5) loading proportionally without unloading, (6) elastic power-law plastic model of stress-strain relation, and (7) plastic zone is a cylinder. By setting stress components as basic unknowns and introducing a modified Nadai's auxiliary-variable φ, at give pressure, the functional relationship between φ and radius *r* is established within the plastic zone. Additionally, based on the boundary conditions and the compatibility equation, the stress components are expressed as a function of φ . According to the general solution in the plastic domain, the stress components ε_r , ε_θ and ε_z are proportional to $r^{-\frac{2}{N+1}}$, and $0 \le N \le 1$. This relationship indicated that the strain distribution inside of the plastic zone is effected by the hardening exponent value N for the open-ended thick-walled cylinder, of which the stress-strain relation followed the elastic power-law plastic mode.

There have been various finite element simulations exploring the plastic distribution associated with deformation mechanism [8] and the influence of the yield strength *Y* and hardening exponent *n* on the shape of the plastic strain contour [21]. In this study, we use Ramberg-Osgood constitutive relation to simulate the wedge-like cylindrical indentation experiment, which are used to examine the macroscopic response and the strain distribution in the plastic zone. Three-dimensional (3D) geometric models for all of the copper specimens in the experiments are established using the ABAQUS finite element package. The dimension of the sample is the same as the experimental samples and only one quarter of the sample was analyzed. The materials properties are input by the parameters which were listed in Table.1 and the analytical rigid indenter with frictionless contact are assumed to simplify

the contact analysis. 8-node linear hexahedral elements are used and mesh refinement is increased within the domain underneath indenter.

	E (Gpa)	Y(Mpa)	n	dg (μm)
Al 6061	66	260	15	85
Cu I	121	180	10	17
Cu II	118	46	2.3	28
Cu III	112	40	1.9	37

Table 3.1 Relevant mechanical properties of the Al60601 alloy and three copper specimens, which were obtained from the uniaxial loading tests .

3.5 EXPERIMENTAL AND NUMERICAL RESULTS

Macroscopic Trends

The measured load-indentation depth curves of the aluminum alloy and three copper samples with same indenter radius R of 0.8 mm are summarized in Fig.3.2, in which the elastic stiffness of the loading fixture has been removed. A full surface contact was established when the linear elastic deformation started, at which zero indentation depth of the load-indentation depth curves were set. The comparison of the experimentally measured macroscopic response with FEM results and analytical solution based on Johnson's cavity expansion model are shown in Fig.3.2a and Fig.3.2b respectively, in which both of them match the experiment measurements well except the analytical solution underestimates the load levels with increment of the indentation depth. The load-indentation depth relation of the analytical solution is based on Eq.2, in which there is no strain hardening considered and incompressible material is assumed.

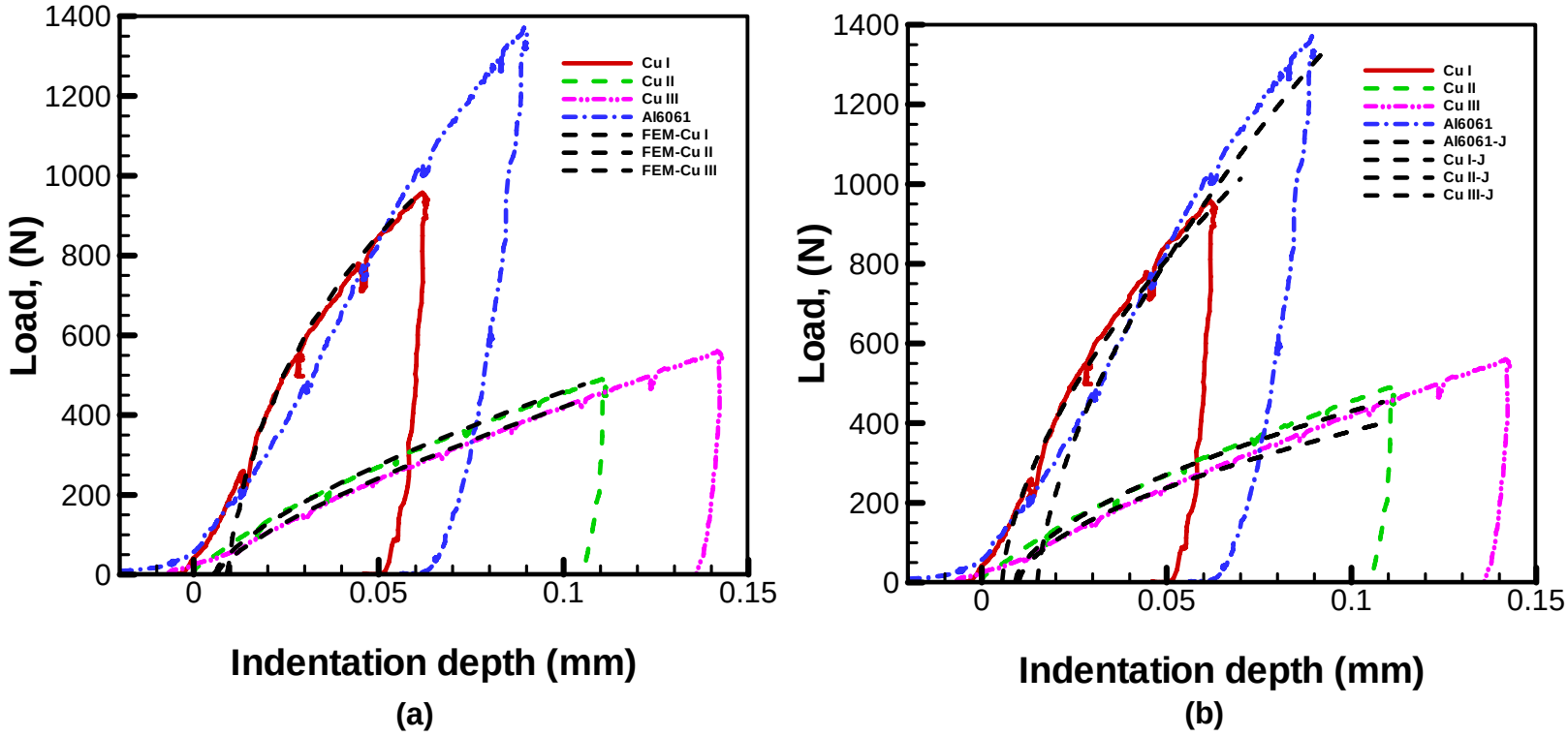

Figure 3.2 Experimental measurements of Force-indentation depth curves for Aluminum and three Copper samples under cylindrical indentation test with radius, R=0.8mm; (a) Comparison of the experimental and FEM numerical macroscopic responses for three different Copper specimens; (b) Comparison of the Johnson's analytical solution and the experimental measurements.

Effective Strain Evolution

According to the images that have been taken during the course of the indentation experiment, the 2D in plane strain maps were plotted based on the DIC analysis. From the in-plane strain components ($\varepsilon_{xx}, \varepsilon_{yy}, \varepsilon_{xy}$), a measure of the effective strain can be obtained by:

$$\varepsilon_{eff} = \sqrt{\frac{2}{3}\varepsilon_{ij}\varepsilon_{ij}} \tag{4}$$

The load-indentation depth curves of Cu I and Cu II are shown in Fig.3. 3a with three loading stages marked on each plot having similar indentation depths. Fig.3. 3b-3d and Fig.3. 3e-3f show the evolution of the in-plane effective strain of Cu I and Cu II respectively at different stages. The blank domain in the effective strain maps of Cu I means that there are no analysis data in those regions, which could be caused by the out of focus of the image by large out of plane deformation underneath the indenter or dust on the camera. As shown in Table.1, Cu I that was tested as received condition has higher yield strength and lower strain hardening capability compared with Cu II that was annealed under 400°C for 2 hours before indentation test. As can be seen in the effective strain maps, the total accumulated effective strain of Cu I around the indenter is much lower than the one of Cu II at given indentation depth.

Although the macroscopic response and local strain levels are much different for these two copper samples, the shapes of these two sets of strain contours keep similar during the plastic deformation propagations, which look like a partial ellipse. To explore more details of the shape of the plastic zone, the ratio of the height to width of the plastic zone at

different loading stages has been investigated for all of the indentation tests, including Al6061 and Cu I, II, III specimens. Because of the resolution of the DIC technique which is controlled by the noise introduced by the camera, illumination and vibration et al, we set 0.5% effective strain level as the elastic-plastic boundary of the deformed field. The height, *h* and the width, *w* of the plastic zone are defined in Fig.3.3e. The variation of the yield strength and the *h/w* aspect ratio is plotted in Fig.3.4a, which indicates that the ratios of the height to width of all of the copper specimens are around 1, except the one of Al6061 alloy is around 0.8. The dependence of the plastic zone size and the load levels for different specimens is shown in Fig.3. 4b, in which the load per unit thickness is normalized by the uniaxial loading yield strength for each specimen and the plastic zone size is averaged from angle 0° to 30° as shown in Fig.3.3b. The linear relationship between the normalized load level and averaged plastic zone size is shown in the plot for each sample and the slop of the linear fit is around 0.81.

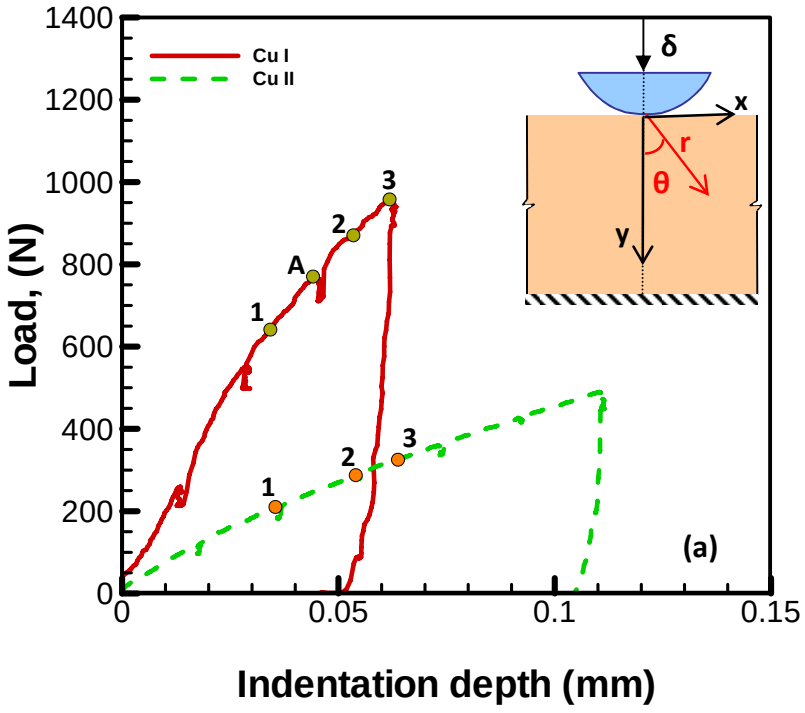

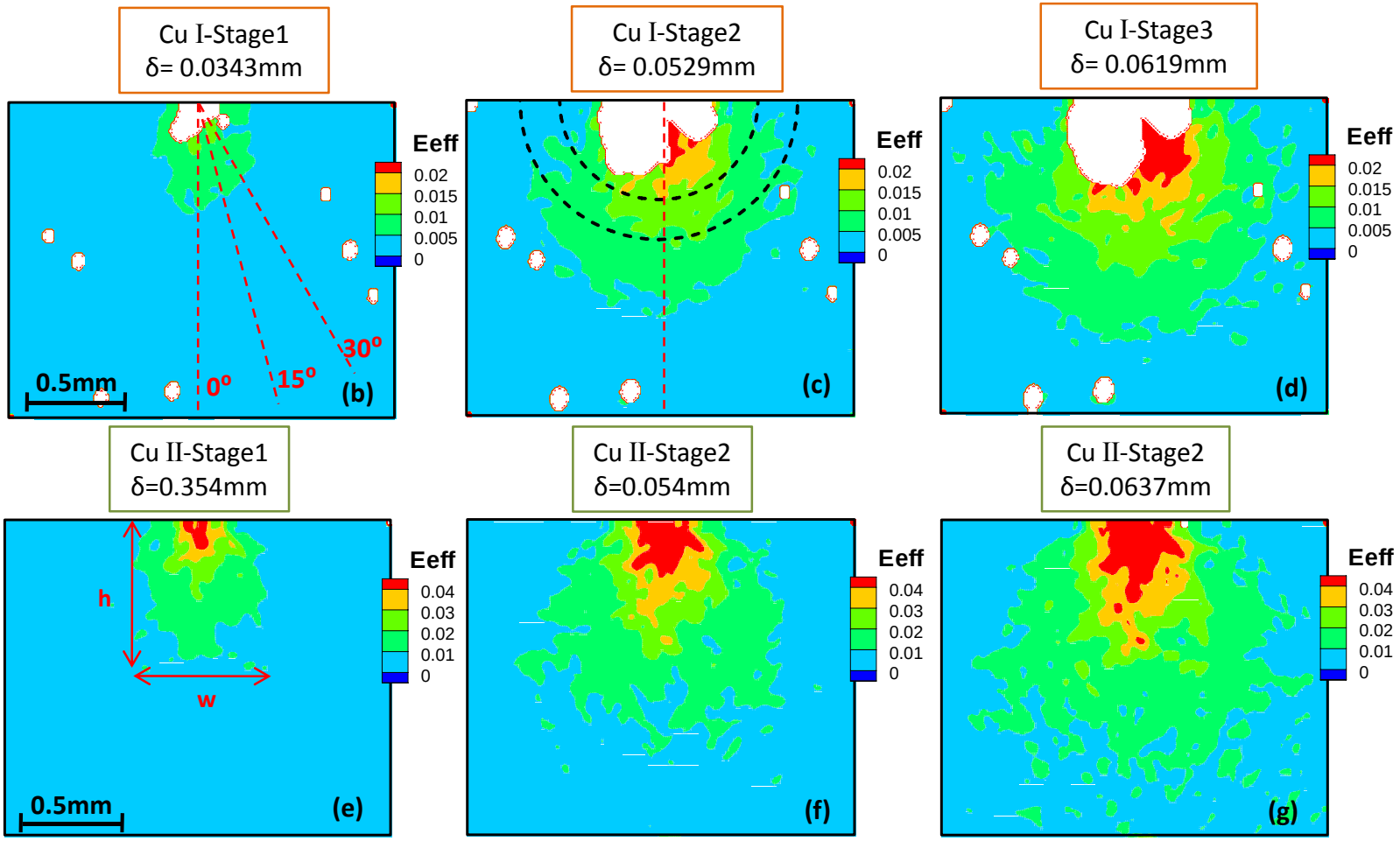

Figure 3.3 Effective strain maps of three different load stages were plotted for Cu I and Cu II. (a). The three different load stages of Cu I and Cu II were marked on the experimental force-indentation depth curves respectively. (b)-(d) Effective strain maps of Cu I; (e)-(g) Effective strain maps of Cu II;

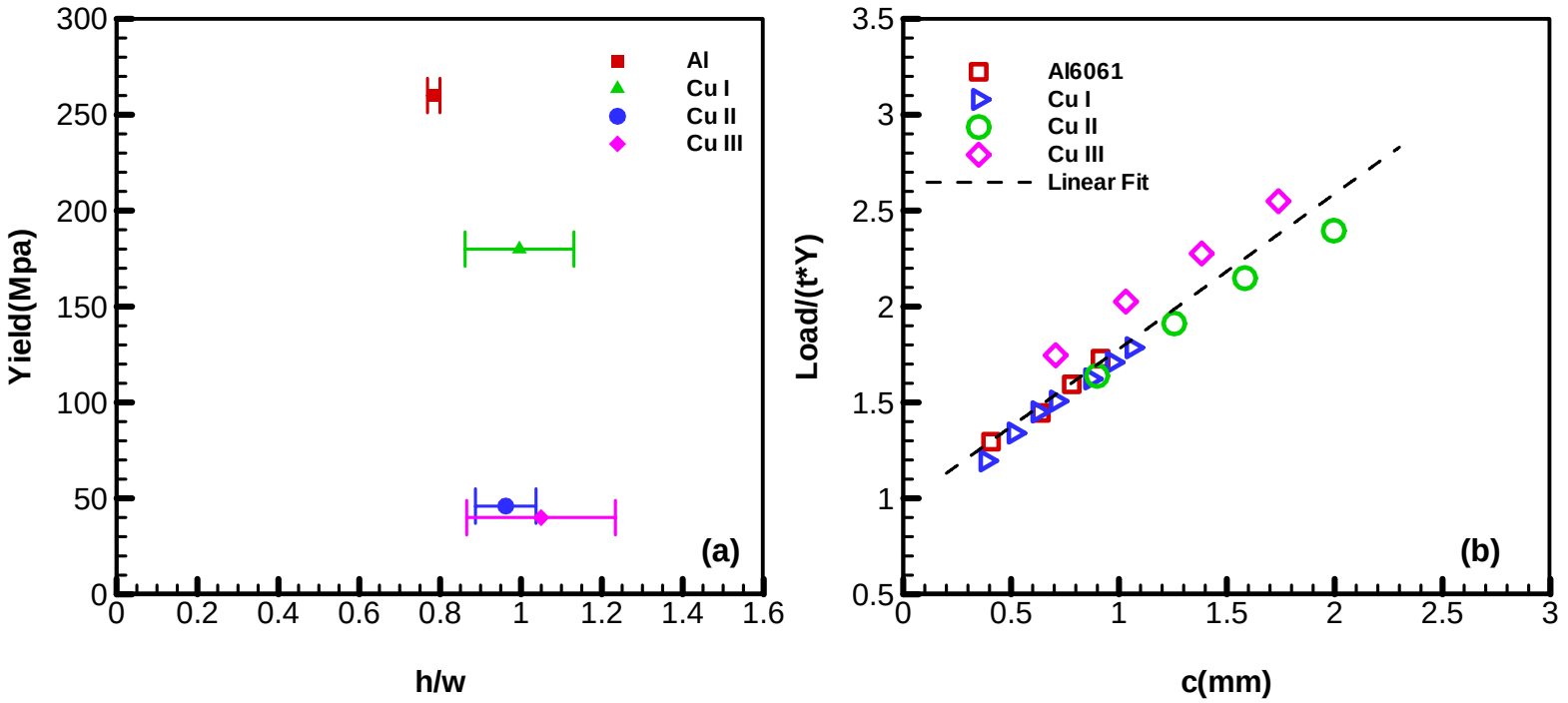

Figure 3.4 (a) The ratio of height to width of plastic zone for all of the specimens. (b) Dependence of the plastic zone size on the load per unit thickness which was normalized by the yield strength Y.

Radial Dependence of the Effective Strain

Beside of the shape and plastic zone size, the dependence of the effective strain on the radial line is another interesting part in this work, which indicates the fact of strain decay underneath the indenter. About Cu I and Cu II, as defined in Fig.3.3a, 3b, the radial lines were extracted from the effective strain maps in different angle θ directions at different load stages. The effective strain of Cu I and II for 3 different loading stages marked in Fig.3. 3a are plotted as a function of normalized radial distance *r*/c in Fig.3.5a and Fig.3.5c respectively, in which the radial lines are along the direction of 0° angles. The normalization parameter *c* is the elastic-plastic boundary at every loading stage. As shown, each of the specimens has their own unique correlations between the effective strain and normalized radial distance at different loading stages, which indicates the self-similar property of the deformation field in the cylindrical indentation. At given indentation depth or loading stage, the normalized radial plots of the effective strain of these two copper along different directions are shown in Fig.3.5b and Fig.3.5d, in which the correlations between the effective strain and normalized radial distance keep same as shown in Fig.3.5a and Fig.3.5b. Therefore, it reveals that for each specimen there is a unique correlation about the effective strain and normalized radial distance that can describe the strain distribution in the deformation filed of cylindrical indentation, based on the experimental results shown n Fig.3. 5.

To obtain the expression of the effective strain as a function of normalized radial distance in the plastic domain, the experimental measurements shown in Fig.3.5a and Fig.3.5c have been averaged along the direction of 0° angles at different loading stages. The dash line plots in Fig.3.6 a, b show the power fit expression of the experimental results

within plastic zone ($r/c<1$) about Cu I and Cu II, in which the effective strain of Cu I has the proportional relationship to the normalized radial distance with power exponent -1.55 and the one of Cu II is -1.302. According to the FEM simulation results, the effective strain of Cu I and II along 0^{o} angle directions at different loading stages are plotted to the normalized radial distance in Fig.3.6a and Fig.3.6b with different symbols, which indicates the same self-similarity as that shown in the experimental results. The effective strain power fit for the FEM radial line plots of Cu I within the plastic zone has the power exponent -1.68 and Cu II has the power exponent of -1.474, both of which are higher than the corresponding experimental measurements. As discussed in Section 3.3, an exact solution for the open-ended cylinder tube analogous to the cylindrical indentation has been developed, in which the material is assumed to be elastic power-plastic and incompressible. This analytical solution states that the effective strain in the plastic zone has the proportional relation to the radial distance with power exponent, $-\frac{2}{N+1}$ where N is the strain hardening exponent and $0 \le N \le 1$. Based on this relation, the analytical solutions by substituting the corresponding N value for each specimen are shown in Fig.3.6a and Fig.3.6b with solid lines for Cu I and II. Compared with the numerical and analytical solution, the experimental measurements have lower accumulated effective strain at given radial distance in the plastic zone , but similar effective strain levels as those of FEM simulation results outside of the plastic zone, where $r/c \ge 1$.

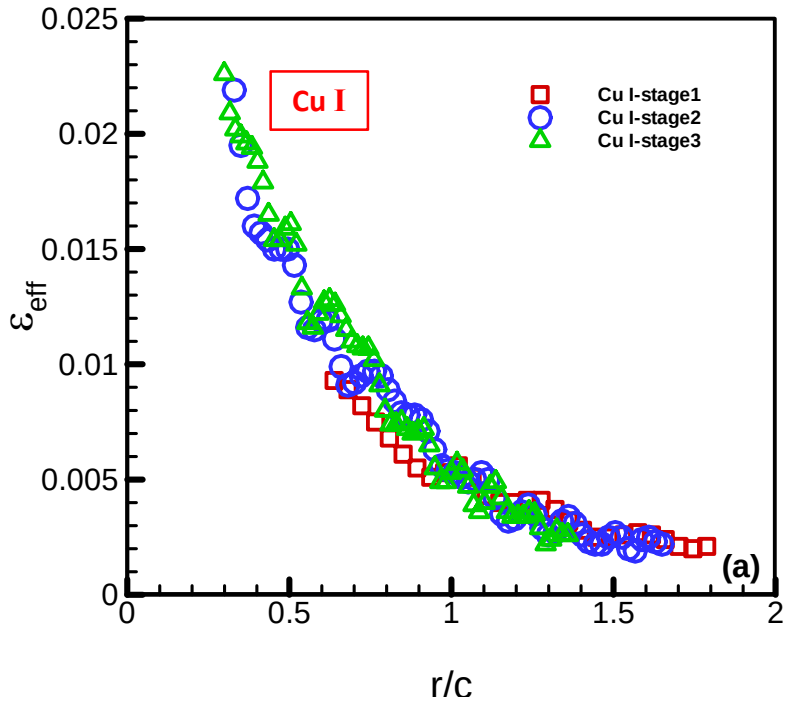
Cu I
Cu I-stage1
Cu I-stage2
Cu I-stage3
(a)
ε_{eff}
r/c
0.025
0.02
0.015
0.01
0.005
0
0
0.5
1
1.5
2

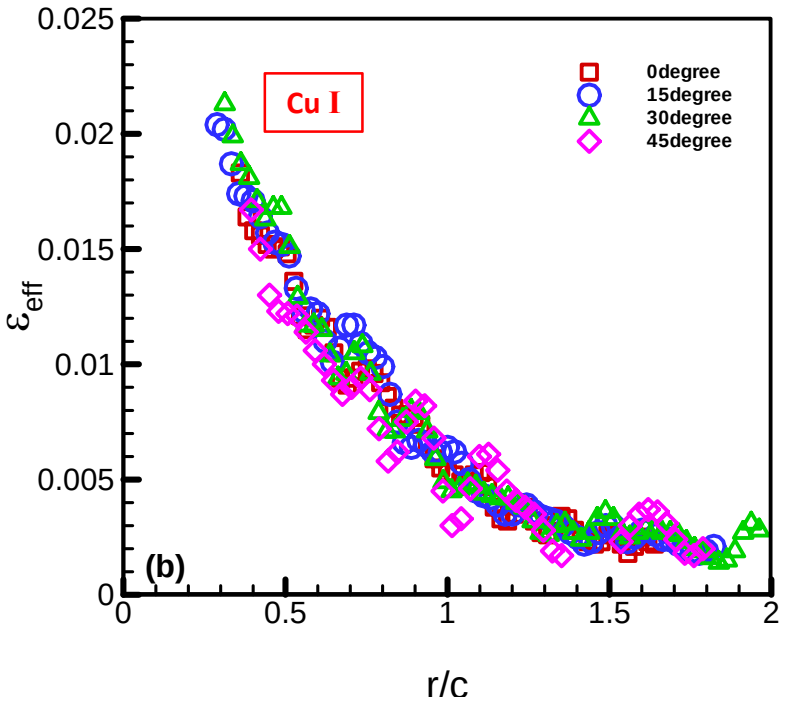
Cu I
0degree
15degree
30degree
45degree
(b)
ε_{eff}
r/c
0.025
0.02
0.015
0.01
0.005
0
0
0.5
1
1.5
2

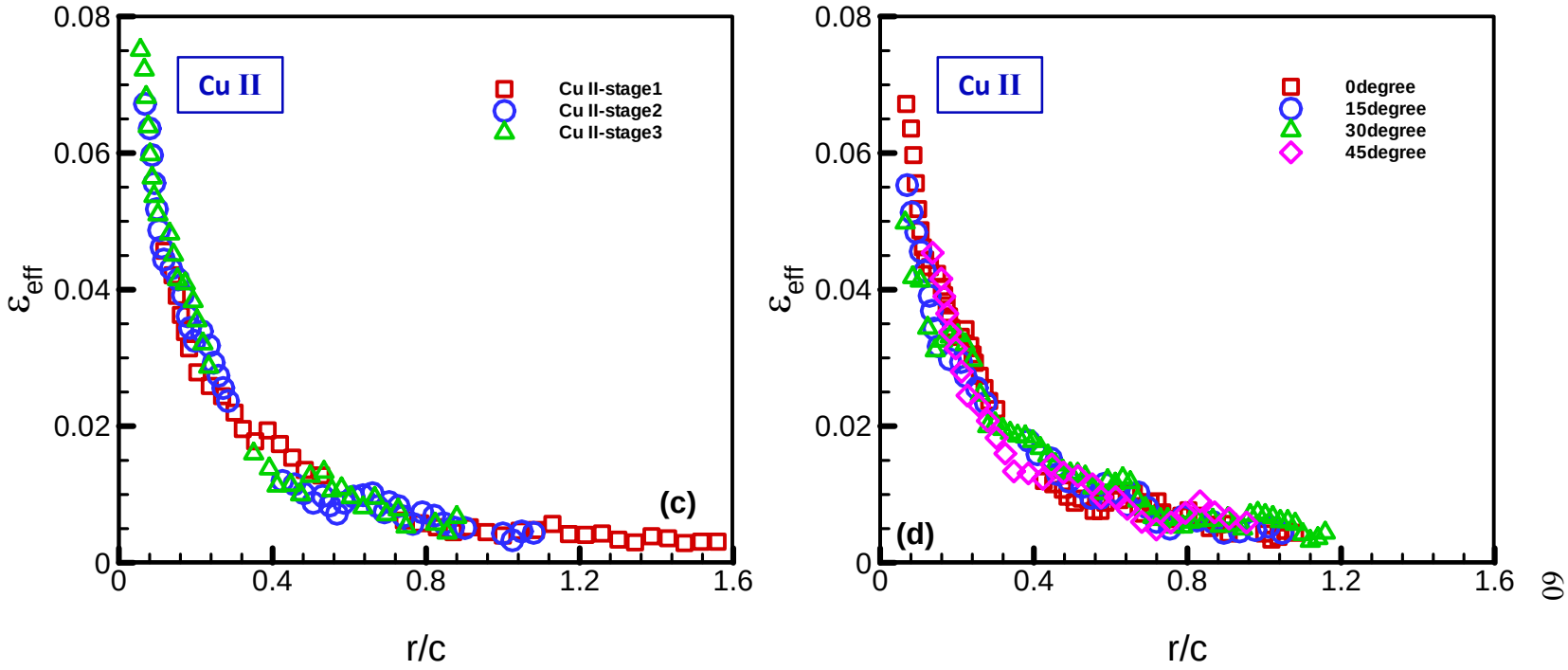

Figure 3.5 (a),(c) Normalized radial line plots along 0^0 angle of the effective strain of Cu I and Cu II for different stages (1-3) marked in Fig3. a; (b),(d) Normalized radial line plots of effective strain along 0^0 , 15^0 , 30^0 and 45^0 degrees of Cu I and Cu II at their own stage 2.

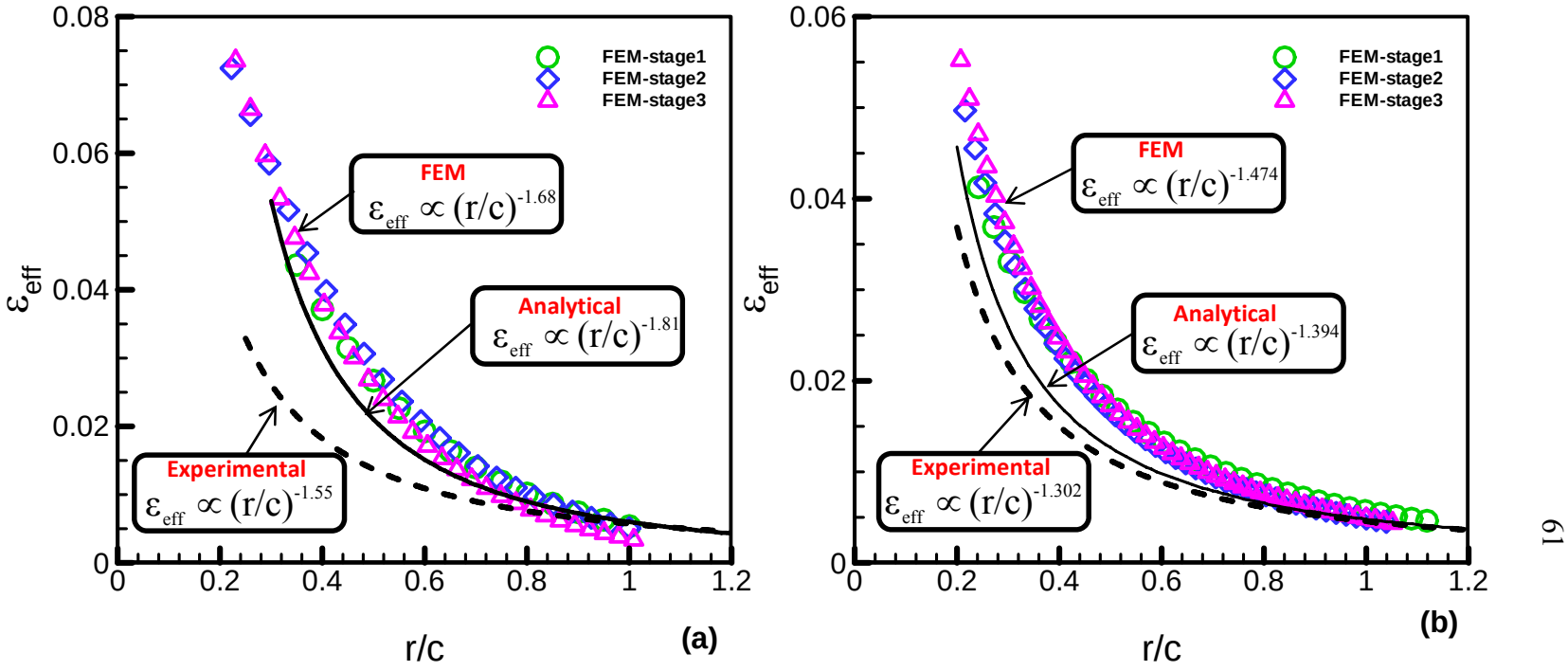

Figure 3.6 Comparison of the radial line plots along 0^0 angle of Cu I **(a)** and Cu II **(b)** effective strain for the average experiment measurements, FEM simulation results and the Analytical solution [20]. The power fit exponents were marked for each curve.

Circumferential Dependence of the Effective Strain

The distribution of the effective strain closed to the indenter has been revealed from the circumferential plots with different radii. The center of the circumferential line is located at the indenter tip and the variation of in-plane total strain vectors are plotted on the reduced Mohr-plane (ε_{xy}, $(\varepsilon_{xx}-\varepsilon_{yy})/2$) at different loading stages, which is a function of angular position measured from θ=-90° to 90° as shown in Fig.3.3b. The distributions of the strain vectors predicted by the experimental measurements are plotted in Fig.3.7, which is about Cu I and Cu II at $r = 300,400,500$ and 700 μm, for the different loading levels. Since the circumferential lines are extracted at different radii with various strain state, the distribution of the in-plane total strain vectors will in essence show the shape of the potential function, which have the same shape as a yield function, if associated flow is assumed. For a homogeneous material with a smooth yield surface, a smooth trajectory of the total strain vectors is expected, as the FEM numerical simulation results shown in Fig.3.7. Although the general shape of the trajectories from the experimental measurement can be identified, it still shows that there are some overlaps and clusters along the trajectory of the strain vectors on the reduced Mohr-plane. Such inhomogeneous localization and fluctuations in the distribution of the in-plane strain vectors could be explained by the microstructure effect, so called grain-noise effect [22]. Comparison of the two materials, it shows that Cu I with smaller grain size and higher yield strength has smoother trajectory than that of Cu II, on which there are more irregular clusters.

In spite of the fluctuations on the strain vectors' distribution, the experimental measurements still can present a reasonable estimation, in which the strain vectors are in the

negative direction of $(\varepsilon_{xx} - \varepsilon_{yy})/2$ axis within the angular position at the flank of the indent and the components of ε_{xy} are around zero at the field just below the indenter ($\theta=0^{o}$). As the radius of the circumferential line is small that the field is near the indenter tip, the magnitude of the strain vectors has much higher value of the FEM simulation results than that of the experimental estimations as shown in Fig.3.7a and Fig.3.7d. While as the radius increases, such as shown in Fig.3.7c, r=700μm, for the lower loading stage (stage1 for Cu I), the FEM results and the experimental measurements become closed to each other. This observation agrees with the result indicated in the radial line plot (Fig.3.6) that the strain level from the experimental measurement is lower than that of the FEM results inside of the plastic zone, but coincides with each other in the elastic region. The trajectories plotted in the Fig.3.7 are self-similar at different loading stages, which also confirm the conclusion from the radial dependence of the effective strain in Section of radial dependence of the effective strain.

3.6 DISCUSSION

By utilizing the new experimental setup and the DIC technique, a clear effective strain map has been developed for the deformation field underneath the cylindrical indenter. Based on the contours of the effective strain at different loading stages, it shows that the shape of the deformation zone is not a semi-circle as assumed in the Cavity Expansion model, but a partial ellipse with the h/w aspect ratio around 1. Similar observations have been reported in the Vickers indentation tests [13,14], however, no significant effect of the yield strength and strain hardening exponent on the shape of the plastic zone, which look like similar and have almost same aspect ratio for all of the specimens tested in this study. According to the investigation of the evolution of the effective strain contour, radial

dependence of the effective strain and variation of the in-plane strain vectors along the circumferential direction at different loading stages, the deformation field underneath the cylindrical indenter has the self-similar manner and the flow characterizations keep the same correlation relation at different angular positions.

More details about the plastic zone size have been explored in this study that as indicated from Fig.3.4b, the plastic zone size has a linear relationship to the normalized linear loading levels for all of the specimens with the slop of 0.81. As mentioned in Section 3.2 the simplified analytical solution, Eq.3 also shows the linear relation between the loading level and plastic zone size, in which the slop of the linear relation is $2/\sqrt{3}$ and higher than our experimental observation. This simplified model has been established on the cavity expansion theory by assuming the plastic zone is semi-circle and keep this shape through the thickness of the half-space, however, in reality, the plastic zone size observed in our experiment is located on the front surface of the sample that could amplify the plastic zone size, and the shape of the plastic zone is also different so that the expression of the elastic-plastic boundary surface is not the same one as described in Eq.3. Generally, both of the experimental and the simplified cavity model reveal that the applied load governs the equilibrium at the elastic-plastic boundary and the size of the plastic zone. Similar conclusions were reported for the spherical indentation test [7]. Furthermore, another common observation from the radial dependence of the effective strain and in-plane total strain vectors' trajectory on reduced Mohr-plane shows that the experimental accumulated strain level coincides with the FEM numerical solution in the elastic domain. Fig.3.8 plots the experimental and FEM effective strain variation with the radial distance normalized by

contact radius *a* of Cu I and II at give indentation depth δ, at which the ratio of δ to indenter radius R is around 0.067. According to previous observation, as shown in Fig.3.8, both of the plots indicate that the experimental effective strain starts to agree with FEM solution at the ratio, *r/a =5~6*, which indicates that the ratio of *c/a* is around *5~6* that *c* is the plastic zone size. This result also could be confirmed from the analytical models. In Johnson's cavity expansion model, the *c/a* value has been suggested to be a constant at any load levels with a cylindrical indentation. If the fully plastic state is assumed, by substituting $\nu = 0.5$ and $E \tan \beta / Y = 100$ into Eq.1 and Eq. 2, which is the limitation for 2D indentation to change the mode of deformation [5], it gives the relations that

$$c / a \approx 6 \tag{5}$$

$$\overline{p} \approx 2.7Y \tag{6}$$

Alternately , the normalized line load is linearly proportional to the plastic zone size as shown in Eq.3, and the *c/a* value based on the force equilibrium relation also could be estimated by substituting Eq. 6 into Eq.3 that

$$c / a \approx 4.7 \tag{7}$$

Therefore, compared with experimental measurement and analytical models, the plastic zone size of our experimental prediction agrees well with the analytical solution, which also has been experimentally examined for 3D micro conical indentation test [23].

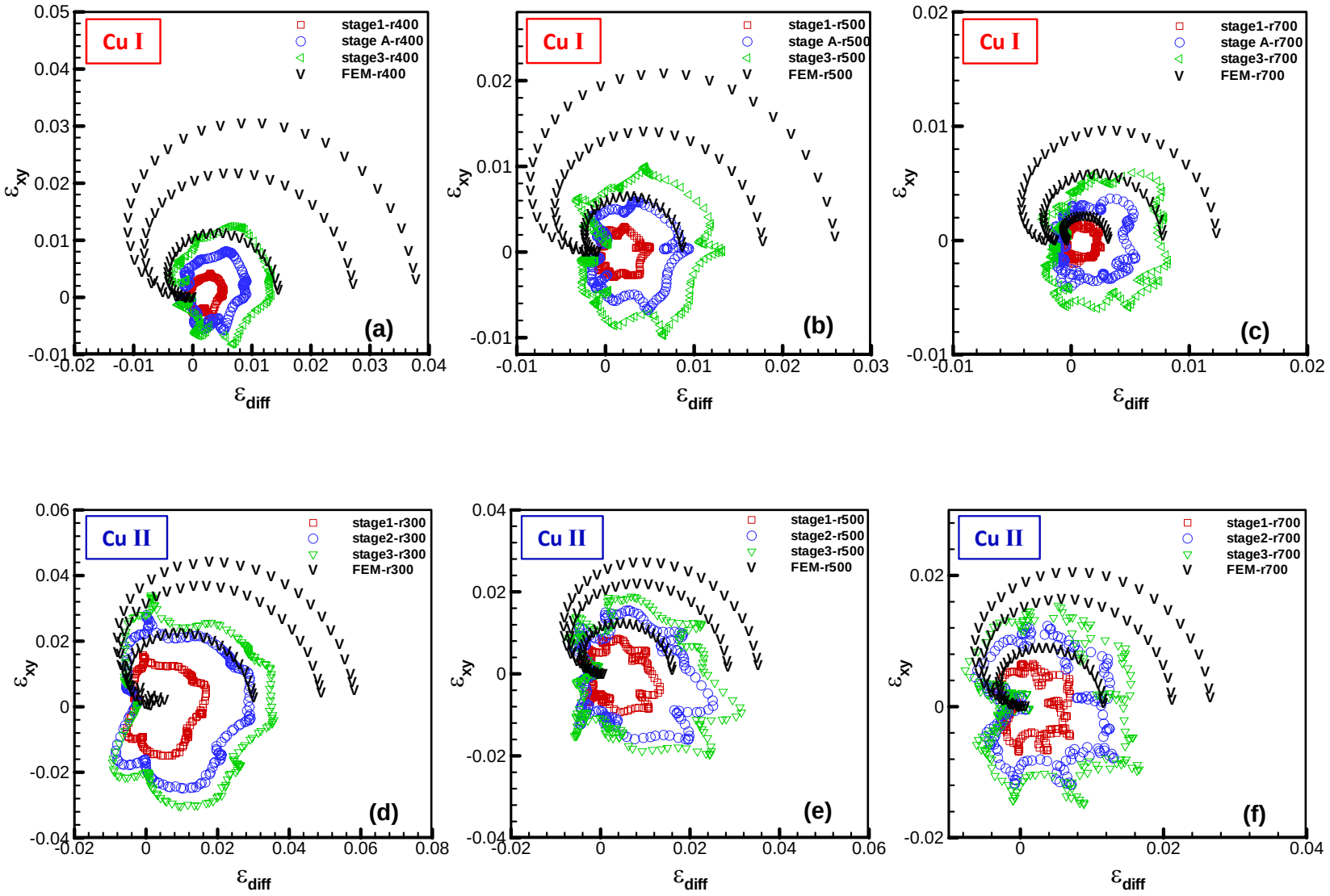
Cu I
stage1-r400
stage A-r400
stage3-r400
FEM-r400
(a)
Cu I
stage1-r500
stage A-r500
stage3-r500
FEM-r500
(b)
Cu I
stage1-r700
stage A-r700
stage3-r700
FEM-r700
(c)
Cu II
stage1-r300
stage2-r300
stage3-r300
FEM-r300
(d)
Cu II
stage1-r500
stage2-r500
stage3-r500
FEM-r500
(e)
Cu II
stage1-r700
stage2-r700
stage3-r700
FEM-r700
(f)
ε_{xy}
ε_{diff}

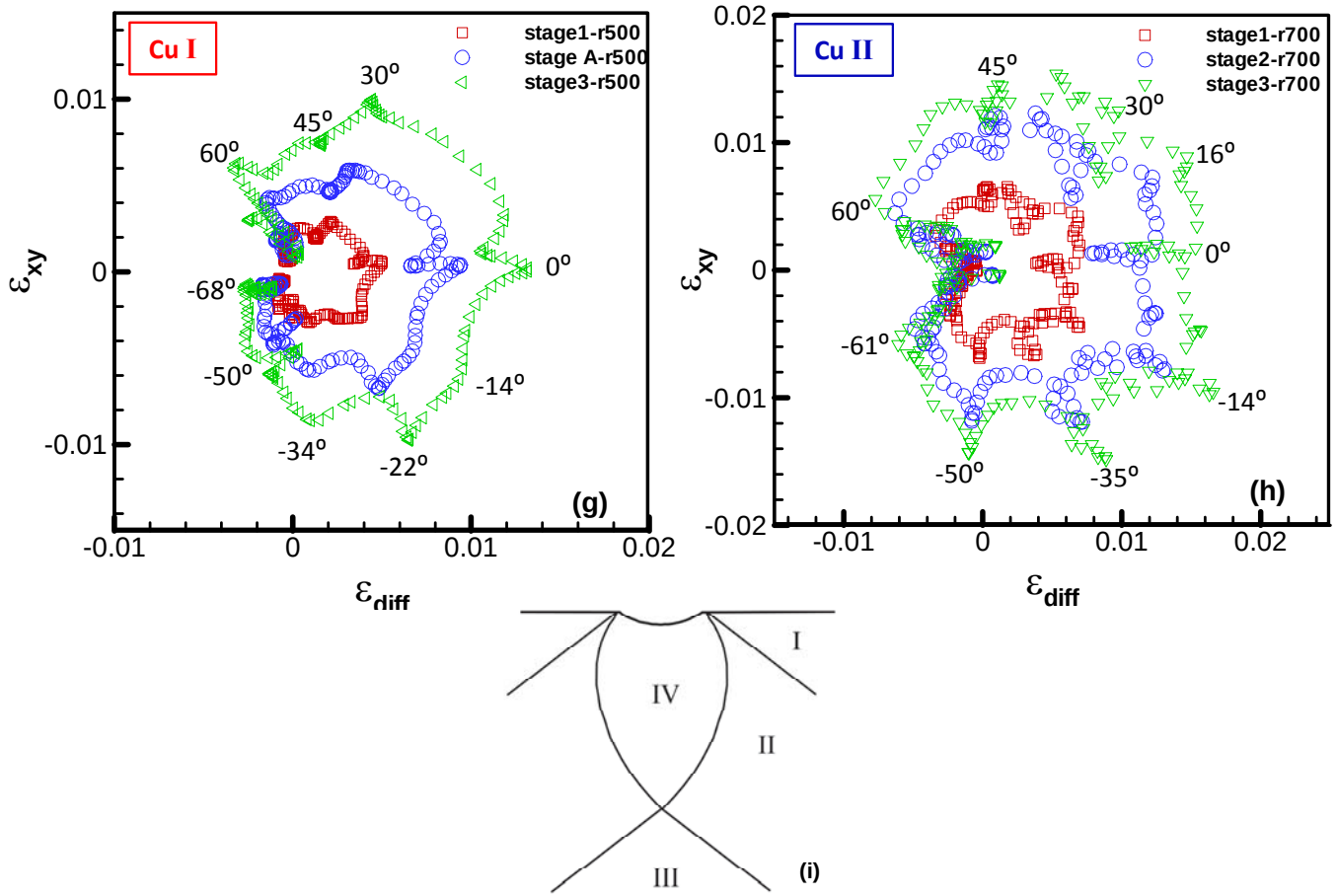

Figure 3.7 In-plane total strain vectors are plotted on reduced Mohr-plane as a function of the angular position at different loading stages. The trajectories of the strain vectors for Cu I and II are shown in (a)-(d), and (g) and (h) are about the details about the regular clusters along the trajectories with angular position marked. A slip-line field solution underneath the cylindrical indenter is plotted in (i).

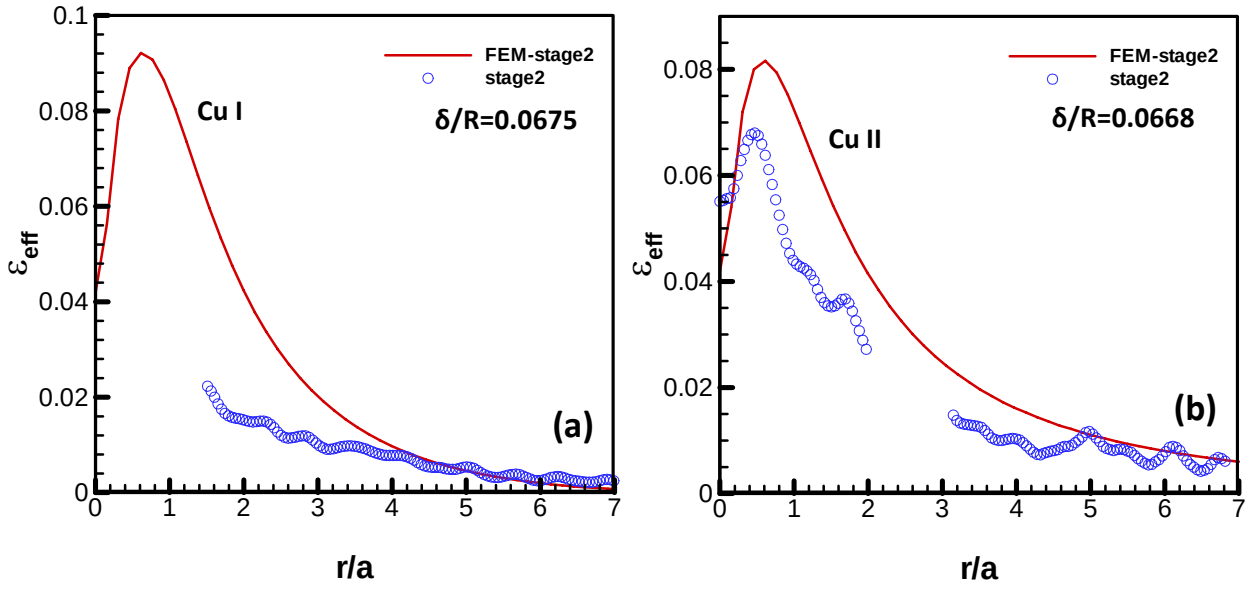

Figure 3.8 Comparison of the effective strain variation along the normalized radial distance for Cu I and Cu II with experimental measurements and FEM simulation results, where *a* is the contact radius.

As shown in Fig.3.6, we obtained the power fit expression to uniquely describe the effective strain distribution as a function of the normalized radial distance. Compared with the power exponents of the FEM simulation results and the analytical solution, our experimental estimation shows the lowest accumulated effective strain within the plastic zone, which means that there is an extra strain hardening mechanism also effect the strain distribution. The overlaps and clusters along the trajectory of the in-plane total strain vectors on the reduced Mohr-plane have already shown the non-homogenous yield surface of the plastic deformation. In the indentation test, for the polycrystalline metals or multi-phases alloys, the grains on the flank of the indent undergo large rotation because of the plastic deformation underneath indenter, which has been studied by electron backscattering diffraction scans [15]. Because of the non-homogenous plastic deformation and the large rotation, the gradient of plastic deformation has been built up in the plastic zone which requires introducing geometrically-necessary dislocations that provide for compatible deformation [24]. Such constraint plastic deformation could be the reason that introduces extra hardening capability of the materials underneath the indenter.

The trajectories of in-plane total strain vectors on reduced Mohr-plane show the plastic flow characterization closed the indenter tip, and Fig.3.7 shows that there are some irregular clusters along the trajectories. However, for Cu I at radius of 500μm and Cu II at radius of 700μm, the overlaps and clusters of the strain vectors on the reduced Mohr-plane seems have some regularities that they are symmetric relative to the angular position $\theta=0^{o}$ and the ε_{xy} components of a cluster of strain vectors around the position of $\theta=0^{o}$ are around zero. The characters of the slip-line field solution of a cylindrical indentation have been

discussed [8], which are very similar to the one of the blunt notch-tip field [25,26]. Fig.3.7i shows the different sectors of the slip-line field underneath the cylindrical indenter, in which sector IV is the logarithmic sector, sector I, III are simple stress sectors and sector II is a composite one that contains a transition from simple stress to logarithmic stress sector. For the incompressible material, the largest extent of the sector IV is located directly below the indenter tip at [27]

$$\boldsymbol{r} = \mathrm{Re}^{\boldsymbol{\beta}} \tag{10}$$

where r is the radial distance from the indenter tip, R is the radius of the indenter and β is same as defined in Eq. 2. Therefore, the extent of the sector IV depends on the indentation depth δ, that uniquely describe the angle β with a constant indenter radius R. Although our experimental materials are not perfect plastic material, the slip-line field solution still makes sense in the plastic zone closed to the indenter tip. Since the sector III is a simple stress sector without shear stress component $\boldsymbol{\varepsilon}_{xy}$, the circumferential line could pass through sector III if the radius is large enough, which means the all strain vectors in sector III should have zero $\boldsymbol{\varepsilon}_{xy}$ strain component same as what we observed in Fig.3.7g and Fig.3.7h. The rest of the symmetric clusters could be the strain vectors that near the boundary of different sectors that stress discontinuity exist in the slip-line field.

3.7 CONCLUSION

Experimental study of the plastic flow characterization with ductile metals has been developed under wedge-like cylindrical indentation. By digital image correlation technique,

the strain maps underneath the indenter have been plotted. The experimental observation of the shape of the plastic zone has confirmed as the one reported in the previous findings about Vickers indentation tests and a unique correlation of the strain distribution has been investigated along radial line with different angular positions. Self-similar manner has been observed in both of the radial dependence of the effective strain and the in-plane total strain vectors on reduced Mohr-plane at different loading stages. FEM numerical solution and analytical solution have been explored to evaluate the experimental measurements.

3.8 APPENDIX.1 CAVITY EXPANSION MODEL

The well-known theoretical solution of plastic-elastic expansion of a cylindrical tube was primarily based on the Tresca yield criterion and elastic-perfectly plastic model [12], which assumed that the plastic boundary in homogenous material was a spherical surface. For most of the ductile metals which yield von-Mises criterion, the approximation solution was obtained by replacing the yield strength Y in Tresca criterion with $2\boldsymbol{Y}/\sqrt{3}$, which was

$$\boldsymbol{\sigma_\theta} - \boldsymbol{\sigma_r} = 2\boldsymbol{Y}/\sqrt{3} \qquad \text{A.1}$$

Although the problem about open-end cylindrical tube, analogous to our experimental specimen, was more difficult than the closed one, this approximation solution still suits for the case of expansion of a cylindrical cavity in an infinite medium based on an empirically determined yield criterion (British design practice, dv.p.21).

By extending Hill's cavity expansion model, a simplified theoretical model was developed by [5], which was about the wedge indentation in an infinite elastic perfectly-

plastic body. In this model, a semi-cylindrical core of radius $\boldsymbol{a}$ replaced the cavity and a hydrostatic pressure $\bar{\boldsymbol{p}}$ was assumed inside of the core. Therefore, based on the stresses components given by Hill [12] (1950, p110) and Johnson's model, the approximation solution for von-Mises materials in infinite elastic perfectly-plastic medium can be written in the following:

$$\begin{cases} \dfrac{\sigma_r}{Y} = \dfrac{2}{\sqrt{3}}\left[-\dfrac{1}{2} - \ln\left(\dfrac{c}{r}\right)\right] \\ \dfrac{\sigma_\theta}{Y} = \dfrac{2}{\sqrt{3}}\left[\dfrac{1}{2} - \ln\left(\dfrac{c}{r}\right)\right] \end{cases} \qquad a \le r \le c \qquad \text{A.2}$$

$$\begin{cases} \dfrac{\sigma_r}{Y} = -\dfrac{1}{\sqrt{3}}\dfrac{c^2}{r^2} \\ \dfrac{\sigma_\theta}{Y} = \dfrac{1}{\sqrt{3}}\dfrac{c^2}{r^2} \end{cases} \qquad c \le r \qquad \text{A.3}$$

where $\boldsymbol{a}$ is the radius of the core, $\boldsymbol{c}$ is the plastic-elastic boundary, and $\boldsymbol{Y}$ is the yield strength under uniaxial loading. Subsequently, based on the radial displacements found by Hill (1950, p.126) [12] and the condition of conservation of volume in the core, Johnson's model considered both of the material parameters and the geometry of the indenter and obtained:

$$\frac{2\sqrt{3}E}{\pi Y}\tan\beta = (5-4\nu)(c/a)^2 - 3(1-2\nu) \qquad \text{A.4}$$

For an incompressible material $\nu = 0.5$, they yield the expression:

$$\frac{\bar{p}}{Y} = \frac{1}{\sqrt{3}}\left[1 + \ln\left(\frac{2E\tan\beta}{\sqrt{3}\pi Y}\right)\right] \qquad \text{A.5}$$

and $$\bar{p} = \frac{F}{2at} \qquad \text{A.6}$$

where E is the Young's modulus, $\bar{p}$ is the mean pressure in the core , β is the angle between the indenter flank and the surface and ν is the Poisson's ratio.

3.9 APPENDIX.2 SIMPLIFIED ANALYTICAL SOLUTION

A simple interpretation of Johnson's spherical cavity model was developed [12], which demonstrated the relation of the plastic zone size and the load level and was verified by both micro and nano indentation tests [7,23]. According to this model, we also developed a simplified version of Johnson's model for the cylindrical indentation. In Johnson's model where there was only hydrostatic pressure inside of the core region, it was assumed that only the radial stresses supported the load. Additionally, for the cylindrical indentation, σ_z was assumed to be the intermediate principle stress and there was no shear stress along the z direction on the yield surface, which is semi-cylindrical. Therefore, the stress components shown in Eq.A.2 satisfy the yield criterion described in Eq. A.1 inside of the elastic-plastic region and boundary condition yields

$$\sigma_r(c^-) = \sigma_r(c^+) = -\frac{1}{\sqrt{3}}Y\,. \qquad \text{A.7}$$

The area of the semi-cylindrical cap is $2\int_0^{\pi/2} \boldsymbol{t}\cdot\boldsymbol{c}\cdot\boldsymbol{d\theta}$, where t is the thickness of the specimen. Given this, the equilibrium relation between the radial forces, $\boldsymbol{\sigma_r}(\cos\boldsymbol{\theta})$ acting on the cylindrical surface and applied load level can be established and the force balance is

$$\boldsymbol{F} = 2\int_0^{\pi/2} \boldsymbol{\sigma_r}\cdot\cos\boldsymbol{\theta}\cdot\boldsymbol{t}\cdot\boldsymbol{c}\cdot\boldsymbol{d\theta} = 2\cdot\boldsymbol{c}\cdot\boldsymbol{t}\cdot\boldsymbol{\sigma_r} \qquad \text{A.8}$$

where F is the load level , c is the elastic-plastic boundary and t is the thickness of the specimen. By substituting the boundary condition Eq. A.7 into Eq. A.8,

$$\boldsymbol{F} = 2\cdot\boldsymbol{c}\cdot\boldsymbol{t}\cdot\boldsymbol{\sigma_r} = \frac{2\boldsymbol{cYt}}{\sqrt{3}} \qquad \text{A.9}$$

which indicates the linear relation between the applied force and plastic zone size of the cylindrical indentation.

3.10 REFERENCE

[1] D.S. Dugdale, "Experiments with pyramidal indenters--Part I," *Journal of the Mechanics and Physics of Solids*, vol. 3, Apr. 1955, pp. 197-205.

[2] D. Tabor, "Hardness and strength of metals," *Institute of Metals*, vol. 79, 1951, pp. 1-18.

[3] M. Doerner and W. Nix, "A method for interpreting the data from depth-sensing indentation instruments," *Journal of Materials Research*, vol. 1, 1986, p. 601.

[4] W. Oliver and G. Pharr, "Improved technique for determining hardness and elastic modulus using load and displacement sensing indentation experiments," *Journal of Materials Research*, vol. 7, 1992, pp. 1564-1580.

[5] K.L. Johnson, “Correlation of indentation experiments,” *J MECHANICS PHYSICS SOLIDS*, vol. 18, 1970, pp. 115–126.

[6] I. Sneddon, “Relation between load and penetration in axisymmetric Boussinesq problem for punch of arbitrary profile,” *International Journal of Engineering Science*, vol. 3, 1965, pp. 47-57.

[7] D. Kramer, H. Huang, M. Kriese, J. Robach, J. Nelson, A. Wright, D. Bahr, and W. Gerberich, “Yield strength predictions from the plastic zone around nanocontacts,” *Acta Materialia*, vol. 47, 1998, pp. 333-343.

[8] A. Bhattacharya and W. Nix, “Finite element analysis of cone indentation,” *International Journal of Solids and Structures*, vol. 27, 1991, pp. 1047-1058.

[9] Y. Wei and J.W. Hutchinson, “Hardness trends in micron scale indentation,” *Journal of the Mechanics and Physics of Solids,v51,n11-12* ,2003, pp. 2037-2056.

[10] L. Samuels and T. Mulhearn, “An experimental investigation of the deformed zone associated with indentation hardness impressions,” *Journal of the Mechanics and Physics of Solids*, vol. 5, Mar. 1957, pp. 125-134.

[11] T. Mulhearn, “The deformation of metals by vickers-type pyramidal indenters,” *Journal of the Mechanics and Physics of Solids*, vol. 7, Mar. 1959, pp. 85-88.

[12] R. Hill, *The Mathematical Theory of Plasticity. 1950*, Clarendon Press, Oxford, .

[13] M. Chaudhri, “Subsurface strain distribution around Vickers hardness indentations in annealed polycrystalline copper,” *Acta Materialia*, vol. 46, 1998, pp. 3047-3056.

[14] G. Srikant, N. Chollacoop, and U. Ramamurty, “Plastic strain distribution underneath a Vickers Indenter: Role of yield strength and work hardening exponent,” *Acta Materialia*, vol. 54, 2006, pp. 5171-5178.

[15] D. Kiener, R. Pippan, C. Motz, and H. Kreuzer, "Microstructural evolution of the deformed volume beneath microindents in tungsten and copper," *Acta Materialia*, vol. 54, 2006, pp. 2801-2811.

[16] A. Antoniou, A. Bastawros, and B. Biner, "Experimental observations of deformation behavior of bulk metallic glasses during wedge-like cylindrical indentation," *Journal of Materials Research*, vol. 22, 2007, pp. 514-524.

[17] A. Antoniou, A. Bastawros, C. Lo, and S. Biner, "Deformation behavior of a zirconium based metallic glass during cylindrical indentation: In situ observations," *Materials Science and Engineering A*, vol. 394, 2005, pp. 96-102.

[18] H. Bruck, S. McNeill, M. Sutton, and W. Peters III, "Digital image correlation using Newton-Raphson method of partial differential correction," *Experimental Mechanics*, vol. 29, 1989, pp. 261-267.

[19] Y. Wang and A.M. Cuitino, "Full-field measurements of heterogeneous deformation patterns on polymeric foams using digital image correlation," *International Journal of Solids and Structures*, vol. 39, 2002, pp. 3777-3796.

[20] X. Gao, "An exact elasto-plastic solution for an open-ended thick-walled cylinder of a strain-hardening material," *International Journal of Pressure Vessels and Piping*, vol. 52, 1992, pp. 129-144.

[21] M. Mata, M. Anglada, and J. Alcala, "Contact deformation regimes around sharp indentations and the concept of the characteristic strain," *Journal of Materials Research*, vol. 17, 2002, pp. 964-976.

[22] A. Bastawros and K. Kim, "Experimental analysis of near-crack-tip plastic flow and deformation characteristics (I): Polycrystalline aluminum," *Journal of the Mechanics and Physics of Solids*, vol. 48, Jan. 2000, pp. 67-98.

[23] D. Bahr and W. Gerberich, "Plastic zone and pileup around large indentations," *Metallurgical and Materials Transactions A: Physical Metallurgy and Materials Science*, vol. 27 A, 1996, pp. 3793-3800.

[24] ASHBY MF, "DEFORMATION OF PLASTICALLY NON-HOMOGENEOUS MATERIALS," *Phil Mag*, vol. 21, 1970, pp. 399-424.

[25] A. Al-Abduljabbar and J. Pan, "Effects of pressure sensitivity and notch geometry on notch-tip fields," *Polymer Engineering and Science*, vol. 38, 1998, pp. 1031-1038.

[26] H. Jeong, X. Li, A. Yee, and J. Pan, "Slip lines in front of a round notch tip in a pressure-sensitive material," *Mechanics of Materials*, vol. 19, 1994, pp. 29-38.

[27] L.M. Kachanov, *Fundamentals of the Theory of Plasticity*, Dover Publications, 2004.

CHAPTER 4: EXPERIMENTAL ANALYSIS OF INHOMOGENEOUS DEFORMATION IN BULK METALLIC GLASS DURING WEDGE-LIKE CYLINDRICAL INDENTATION

4.1 ABSTRACT

Inhomogeneous deformation behavior of Vitreloy-1 bulk metallic glass has been experimentally studied by wedge-like cylindrical indentation. The process zone underneath the indenter is in situ monitored to observe the nucleation and propagation of shear bands on the front surface. The deformation field is analyzed by digital image correlation technique and the severity of deformation is represented as strain maps at each loading increment by the in-plane maximum shear strain $\gamma_{\max}$. And the strain levels of the shear bands in strain maps can be used for visualization purpose only, due to the disparity in gage length for strain calculation within the shear bands (o(10~20nm)) and that utilized for the continuum strain map (o(10μm)). By measuring displacement jumps of two selected points on the shear bands, Lagrangian strain components of the shear band are estimated over the entire shear band thickness at different stages of the whole loading cycle. The corresponding Lagrangian strain components within the shear band surrounding are evaluated by bi-linear surface fitting local displacement distribution. The strain evolution shows that shear band deformation is highly discontinuous and the surrounding matrix does not show much activity during the activation of the shear band, and vice versa. The strain increment remarkably remains approximately in the same direction of the total macroscopic strain vector at every loading stage. The self-similarity of the deformation field surrounding matrix is indicated by strain increasing

without unloading. The measured strain level of a fresh shear band during first activation is comparable to the one evaluated from the theoretical model based on continuum mechanics.

4.2 INTRODUCTION

Bulk metallic glasses (BMG) exhibit unique combination of high strength, large elastic strain limit (up to 2%), [1,2] high hardness [3], corrosion resistance and formability [4]. Though, BMG fracture catastrophically by highly localized shear band in unconfined geometries, such as uniaxial tension or compression [1,2,5]. For the BMG deformation behavior, an empirical deformation map has been developed [6], classifying BMG flow as homogenous and inhomogeneous. The homogenous flow occurs at low stresses and high temperature [7]. Inhomogeneous flow is seen at high stress and low temperatures, where the plastic deformation tends to be highly localized into narrow shear bands. The macroscopic observations showed asymmetric deformation behavior between tensile and compressive loading [1] with moderate pressure dependent macroscopic yielding behavior [8-11]. Under geometric confinement, the BMG deformation exhibit increased ductility, accompanied with stable shear bands propagation. Especially under inhomogeneous loading conditions during ribbon bending [12], crack tip behavior [13] and indentation field, either in 2D [14,15] or 3D [3,9,16].

The microscopic mechanisms of the BMG inhomogeneous deformation is phenomenological viewed as a cooperative behavior of small clusters of randomly closed-packed atoms, so called shear transformation zones (STZs) [17], rather than the dislocation mechanisms in crystalline metals. The STZs are thought to create a localization of

displacements in surrounding regions that triggers the evolution of highly localized shear bands during the deformation by creation of free volume [17]. Such phenomenological view has been further corroborated by molecular dynamic (MD) simulations [18]. In continuum modeling, the free volume is considered to evolve with the applied stress [6]. The BMG plastic flow will occur when the free volume created by the applied stress exceeds the annihilation/diffusion rates. This microscopic view is generalized by Steif et al. (1982), Huang et al. (2002), among many others, to describe the initiation and propagation of shear bands. Transmission Electron Microscopy (TEM) analysis of the shear bands have indeed shown that the amount of voids has increased within a shear band, relative to surroundings [19].

Realizing the differences in length scales between TEM observations, MD simulation and the continuum description of shear band nucleation and propagations, there is a lack in experimental observation of the microscopic deformation evolution for shear bands in BMG. In this work, we have analyzed the evolution of the shear band in BMG under constrained geometry. The wedge-like cylindrical indentation experiment, developed earlier to allow in situ observation of the nucleation and propagation of shear bands, is utilized. The deformation field underneath the indenter is analyzed by digital image correlations. Details of the material, experimental protocols and the measurements of the shear strain within the shear band by digital image correlation (DIC) are given in section 2. The details of the experimental results and the history of the deformation filed within the shear band and the surrounding matrix are given in section 3.

4.3 EXPERIMENTS

Material System

The examined BMG is Vitreloy-1 with composition Zr 41.2-Ti 13.8-Cu 12.5-Ni 10-Be 22.5 (Atomic Weight). Both the X-ray diffraction analysis and TEM studies indicated that the system was in the amorphous state [20]. The sample has a cross section of 3mm in width by 7mm in height (indentation direction) and total length of 25mm. The sample front surface is polished with standard metallographic techniques to 1μm finish prior to indentation experiments. A random speckle pattern of 1μm graphite particle is applied on the front surface to enables the DIC analysis and estimates of the shear strain within and outside the shear bands. The resulting speckle pattern is about 10μm, which will set the analysis window to be about three times the average speckle pattern.

Experimental Setup

A computer controlled Instron 8862 servoelectric loading frame is utilized for the cylindrical indentation test, with controlled crosshead displacement rate of 1μm/s. A SiC wedge like cylindrical indenter with root radius, R of 2.4mm is used in the experiment. The schematic of the fixture and the alignment of the indenter and sample, as well as systematic study of the self-similarity of the field for other indenter radii can be found in Antonia el al. [14]. The load-indentation depth curve is shown in Fig.4.1 with the analysis stages marked on the curve. On the front surface of the sample, the evolution of the deformation zone underneath the indenter is in situ recorded during the course of loading by a traveling microscope with 5x lens objective and a progressive-scan camera (SPOT Insight CCD array of 2048x2048). A combination of through the lens and external oblique un-polarized white

light was used to illuminate the specimen surface. Images are collected every 2 seconds during the indentation test. The field of view is 2x2mm with a pixel resolution of 1 pixel/μm. This field of view is estimated to cover the entire process zone underneath the indenter up to the maximum applied load, based on estimates of the [21] cavity expansion model. A composite optical image showing the extent of the process zone at the end of the indentation test is shown in Fig.4. 2.

Strain Analysis

Digital Image Correlation Analysis

An in house digital image correlation (DIC) program is used to analyze the deformation filed on the front surface underneath the indenter. Pairs of images of the current deformed configuration and the reference undeformed configuration are correlated together to find the nodal displacement over a uniform grid points of 5 pixel spacing. At each nodal point on the reference configuration, a correlation window of 31x31 pixels is correlated to the corresponding pair on the deformed configuration. The DIC analysis protocol has two steps, (i) a coarse search is used to approximately locate the nodal displacement to the nearest pixel [22,23]. The search locates the correlation coefficients maxima within a search area (twice the correlation window size) on the deformed configuration. (ii) A fine search, utilizing the local intensity distribution, fitted to a two-dimensional third-order B-spline function is applied to minimize the error in the nodal displacement vector and their gradients [22,23]. Despite the accuracy of the numerical algorithm, the perceived resolution is about 0.01 pixel (ref. Chapter2). It should be noted that the acquired nodal displacement field, while in themselves have a high accuracy, they posses strong fluctuation to render a

compatible displacement field. Thus, a 2D second order polynomial is fitted to a smoothing window of 9x9 nodes, so as to smooth the higher order fluctuations and provide estimates of the displacement gradient. The strain accuracy will be thus controlled by the size of the smoothing window, which would set the strain measurement gage length to about 40μm. For such limits, the accumulated error in the strain measurements is bounded to about 0.025%. The acquired displacement gradients are then used to evaluate the Lagrangian strain components of the in-plane strain tensor on the nodal grid of the reference configuration. A typical result of the analysis is shown in Fig.4.3 for the in-plane maximum shear strain, $\gamma_{\max}$ for the increment of loading, stage5-6

$$\gamma_{\max} = \sqrt{(\varepsilon_{xx} - \varepsilon_{zz})^2 + 4\varepsilon_{zx}^2} \qquad (1)$$

The components of the in-plane strains are derived at a spatial point for the whole loading cycle relative to the reference configuration, or for an incremental loading step during the course of loading. In this definition, $\gamma_{\max}$ for the increment of loading would represent a metric of the severity of deformation, without confusing it with the exact definition of $\Delta\gamma_{\max} = f(\varepsilon, \Delta\varepsilon)$ that depends on both the total strain, ε at a give loading stage as well as the increment of stain, $\Delta\varepsilon$. The strain map highlights the evolution of the shear bands underneath indenter. To this extent, such strain map can be used for visualization purpose only, due to the disparity in gage length for strain calculation within the shear bands (o(10~20nm)) and that utilized for the continuum strain map (o(10μm)). Thus, no quantitative strain levels from such maps can be utilized to calibrate the physical models of shear band nucleation and formations.

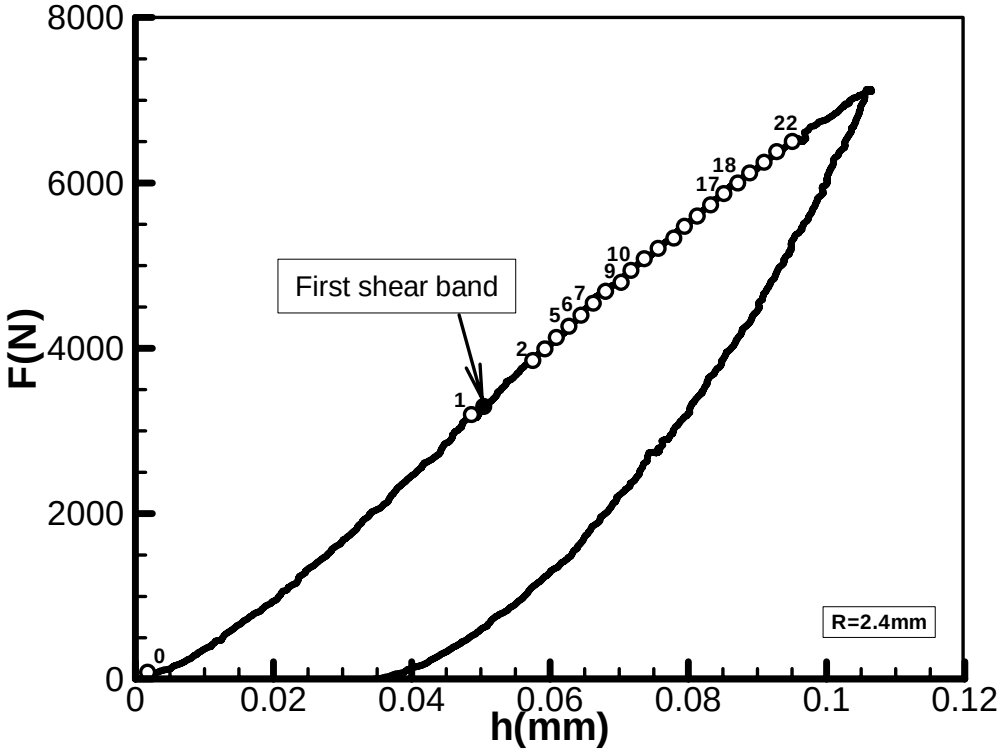

Figure 4.1 The load and indentation depth and analysis steps at different loading stages are marked on the curve.

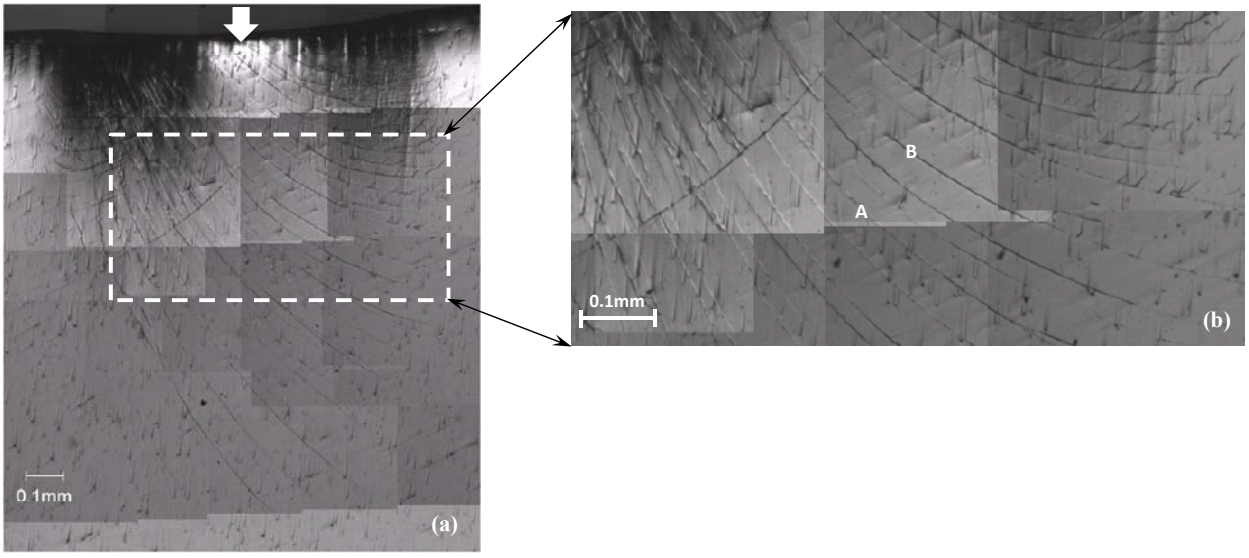

Figure 4.2 a composite optical image of the process zone after unloading and two points of interest along shear bands are shown in (b).

Estimates of Shear Strain within the Shear Bands

A typical shear band thickness in BMG is in the order of 10~20nm [24]. The disparity between the shear band thickness and the required gage length to evaluate the displacement gradient precludes the ability of the DIC to resolve the shear strain evolution within the band. The DIC technique overestimates the width of any deformation localization; with localization length scale that falls within the implemented gage length for each step of the analysis. For larger deformation localization, the effect of the analysis gage length can be corrected (Wang and Bastawros, 2010). When the scale of the localization is much smaller than the analysis gage length, the strain estimates are significantly reduced. Moreover, the spatial shear strain distribution within the band, as those shown in Fig.4.3, are nothing but artifacts that qualitatively highlights the shear bands.

Alternatively, if one accounts for the discontinuity in the displacement field across the shear band, an estimate of the displacement gradient can be found. Such estimate represents an average over the entire shear band thickness, without considering the spatial shear strain distribution within the band. Though, t has to be known, which can be done independently after the indentation experiment. For displacement gradient analysis, selected points on the shear band were chosen for the analysis at different stages of the whole loading cycle. The analysis starts by indentifying the variation of the in-plan displacement components in two orthonormal directions, centered at the point of interest along the shear band, for all loading increments. The results of two selected points A and B in Fig.4.2 (b) on two different shear bands within the network, underneath the indenter will be presented here to show the evolution of the shear strain within the band, and in the neighboring matrix.

Figure 4 (a-d) shows the variation of the two in-plan displacement components (u, w) at point B for the incremental loading stage 5-6, along two orthonormal directions ($H-H'$ and $V-V'$). The $V-V'$ direction is chosen to be parallel to the indentation direction for ease of analysis. The displacement jumps ΔU_x, ΔW_x, ΔU_z and ΔW_z are estimated across the shear band, and marked on the figure. Estimates of the average displacement gradients across the shear band will be,

$$\begin{bmatrix} \frac{\partial u}{\partial x} & \frac{\partial u}{\partial z} \\ \frac{\partial w}{\partial x} & \frac{\partial w}{\partial z} \end{bmatrix} = \begin{bmatrix} \frac{\Delta U_x}{t/\sin\theta} & \frac{\Delta U_z}{t/\cos\theta} \\ \frac{\Delta W_x}{t/\sin\theta} & \frac{\Delta W_z}{t/\cos\theta} \end{bmatrix} \qquad (2)$$

where, θ is the orientation angle of the shear band with the horizontal direction. Once the component of the displacement gradient are defined on an average sense within the shear band, the in plane components of the Lagrangian strain components can be evaluated. Outside the shear band, such as at point B', the local displacement distribution is fitted to a bi-linear surface, to evaluate the spatial displacement gradients and the corresponding Lagrangian strain components within the shear band surrounding.

To estimate the shear band width, we assume that the local plastic volumetric strain is conserved when the shear band initiates and the out of plane strain is neglected. The following expression shows the plastic volumetric strain of BMG:

$$\varepsilon_{mean-band} \cdot \frac{t}{\lambda + t} + \varepsilon_{mean-matrix} \cdot \frac{\lambda}{t + \lambda} = 0 \qquad (3)$$

Here, $\varepsilon_{mean} = (\varepsilon_{xx} + \varepsilon_{yy})/3$, t is the thickness of the shear band and λ is the spacing between bands. Also the mean strain values inside and outside of the shear band are chosen at the load stage that shear band initiated. By substituting λ, shear band thickness t is about 15nm calculated by Eq.3, which is comparable with the reported value [24].

4.4 EXPERIMENTAL RESULTS

Macroscopic Response

The acquired load-indentation depth curve of the BMG with indenter radius of 2.4mm is shown in Fig.4.1. The elastic stiffness of the loading fixture is removed from the loading curve. The first shear band is also marked on Fig.4. 1 at a macroscopic load of 3290N, just after the stage 1 of analysis. Employing the elastic Hertzian contact theory [25], the critical shear stress for the nucleation of the shear bands as 0.8 GPa [26]. An optical micrograph of the shear band morphology is shown in Fig.4. 2, showing self-similarity of the shear band pattern underneath the indenter. Analysis of the surface texture, shear band angle and spacing [26] showed that they closely follow the slip line field for a pressure sensitive material, with dominating surface textures that follow either the α or β lines for each sector. It was also observed that the band spacing is found to scale with the local average of the maximum in-plane shear strain such that the local strain energy is minimized.

Results of DIC analysis are shown in Fig.4.5 for the insert of Fig.4. 2(b), highlighting the evolution of the shear band network, as $\gamma_{\max}$ for the total loading till stage 6, and for the incremental loading between stage5-6. Careful examination of $\gamma_{\max}$ for the increment of loading stage 5-6 shows that the shear bands are not continuously evolving during the course

of the macroscopic applied load. Focusing on the three marked bands *A, B* and *C* on $\gamma_{\max}$ map for the total loading (Fig.4. 5a), only bands A and B can be seen on the $\gamma_{\max}$ map for the incremental increase in loading stage 5-6 (Fig.4. 5b). Here, we will focus on the strain evolution at these two points *A* and *B*, and within the perceived "*homogeneously*" deformed local surroundings, at points A' and B'.

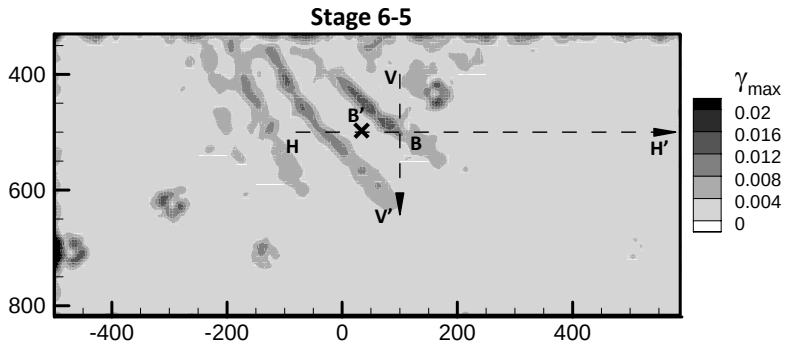

Figure 4.3 a typical result from digital image correlation (DIC) technique for the in-plan maximum shear strain at the loading increment stage5-6; To observe the displacement discontinuity, the displacement components are extracted along H-H' and V-V' lines.

History of shear band evolution

The incremental change of the strain components for each of the monitored loading stages on Fig.4. 1 is calculated using the algorithm elaborated in Sec. 3.2 for the spatial points, marked on Fig.4. 5b. For each group of incremental strain components, $\gamma_{\max}$ is evaluated employing Eq. (1). The average shear strain γ_{band} over the shear band width is summarized in Figs. 6 for the two spatial locations *A* and *B*. The evolution of γ_{band} and $\gamma_{\max}$ outside the band are plotted against a load derived shear strain measure, $\tilde{\gamma}_{\max}$ at the same

spatial point. The $\tilde{\gamma}_{\max}$ represents the homogeneous maximum in plane shear strain, derived from the Johnson's cavity expansion model (Johnson, 1970), as elaborated further in Appendix 1. The evolutions of γ_{band} and $\gamma_{\max}$ for each of the monitored loading increments are shown in Fig.4. 6a, b for both the shear band and its surrounding. Filled symbols represent activity within the shear band. It is apparent that there are close to three order of magnitude difference between the accumulated shear stain within the band and the surrounding matrix. During the activation of the shear band, the surrounding matrix does not show much activity, and vice versa, as indicated by the pairing of filled and unfilled symbols on the figure. By combining continuous loading increments with same shear band activation status, the variation of γ_{band} with $\tilde{\gamma}_{\max}$ for the shear bands *A*, *B* and their surroundings $\gamma_{\max}$ are shown in Fig.4. 6c, d. As shown, before shear band nucleation the accumulated matrix shear strain $\gamma_{\max}$ is around 3.35 ~ 4%, which is consistent with homogeneous strain estimations $\tilde{\gamma}_{\max}$ of 4-6% based on cavity expansion model. Once the shear bands initiated, they propagate discontinuously with a significant increment of plastic shear strain of about 3170~3550%.

The components of the total strain at each loading stage are evaluated at the spatial observation points based on the measured incremental strain components, such that

$$\varepsilon_{ij}(n+1) = \varepsilon_{ij}(n) + \Delta\varepsilon_{ij}. \qquad (3)$$

The total strain components are used to evaluate the measure of the deformation severity $\gamma_{\max}$. Fig.4. 7a, b shows the evolution of γ_{band} averaged over the shear band width, and $\gamma_{\max}$ over the surrounding matrix. The total accumulated shear strain within the band reaches 18000-19000%. The surrounding matrix around the shear band has total averaged shear strain about

6-7%. It is clearly seen that shear band deformation is highly discontinuous. The strain level of the surrounding matrix increases with different strain rate during loading, but not monotonic increasing with the possibility of relaxation as marked in Fig.4.7b at site A.

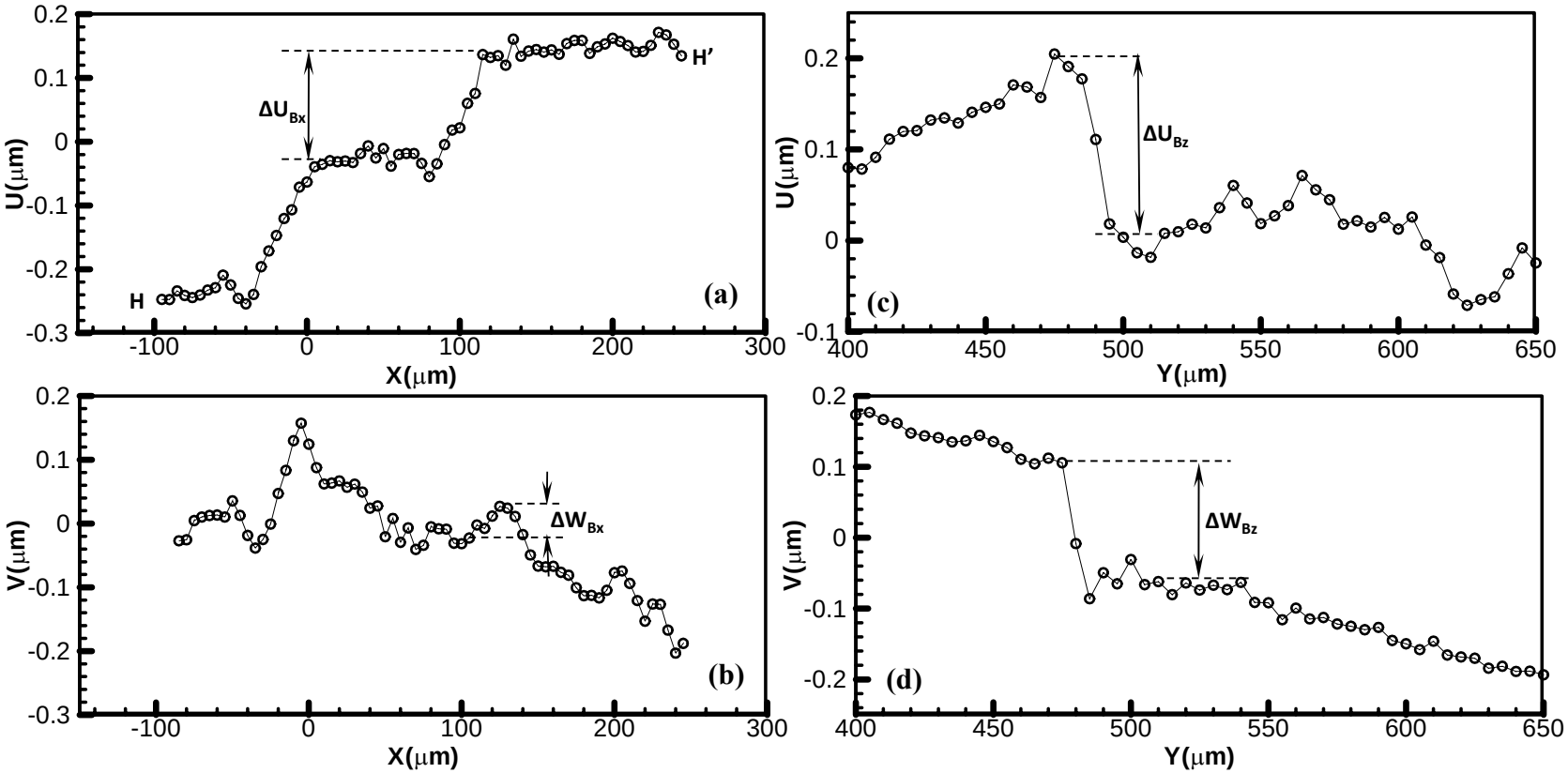

Figure 4.4 The variation of two in-plane displacement components at point B for the incremental loading stage 5-6, along two orthonormal directions (H-H' and V-V') shown in Fig.4.3.

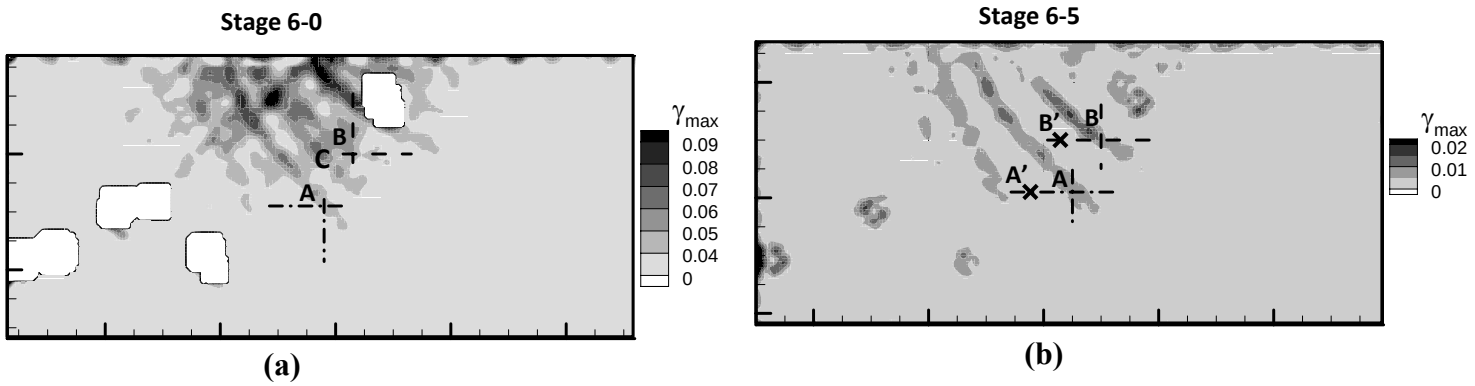

Figure 4.5 Results of DIC analysis for Fig.4.2 (b) that highlight the evolution of the shear band network, for the total loading till stage 6 and for the incremental loading between stage 5-6.

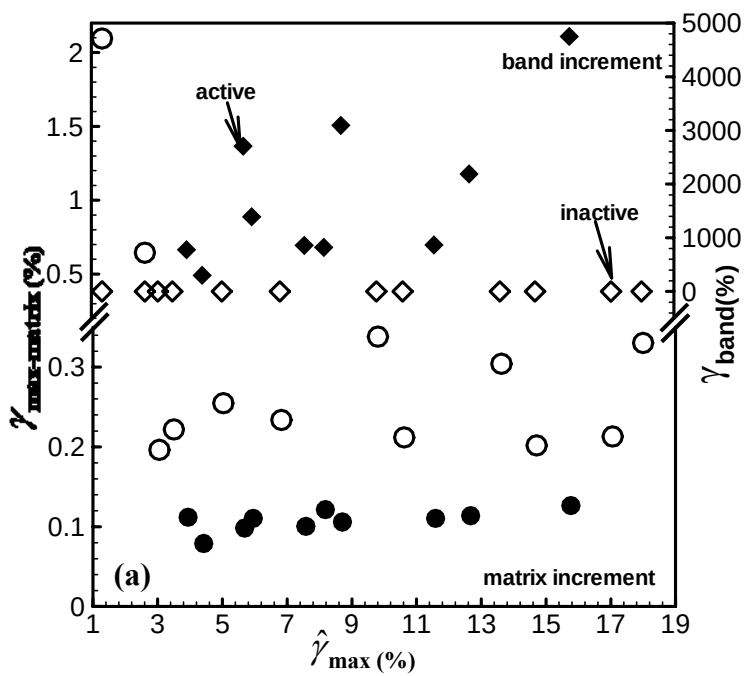
band increment
active
inactive
matrix increment
(a)
$\gamma_{max-matrix}$ (%)
γ_{band}(%)
$\hat{\gamma}_{max}$ (%)

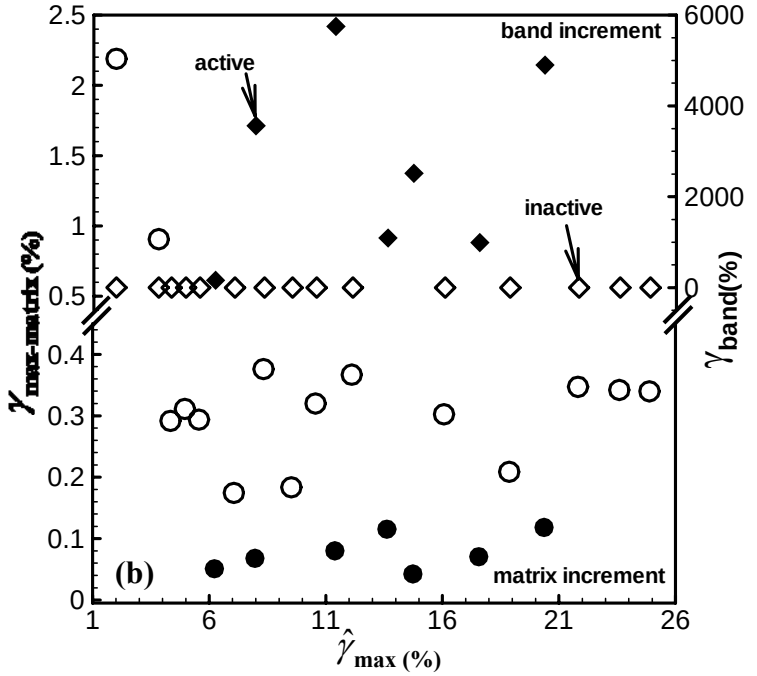
band increment
active
inactive
matrix increment
(b)
$\gamma_{max-matrix}$ (%)
γ_{band}(%)
$\hat{\gamma}_{max}$ (%)

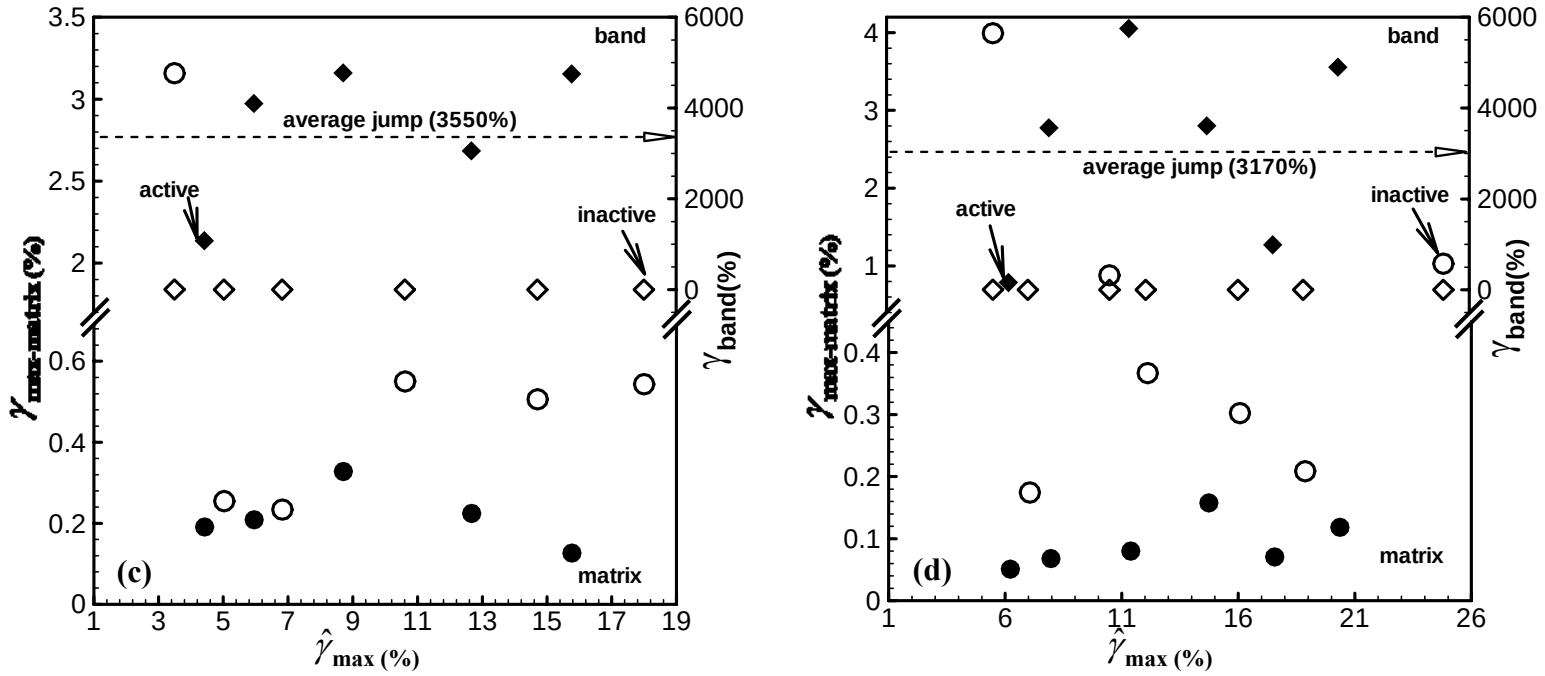

Figure 4.6 The evolution of in-plane maximum shear for each of the monitored loading increments: (a) and (b) for both shear band and their surroundings; the filled symbols show activity within the bands. (c) and (d) combine continuous loading increments with same shear band activity status for both shear band and their surroundings.

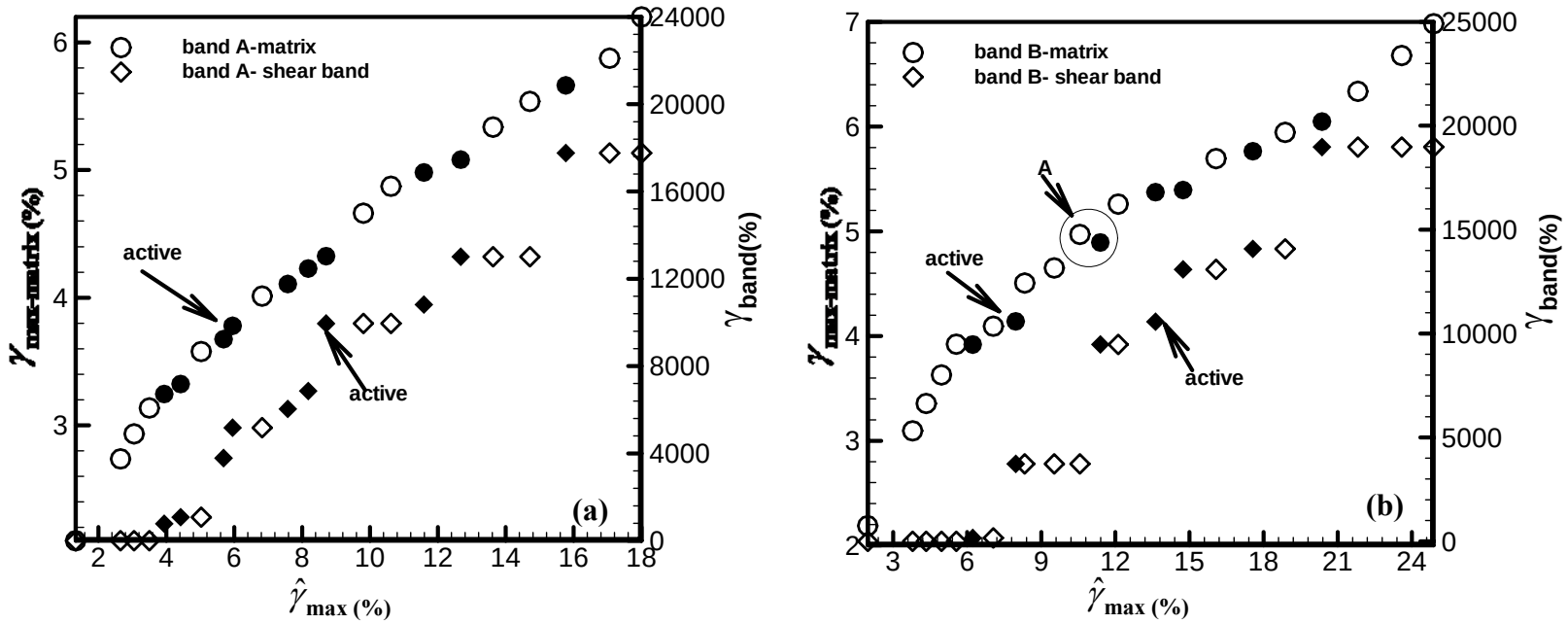

Figure 4.7 The evolution of total in-plane maximum shear strain averaged over the shear band width and the surrounding matrix

4.5 DISCUSSION

Shear band Nucleation

According to Huang's model (2002)[27], the inhomogeneous deformation occurs at the stress-driven creation of free volume becomes more significant and also the average strain has been accumulated at certain value. Following their example of simple shear problem and as for our experimental investigation of the shear band first initiation at spatial point (*A* or *B*), we validate the numerical model by utilizing experimental parameters. The total shear strain rate is

$$\frac{d\gamma}{dt} = \frac{1}{\mu}\frac{d\tau}{dt} + f(\xi, \tau_e)\frac{\tau}{\tau_e}, \qquad (4)$$

Where τ is shear stress; ξ is the free volume; τ_e is effective stress. The shear strain distribution across the shear band could be computed at the integration points. More results about the numerical model will be introduced in Appendix2. In Fig.4. 8, the maximum shear strain inside of the shear band has been plotted against average strain γ_{ave}, in which γ_{ave} indicates the time steps $\gamma_{ave} = rt$ and r is the averaged strain rate over the shear band. The numerical result shows that the localized deformation occurs at $\gamma_{ave} \approx 6.1\%$ with a shear strain jump about 150%. For our experimental observation, the measured in-plane maximum shear strains $\gamma_{\max}$ over the bands are also plotted against the homogeneous average shear strain $\tilde{\gamma}_{\max}$ in Fig.4. 8, when the shear bands initiate at the spatial points A, B. The magnitude of the accumulated maximum in-plain shear strain at point *B* is comparable with the one from simulation result. It also indicates that localization initiates at point *B* when the averaged

homogeneous strain reaches the level of 6.2%. About the other shear band *A*, it keeps active in two continuous incremental steps and the sum of these two continuous shear strain jumps is around 780%. The shear band nucleates as the average strain is about 4.0%. This is probably because the band *A* is an existing shear band before it passes spatial point *A*. Therefore, it doesn't need to accumulate so much energy to propagate the shear band as the one needed for a fresh shear band. Moreover, the intermittent deformation behavior of the shear band shows that the magnitude of the subsequent shear band nucleation after the initiation is higher than the first one as indicated in Fig.4. 6c, d. Comparable results also have been reported in the macro-response of the uniaxial compression test [28], in which the magnitude of the displacement serrations increases with plastic strain at later loading stages. This phenomenon has been demonstrated to be primarily caused by the intermittent abrupt sliding events which are the result of preferential shear band formation on an existing shear band in a BMG sample [29].

Nature of the deformation

The components of the total strain at the spatial observation points for each loading stages are evaluated by utilizing Eq. (3), based on the incremental strain components which are calculated along two orthogonal directions *x*,*z* shown in Fig.4. 3. The corresponding strain components for the shear bands and their surroundings are so called ε_{xx}, ε_{zz} and ε_{xz} plotted in Mohr's circles as shown in Fig.4.9 and Fig.4. 10. At the two spatial point A and B, shear bands have different inclined angle with the horizontal direction, 45° and 37°, respectively. Therefore, the strain states at each loading stage are also shown in Mohr's circles with respect to the rotated coordinates, along and normal to the shear band direction, *t*

and *n*. According to the definition in Antoniou et al (2007), band A and B belong to different shear band set. Band A is one of the primary formed shear band, which appears at the propagating front of the deformation; While band B is termed band with band that appear within previously formed bands. As can be seen in Fig.4. 9, it clearly indicates that band A primarily have simply shear deformation along shear band directions during the course of loading. The ε_{nn} strain components increase to stretching magnitude of 12000% and the level of shear strain ε_{nt} rises to 1000%, while the ε_{nt} components are very small relative to ε_{nn} component. About the surroundings, the strain Mohr's circles are shown in Fig.4. 10 at different loading stages. The two strain states show that the matrix outside of the shear band deforms in form of pure shear to accommodate the shear band deformation. However, the mean strain ε_{mean} of the surrounding matrix has a compressive status during the deformation with an averaged mean strain value of 0.29~0.30% during the whole deformation as shown in Fig.4. 11.

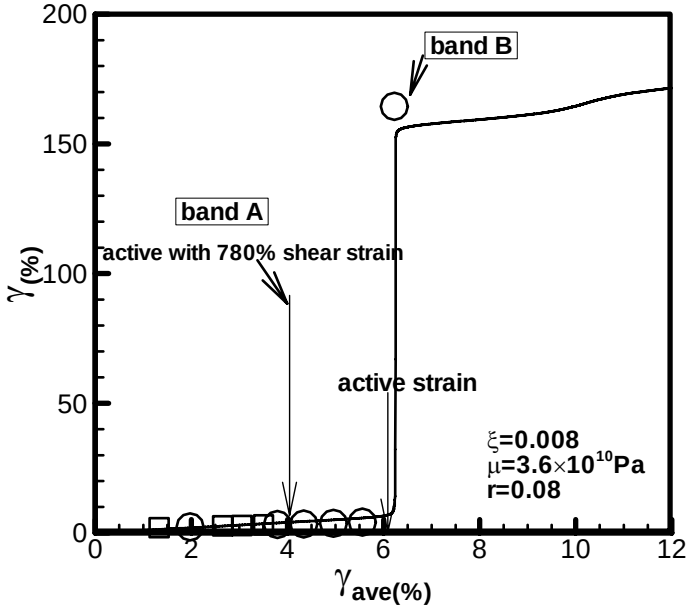

Figure 4.8 Analytical estimation and experimental measurements of the maximum shear strain inside of the shear band, in which experimental measurement for band B is more closed to the analytical result.

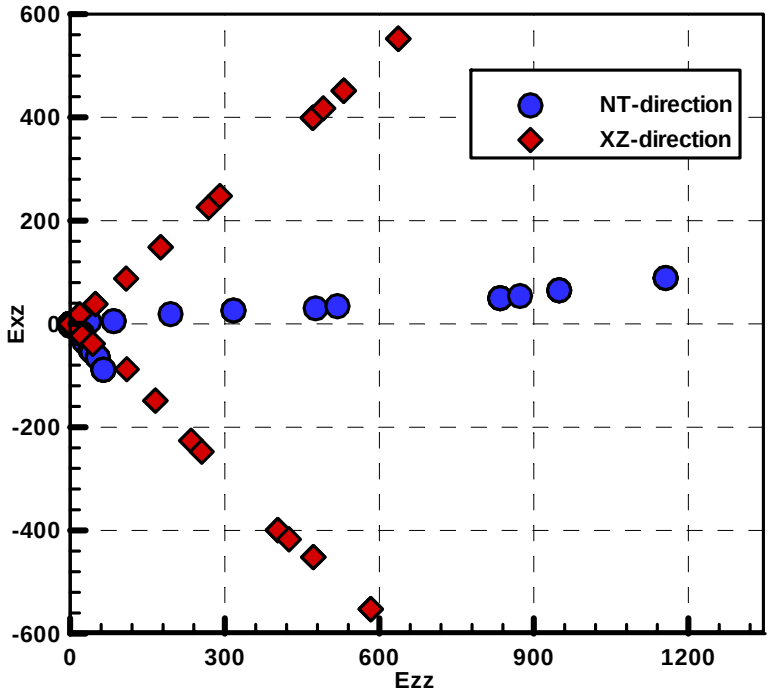

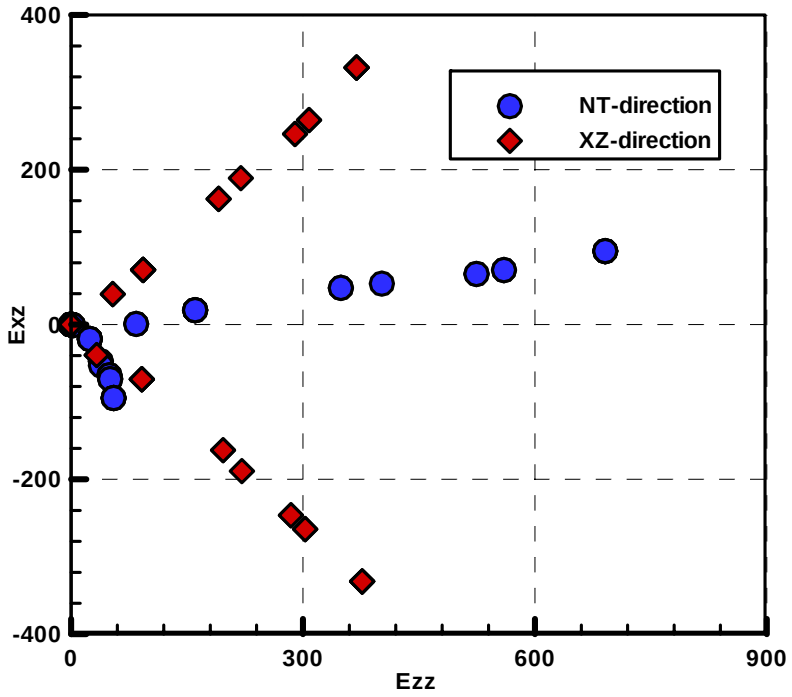

Figure 4.9 Strain component of shear band A and B are plotted in Mohr's circle. Different loading increments with active shear band are indicated by different colors. It shows that the nature of shear band deformation is simple shear.

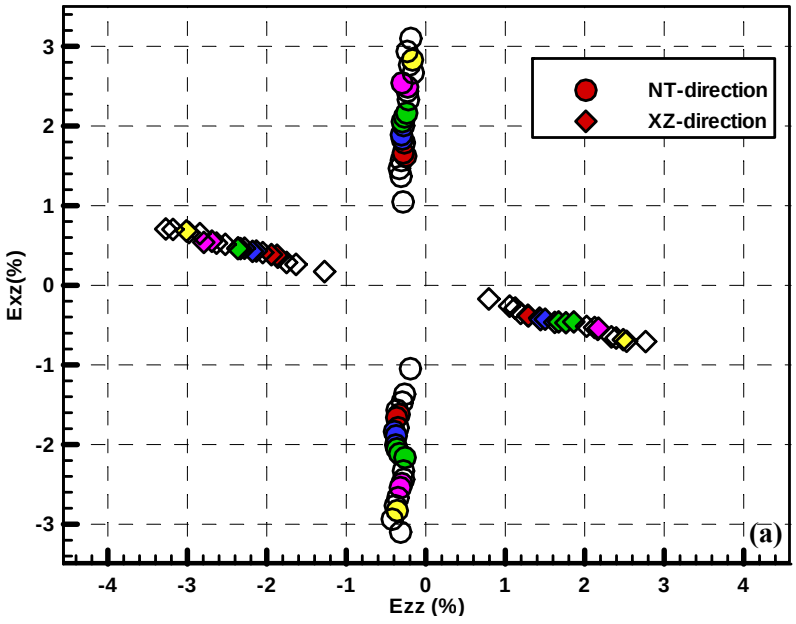

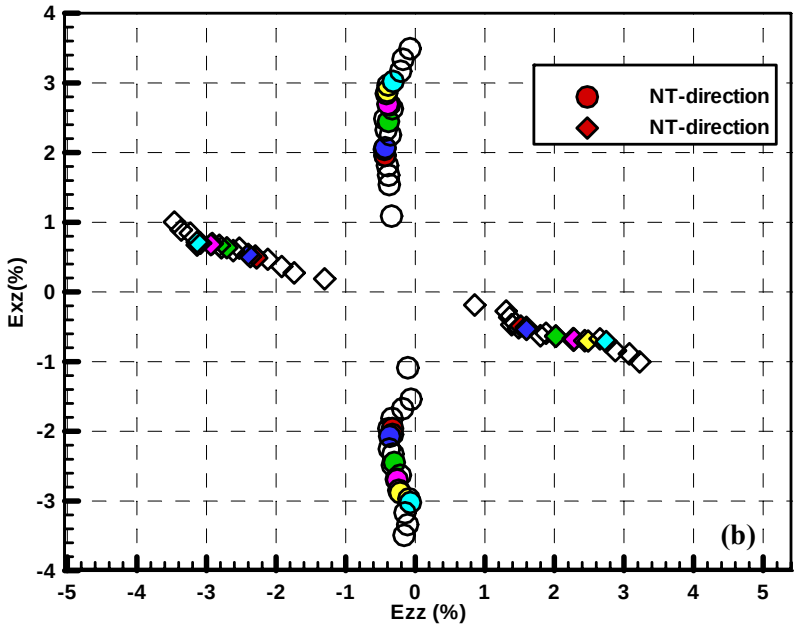

Figure 4.10 Strain component of the surrounding matrix are plotted in Mohr's circle. Different loading increments with active shear band are indicated by different colors. It shows that the surrounding matrix deforms in form of pure shear to accommodate the shear band deformation.

Characteristics of inhomogeneous plastic flow

The in-plane reduced Mohr strain plot will be used to understand the plastic flow characteristics of the inhomogeneous deformation. The component of the total in-plane strain $(\varepsilon_{xx} - \varepsilon_{zz})/2$ and ε_{zx} are shown in Fig.4. 12 for the surrounding matrix at the spatial points marked on Fig.4. 5b. Despite the highly inhomogeneous deformation field and intermittent deformation activity, the strain increment remarkably remains approximately in the same direction of the total macroscopic strain vector at every loading stage. By linear fit the strain components on the reduced Mohr's circle, the surrounding matrix has about 15^{o}~17^{o} offset from the horizontal direction. In addition, no evidence of the surrounding matrix unloading

can be seen. This is a clear indication of the self-similarity of the deformation field in the surrounding matrix.

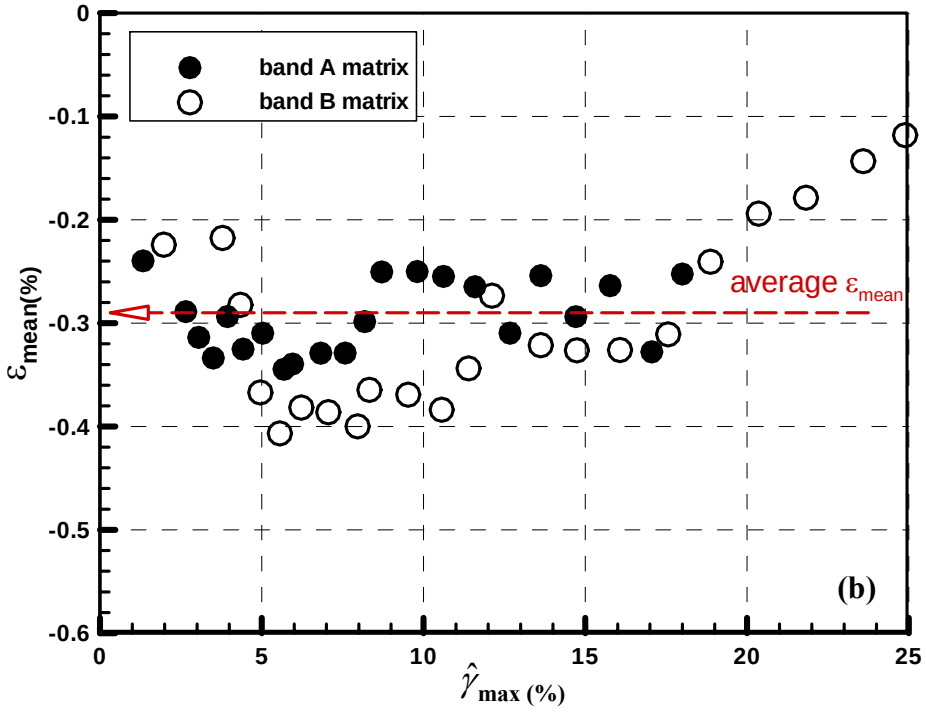

Figure 4.11 (a) the mean strain of the shear band increases with loading and show dilation property of shear band. (b) The mean strain of the surrounding matrix keeps almost constant during the loading, with average value of 0.3%.

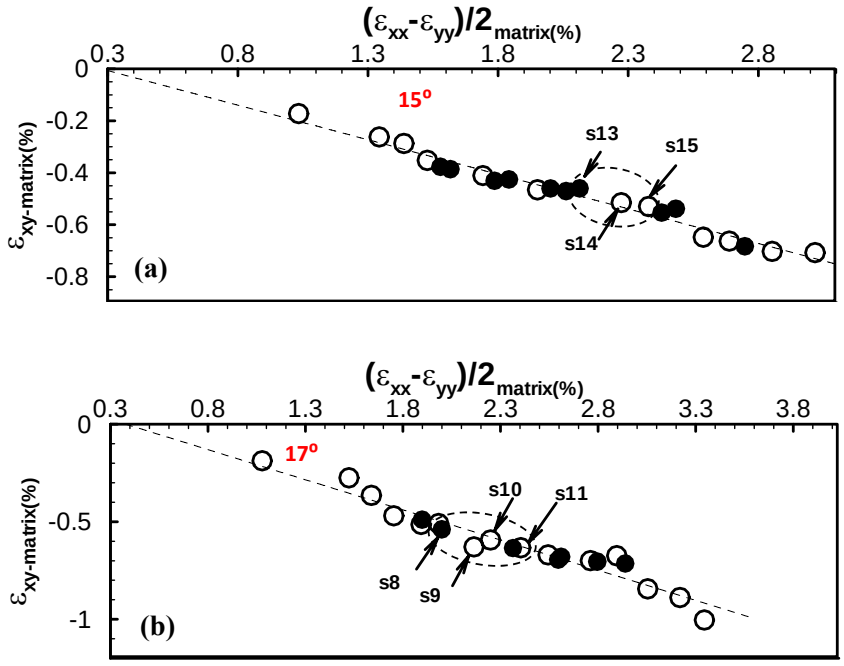

Figure 4.12 The in-plane strain components of surroundings are plotted in to reduced Mohr's circle (a) and (b). Since the incremental strain and the total strain keep almost same direction, it indicates self-similarity property of the shear band deformation.

4.6 CONCLUSION

Experimental study of the inhomogeneous deformation of metallic glass on microscopic level has been developed under wedge-like cylindrical indentation test by utilizing the digital image correlation technique. The evolution of shear band at fixed location has been investigated, including the nucleation strain level, strain increments inside of the shear band and the situation of the surroundings. It finds out that the shear band propagate highly discontinuously with different strain increment rate as their surrounding matrix. The shear band and the surroundings alternatively show their activity and the accumulated strain level inside of the shear band is higher than the one of the surroundings about 3 order

magnitudes. To explain the experimental observation about the shear band nucleation, a theoretical model has been used by initializing the experimental parameters and the simulation results are comparable with the experimental measurements, which characterizes the shear band initiation and post yield response on the microscopic level. Also, the nature of the shear band deformation is simple shear, while the surrounding matrix has pure shear deformation to accommodate the shear band propagation.

4.7 APPENDIX 1: CAVITY EXPANSION MODEL

The well-known theoretical solution of plastic-elastic expansion of a cylindrical tube was primarily based on the Tresca yield criterion and elastic-perfectly plastic model [30]. Then, based on Johnson's cavity expansion derivation [21], the following relation is obtained:

$$2(1-\nu)\left(\frac{c}{a}\right)^2-(1-2\nu)=\frac{2}{\pi}\frac{E}{(1+\nu)}\frac{1}{2k}\tan\beta \qquad \text{(A.1-1)}$$

Where E is the Young's modulus, ν is the Poisson's ratio, c is the plastic zone size, a is the contact radius, k is maximum in plane shear strength and β is the angle between the indenter flank and the surface. In this study, we estimate the plastic zone size c from the following:

$$\frac{c}{R}=2\pi\frac{(1-\nu^2)}{E/2k}\frac{\sqrt{e^{\bar{p}/k-1}}}{k}\left(e^{\bar{p}/k-1}-\frac{1-2\nu}{2(1-\nu)}\right) \qquad \text{(A.1-2)}$$

Here, $k = 0.5Y$ and $\overline{p}$ is the mean pressure within the cavity core. For an applied force F with the corresponding indentation depth h, $\overline{p} = F/(2W\sqrt{2Rh})$, where W is the indenter width.

From the radial displacements expression found by Hill (1950):

$$u = \frac{(1+\nu)(1-2\nu)}{E}\left(\frac{Y}{2}\right)\left[1+2\ln(\frac{c}{r})\right]r + \frac{(1+\nu)(1-\nu)}{E}Y\left(\frac{c}{r}\right)c$$

Under the small strain assumption, the strains in the elastic-plastic zone are:

$$\varepsilon_r = \frac{\partial u}{\partial r} = \frac{(1+\nu)(1-2\nu)}{E}\left(-\frac{Y}{2}\right)\left[2\ln(\frac{c}{r})-1\right] - \frac{(1+\nu)(1-\nu)}{E}Y\left(\frac{c}{r}\right)^2$$

$$\varepsilon_\theta \approx \frac{u}{r} = \frac{(1+\nu)(1-2\nu)}{E}\left(-\frac{Y}{2}\right)\left[2\ln(\frac{c}{r})+1\right] + \frac{(1+\nu)(1-\nu)}{E}Y\left(\frac{c}{r}\right)^2$$

The maximum in-plane shear strain in elastic-plastic zone could be deduced as:

$$\tilde{\gamma}_{\max} = \frac{(1+\nu)(1-2\nu)}{E}\left(-\frac{Y}{2}\right) + \frac{(1+\nu)(1-\nu)}{E}Y\left(\frac{c}{r}\right)^2 \qquad \text{(A.1-3)}$$

where $Y = 2k$,for elastic-plastic zone ($a \le r \le c$). More details about derivation could be found elsewhere (Antoniou thesis).

To estimate the nominal strain rate by cavity expansion model inside of the elastic-plastic zone, we need to do the time derivative of Eq. A.1-3 and A.1-1:

$$\dot{\varepsilon}_{eff} = \frac{(1-\nu)(1+\nu)}{E}Y\frac{c\dot{c}}{r} \qquad \text{(A.1-4)}$$

By plugging $\tan\beta = \frac{a}{R}$ and $a = \sqrt{2Rh}$ into the time derivative of Eq.A.1-1, the final result could be summarized as following:

$$cc' = \frac{R\dot{h}(1-2\nu)}{2(1-\nu)} + \frac{3E\sqrt{2Rh}\,\dot{h}}{4\pi(1-\nu^2)k} \qquad \text{(A.1-5)}$$

Here, h is the indentation depth and $\dot{h}$ is the loading rate in the experiment; R is the radius of the indenter.

Finally, the nominal strain rate could be expressed as:

$$\dot{\varepsilon}_{eff} = \frac{(1+\nu)k}{2Er}\left[2R\dot{h}(1-2\nu) + \frac{3E\sqrt{2Rh}\,\dot{h}}{\pi(1+\nu)k}\right] \qquad \text{(A.1-6)}$$

4.8 APPENDIX 2: NUMERICAL MODEL FOR INHOMOGENEOUS DEFORMATION IN METALLIC GLASS

In Huang ‘s model (2002)[27], it assumes that the average strain rate of the thin layer is a constant. Based on the reported model about the shear band [31], the average strain rate γ'_{ave} is equal to the volume weighted average of the strain rate inside and outside of the band, according to:

$$\rho\gamma'_b + (1-\rho)\gamma'_o = \gamma'_{ave} \qquad \text{(A.2-1)}$$

Where ρ is the volume fraction of the thin band (a typical value of 10^{-6} will be used), $\gamma_b^{'}$ is the strain rate inside of the band, which has the range of 5×10^3- 7×10^4 s^{-1} from the measurement of uniaxial compression test[28]; and $\gamma_o^{'}$ is the strain rate outside of the band, which we assume as homogeneous maximum in plane shear strain rate $d\tilde{\gamma}_{\max}/dt$ defined from Cavity Expansion Model (See Appendix1). r is the average strain rate, defined as

$$r = \frac{1}{2h}\int_{-h}^{h} \gamma_{ave}^{'} dx \qquad \text{(A.2-2)}$$

Here $2h$ is the width of the thin layer. Based on the sample used in this study, shear modulus μ of the BMG is $36GPa$ and the value of the normalized shear modulus $\bar{\mu}$ is 53, which is defined as:

$$\bar{\mu} = \frac{\mu\Omega}{2k_B T} \qquad \text{(A.2-3)}$$

Here, Ω is the atomic volume of the BMG which is $1.64\times10^{-29}m^3$; Initial free volume concentration and parameter R are defined same as Huang's model (2002).

Here, we just show the main equations that we used to do the simulation by plugging our experimental parameters.

The stresses and strains are assumed to be zero in the initial configuration. By finite element method and a semi-implicit algorithm for the time integration, the free volume is updated by solving the following equation:

$$\frac{\partial \xi}{\partial t} = D\frac{\partial^2 \xi}{\partial x^2} + g(\xi, \tau_e) \qquad \text{(A.2-4)}$$

Where $g(\xi, \tau_e) = R \cdot \exp\left[-\frac{\alpha}{\xi}\right]\left\{\frac{\alpha}{\beta\overline{\mu}\xi}\left(\cosh\frac{\tau_e \Omega}{2k_B T} - 1\right) - \frac{1}{n_D}\right\}$ from Spaepen's model (1977), in which $\beta = 1, \alpha = 0.15, n_d = 3$ and $R = \nu_0 \exp\left[-\frac{\Delta G^m}{k_B T}\right]$. Here, $\nu_0 \sim 10^{13} s^{-1}$, $\Delta G^m \sim 10^{-19} J$ and $k_B T \sim 5 \times 10^{-21} J$ with $T \sim 400K$.

The shear stress is computed from the following equation by the integration with respect to x with Gaussian quadrature method.

$$\frac{d\tau}{dt} = \mu\left[r - \frac{1}{2h}\int_{-h}^{h} f(\xi, \tau_e)\frac{\tau}{\tau_e}dx\right] \qquad \text{(A.2-5)}$$

where $f(\xi, \tau_e) = 2R \cdot \exp\left[-\frac{\alpha}{\xi}\right]\sinh\left[\frac{\tau_e \Omega}{2k_B T}\right]$, and τ_e is the effective stress, $\tau_e = \sqrt{\tau^2 + \frac{1}{3}\sigma^2}$. Therefore, at each time step, the shear stress and free volume concentration at next time step are computed from Eqs. A.2-4 and A.2-5, respectively, using the values of current time step. Then the normal strain could be calculated by:

$$\frac{d\varepsilon}{dt} = \frac{1}{2h}\int_{-h}^{h}\left[f(\xi, \tau_e)\frac{\sigma}{6\tau_e} + \frac{1}{3}\frac{\partial \xi}{\partial t}\right]dx \qquad \text{(A.2-6)}$$

After that, the normal stress σ could be computed at each integration point from the following equation,

$$\frac{d\varepsilon}{dt} = \frac{1-2\nu}{2\mu}\frac{\partial\sigma}{\partial t} + f(\xi,\tau_e)\frac{\sigma}{6\tau_e} + \frac{1}{3}\frac{\partial\xi}{\partial t} \ . \qquad \text{(A.2-7)}$$

At the last step, the shear strains γ at the integration points are computed from the equation as shown:

$$\frac{d\gamma}{dt} = \frac{1}{\mu}\frac{d\tau}{dt} + f(\xi,\tau_e)\frac{\tau}{\tau_e} \qquad \text{(A.2-8)}$$

Fig.4. 13(a) shows the maximum shear strains inside of the shear band have with different strain rates. Since the strain rate in our experiment is an approximated value, several normalized strain rates have been tried in the simulation and finally r/R=5.9×10^{-7} is chosen because of the best fitting experimental results. The variation of the shear stress normalized by shear modulus is shown in Fig.4.13 (b), in which the shear stress starts to drop at the $\gamma_{ave} \approx 6.1\%$ marked as active strain. Also, the variation of the simulated free volume amplitudes with the distance relative to the band center at different time steps is plotted in Fig.4.13 (c), which also demonstrates that the free volume disturbance starts to grow at same average strain level.

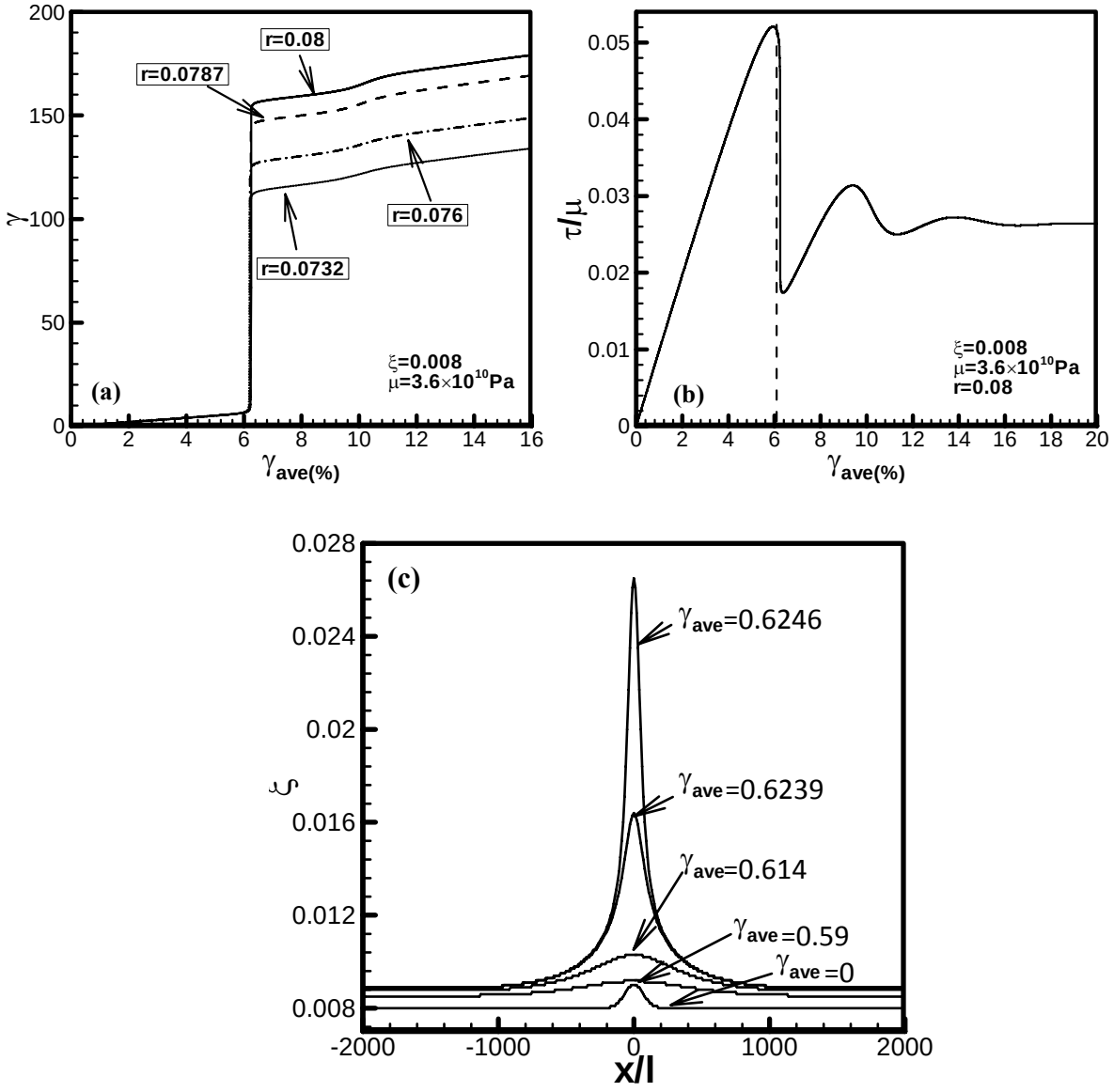

Figure 4.13 (a) maximum shear strains inside of shear band with different strain rates.(b) the variation of the shear stress normalized by shear modulus and the average strain and it shows shear band initiates at about 6% stain level. (c) The simulated free volume amplitude varies with distance relative to the band center, which also shows the instable growth at the 6% of average strain.

4.9 REFERENCE

[1] H. Bruck, T. Christman, A. Rosakis, and W. Johnson, "Quasi-static constitutive behavior of Zr41.25Ti13.75Ni10 Cu12.5Be22.5 bulk amorphous alloys," *Scripta metallurgica et materialia*, vol. 30, 1994, pp. 429-434.

[2] W.J. Wright, R.B. Schwarz, and W.D. Nix, "Localized heating during serrated plastic flow in bulk metallic glasses," *Materials Science and Engineering A*, vol. 319-321, 2001, pp. 229-232.

[3] P. Donovan, "Yield criterion for Pd40Ni40P20 metallic glass," *Acta Metallurgica*, vol. 37, 1989, pp. 445-456.

[4] Y. Kawamura, T. Nakamura, and A. Inoue, "Superplasticity in Pd40Ni40P20 metallic glass," *Scripta Materialia*, vol. 39, 1998, pp. 301-306.

[5] C.A. Pampillo, "FLOW AND FRACTURE IN AMORPHOUS ALLOYS.," *Journal of Materials Science*, vol. 10, 1975, pp. 1194-1227.

[6] F. Spaepen, "MICROSCOPIC MECHANISM FOR STEADY STATE INHOMOGENEOUS FLOW IN METALLIC GLASSES.," *Acta Metallurgica*, vol. 25, 1977, pp. 407-415.

[7] H. Chen and M. Goldstein, "ANOMALOUS VISCOELASTIC BEHAVIOR OF METALLIC GLASSES OF Pd-Si-BASED ALLOYS.," *Journal of Applied Physics*, vol. 43, 1972, pp. 1642-1648.

[8] A.C. Lund and C.A. Schuh, "Yield surface of a simulated metallic glass," *Acta Materialia*, vol. 51, 2003, pp. 5399-5411.

[9] M. Patnaik, R. Narasimhan, and U. Ramamurty, "Spherical indentation response of metallic glasses," *Acta Materialia*, vol. 52, 2004, pp. 3335-3345.

[10] A. Antoniou, A. Bastawros, and B. Biner, "Experimental observations of deformation behavior of bulk metallic glasses during wedge-like cylindrical indentation," *Journal of Materials Research*, vol. 22, 2007, pp. 514-524.

[11] U. Ramamurty, S. Jana, Y. Kawamura, and K. Chattopadhyay, "Hardness and plastic deformation in a bulk metallic glass," *Acta Materialia*, vol. 53, 2005, pp. 705-717.

[12] R. Conner, W. Johnson, N. Paton, and W. Nix, "Shear bands and cracking of metallic glass plates in bending," *Journal of Applied Physics*, vol. 94, 2003, pp. 904-911.

[13] C. Gilbert, R. Ritchie, and W. Johnson, "Fracture toughness and fatigue-crack propagation in a Zr-Ti-Ni-Cu-Be bulk metallic glass," *Applied Physics Letters*, vol. 71, 1997, p. 476.

[14] A. Antoniou, A. Bastawros, C. Lo, and S. Biner, "Deformation behavior of a zirconium based metallic glass during cylindrical indentation: In situ observations," *Materials Science and Engineering A*, vol. 394, 2005, pp. 96-102.

[15] A. Antoniou, P. Onck, and A.F. Bastawros, "Experimental analysis of compressive notch strengthening in closed-cell aluminum alloy foam," *Acta Materialia*, vol. 52, 2004, pp. 2377-2386.

[16] R. Vaidyanathan, M. Dao, G. Ravichandran, and S. Suresh, "Study of mechanical deformation in bulk metallic glass through instrumented indentation," *Acta Materialia*, vol. 49, 2001, pp. 3781-3789.

[17] A. Argon, "PLASTIC DEFORMATION IN METALLIC GLASSES.," *Acta Metallurgica*, vol. 27, 1979, pp. 47-58.

[18] Y. Shi and M.L. Falk, "Atomic-scale simulations of strain localization in a single-component three-dimensional model amorphous solid," *2005 MRS Fall Meeting, November 28, 2005 - December 2, 2005*, Boston, MA, United states: Materials Research Society, 2005, pp. 120-125.

[19] J. Li, F. Spaepen, and T. Hufnagel, "Nanometre-scale defects in shear bands in a metallic glass," *Philosophical Magazine A: Physics of Condensed Matter, Structure, Defects and Mechanical Properties*, vol. 82, 2002, pp. 2623-2630.

[20] M. Kramer, D. Sordelet, A. Bastarows, X. Tan, and S. Biner, "Absence of crystallization during cylindrical indentation of a Zr-based metallic glass," *Journal of Non-Crystalline Solids*, vol. 351, 2005, pp. 2159-2165.

[21] K.L. Johnson, "Correlation of indentation experiments," *J MECHANICS PHYSICS SOLIDS*, vol. 18, 1970, pp. 115–126.

[22] M. Sutton and Y. Chao, "novel experimental techniques in the fracture mechanics ," *ASME*, vol. 176, 1993, pp. 203-217.

[23] Y. Wang and A.M. Cuitino, "Full-field measurements of heterogeneous deformation patterns on polymeric foams using digital image correlation," *International Journal of Solids and Structures*, vol. 39, 2002, pp. 3777-3796.

[24] Y. Zhang and A. Greer, "Thickness of shear bands in metallic glasses," *Applied Physics Letters*, vol. 89, 2006.

[25] K.L. Johnson and L.M. Keer, "Contact Mechanics," *Journal of Tribology*, vol. 108, Oct. 1986, p. 659.

[26] A.M. Antoniou, *Experimental observations of shear band nucleation and propagation in a bulk metallic glass using wedge-like cylindrical indentation*, Thesis (Ph.D.)--Iowa State University, 2006.: 2006.

[27] R. Huang, Z. Suo, J. Prevost, and W. Nix, "Inhomogeneous deformation in metallic glasses," *Journal of the Mechanics and Physics of Solids*, vol. 50, 2002, pp. 1011-1027.

[28] S. Song and T. Nieh, "Flow serration and shear-band viscosity during inhomogeneous deformation of a Zr-based bulk metallic glass," *Intermetallics*, vol. 17, 2009, pp. 762-767.

[29] S. Song, H. Bei, J. Wadsworth, and T. Nieh, "Flow serration in a Zr-based bulk metallic glass in compression at low strain rates," *Intermetallics*, vol. 16, 2008, pp. 813-818.

[30] R. Hill, *The Mathematical Theory of Plasticity. 1950*, Clarendon Press, Oxford, .

[31] P. Steif, F. Spaepen, and J. Hutchinson, "STRAIN LOCALIZATION IN AMORPHOUS METALS.," *Acta Metallurgica*, vol. 30, 1982, pp. 447-455.

CHAPTER 5: DEFORMATION AND FRACTURE TESTING OF NI-BASED BULK METALLIC GLASS COMPOSITE BY WEDGE-LIKE INDENTATION

5.1 ABSTRACT:

The deformation and damage evolution behavior of a Ni-based bulk metallic glass (BMG) composite reinforced with elongation brass phase is studied under wedge like cylindrical indentation. The estimated fracture toughness values based on the energy dissipation and the in-situ observation during the loading reveal the details of the damage evolution and toughening mechanisms in this composite system. The results indicate that the enhanced toughness of the BMG composite is plausibly an outcome of crack bridging mechanisms by the ductile brass phase, rather than a diffused array of nucleated shear bands in the hard BMG and arrest by the ductile reinforcing phase. The site of the first shear band initiation and process zone size were studied by the experimental estimation and the 3D FEM simulation and it shows that the critical stress and strain for parallel and normal loading composites, respectively, controlled the local fracture commence over a characterized size scale.

5.2 INTRODUCTION:

Although bulk metallic glasses (BMGs) as amorphous metals exhibit high strength, perfect elastic behavior and corrosion resistance at room temperature [1], however, they also exhibit very limited macroscopic plasticity with the highly localized shear bands, followed by crack initiation and unstable crack propagation [2,3]. To prevent the catastrophic failure, a new class of BMG composites has been developed by introducing different ductile metal

reinforcements, such as particles, fibers, or in situ formed precipitates, which lead to higher ductility, fracture toughness and fatigue endurance [4, 5, 6]. It has been observed that the shear bands can transverse the ductile reinforcement [6], which also would inhibit the propagation of localized shear bands within the BMG. The size and volume fraction of the reinforcements also play an important role on the incremental ductility of BMG composites [7, 8].

Recently, the Ni-based BMG and BMG composite containing brass fibers were fabricated by warm extrusion of gas atomized powders [9] and the plasticity of the BMG composites with different volume fractions and powder sizes were studied. The results showed that the BMG composite with 40% volume fraction of the brass phase showed highest ductility and the powder size of the brass is less than 63 μm. The mechanical properties of the BMG and BMG composite have been tested by uniaxial compression test along the extrusion direction and the stress-strain curve is shown in Fig.5.1, in which a monolithic Ni-base BMG by Cu-mold injection casting was compared [10]. As shown in the Fig.5.1, the injection casting BMG has the highest strength with 2% plastic strain to failure and the BMG by warm extrusion didn't show any plastic strain before failure. But the BMG composite has improved ductility compared to the warm extrusion BMG.

Indentation experiments are increasingly being used to evaluate the mechanical properties of bulk metallic glasses, due to their very limited ductility. The deformation filed under the indenter experiences a constraint plastic flow, and thereby provides stable deformation path to study the evolution of the deformation mechanisms. In order to reveal the deformation field under indentation, serial sectioning and etching techniques are utilized

[11]. A new experimental methodology to obtain in-situ observation of the evolution of the deformation behavior of bulk metallic glass under a cylindrical indenter has been developed [12,13], which resolved the much-needed information on the temporal and spatial evolution of the shear bands.

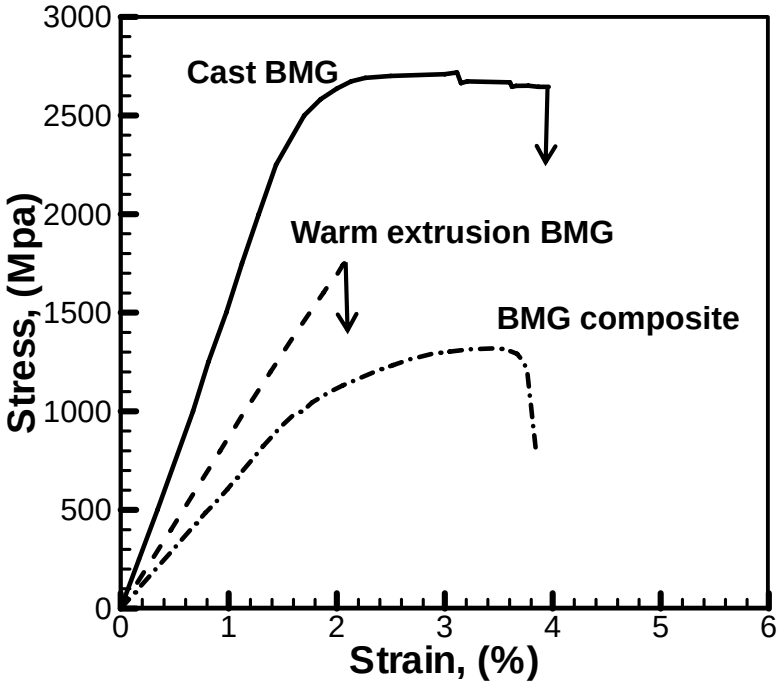

Figure 5.1 Stress-strain curves for the injection cut BMG, warm extrusion BMG and BMG composite reinforced by 40% brass under uniaxial compression test. [10]

In this study, the evolution of the deformation and damage in the BMG/Brass composite system was studied with an experimental set up that enables in-situ observations during the course of a wedge like cylindrical indentation. By quasi-static loading mode, the BMG/Brass composite was indented in two directions, parallel and normal to the extrusion direction, and more details will be presented in the following sections.

5.3 EXPERIMENTS

Material System

The composite studied was the Ni-rich $Ni_{59}Zr_{20}Ti_{16}Si_2Sn_3$ metallic glass matrix composite, containing a ductile brass phase by warm extrusion method. The initial amorphous and ductile phase powders were spherical with the same size range (<63μm) and the volume fraction of the brass phase was 40%. The resulting reinforcement morphology in the composite was short discontinuous fibers and aligned in the warm extrusion direction and the interparticle spacing (λ) along the direction normal to the extrusion direction is 65μm measured by line-intercept method (Fig.5. 2a). A homogeneous BMG matrix only sample "termed as *monolithic BMG*" was also prepared separately by identical warm extrusion processing for comparison (Fig.5. 2b). Both the x-ray diffractometry (XRD) and DSC studies indicated that the existence of amorphous and brass phases in composite sample and no devitrification occurred in monolithic sample throughout the extrusion process. A more detailed introduction about the fabrication of this metallic composite has been given by ref [9].

Two BMG composite specimens with different loading orientations were tested in this study. One of the samples was loaded along the extrusion direction with a cross section of 2.72mm in width by 6.35mm in height (*indentation direction*) and the total length of 6.43mm. The other composite sample was loaded normal to the extrusion direction with same cross section dimension as the parallel loading specimen and total length of 16.3mm. The monolithic BMG specimen has the same dimension as the composite of normal loading.

Experimental Setup

An Instron 8862 servoelectric loading frame was used to do the cylindrical indentation experiments, with loading rate of 1μm/s. The loading fixture is shown in Fig.5. 2c [12], which could ensure the contact line between the indenter and specimen top surface was perpendicular to the front plane of the sample. SiC wedge like cylindrical indenters with root radii, R of 0.8, 1.6, and 2.4mm were used in this study. On the front surface of the samples, the evolutions of the deformation zone underneath the indenter were recorded simultaneously with the loading by a progressive-scan camera (SPOT Insight CCD array of 2048x2048) with a traveling microscope having $5\times$ objective lens and $2\text{mm}\times 2\text{mm}$ field of view. Sufficient illumination was required in the indentation region and imaging rate is 2 images per second.

5.4 RESULTS:

Macroscopic trends

The resulting load-indentation depth curves for two loading directions of the BMG composite and monolithic BMG with same indenter radius R of 0.8mm are summarized in Fig.5. 3a, in which the elastic stiffness of the loading fixture has been removed. A full surface contact was established when the linear elastic deformation started, at which zero indentation depth of the force-displacement curves was set. As can be seen, the monolithic BMG specimen exhibited the largest stiffness and very limited ductile deformation before the catastrophic failure. On the other hand, different loading directions resulted in an anisotropic behavior for the BMG composite case. The sample that was indented in parallel direction to the reinforcement yielded higher stiffness, but still failed in an unstable manner without

permitting a controlled unloading, while the sample of normal loading shows higher ductility but relative lower stiffness. Since the experimental set up enables the direct observation of the nucleation of the shear bands and continuous evolution of deformation under the indenter, the load levels at which the first appearance of the shear bands are also indicated in Fig.5. 3a.

To explore the role of different indenter radii on the mechanical properties of the BMG composite, there are two additional indentation tests conducted on the normal loading composite sample with different radii R of 1.6 and 2.4 mm. The load-indentation depth curves for the normal loading composite with 3 different indenter radii are shown in Fig.5. 3b, which also indicates the load levels of the first shear band initiation in each case. From Fig.5. 3, it shows that with same indenter radius (R=0.8mm) the parallel loading composite initiated the shear band at the lowest load level and monolithic BMG started at highest load level, while for the normal loading composite, the lager indenter radius, the higher load level to initiate the shear band. Similar results were reported in the cast BMG wedge like cylindrical indentation tests [12].

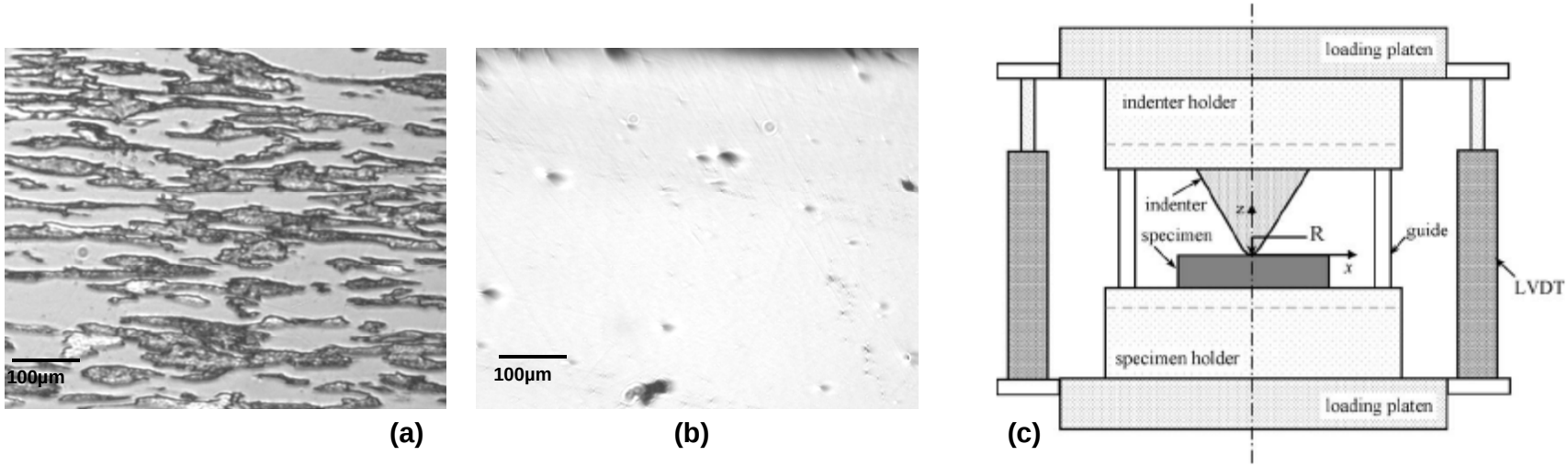

Figure 5.2 (a) Microstructure of the composite BMG, containing a 40% volume fraction brass phase. (b) The monolithic BMG matrix. (c) Schematic of the loading configuration, after [12].

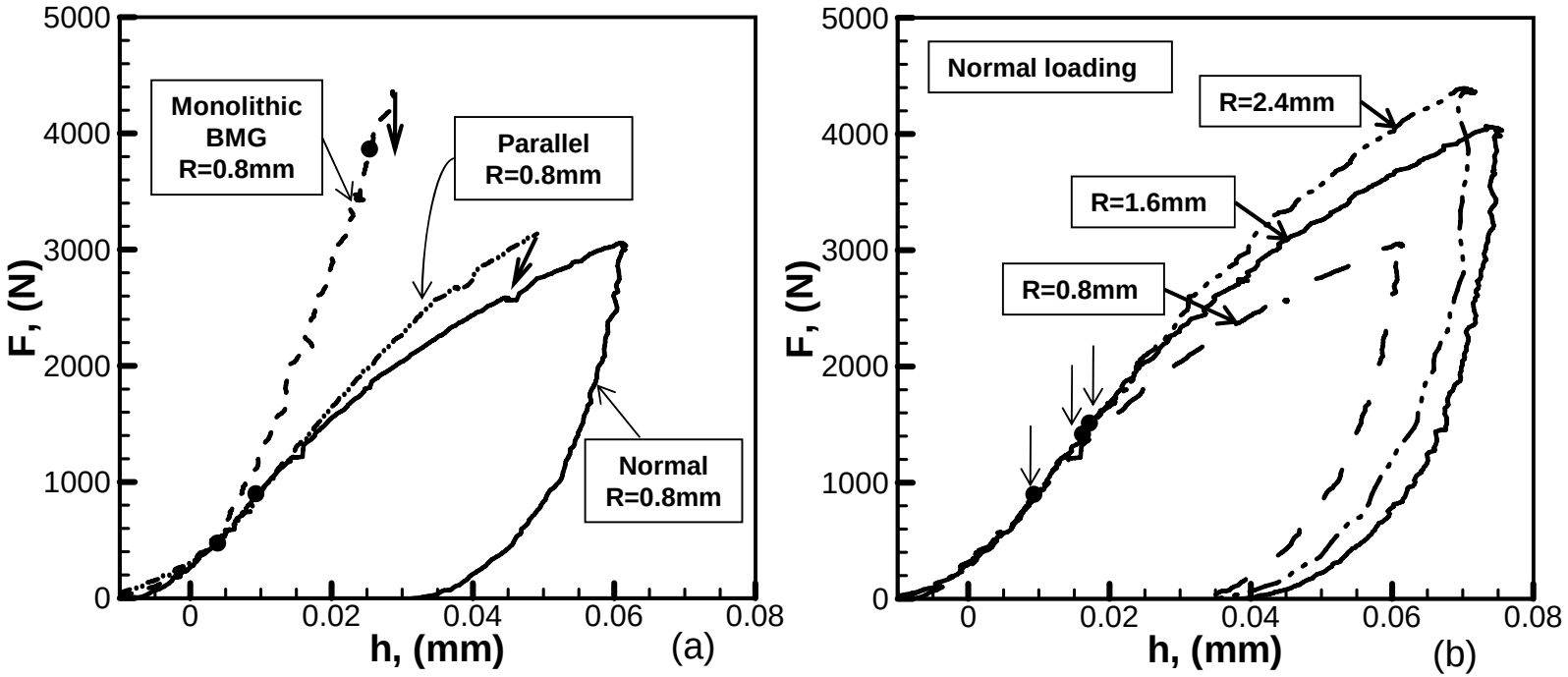

Figure 5.3 Force – displacement curves of the cylindrical indentation tests and the positions of the first shears band initiation marked with solid circles. (a). Indentation tests on monolithic BMG, parallel loading composite and normal loading composite samples, with indenter radius R=0.8mm. (b). Indentation tests of the normal loading composite sample with indenter radius ranging from 0.8mm to 2.4mm.

Evolution of the deformation and damage

The indentation process of the normal loading BMG composite with indenter radius of 0.8 mm is summarized in Fig.5.4. The force-indentation depth curve is shown in Fig.5. 4a. There are several different loading stages marked with different letters on the curve and Fig.5. 4b-g show the corresponding images, which were recorded during the course of the indentation test. The images in Fig.5.4 are cropped ones that only show the regions underneath the indenter. Fig.5. 4b indicates the first appearance of the shear bands, which was nucleated at the interface of the BMG and brass phase. The indenter position was marked with white dash line, which could be adjusted from the rest of the image. And the blurred region between the indenter and the specimen top surface is due to the shade of the indenter under illumination. Fig.5. 4e-g show that a limit finite deformation zone was formed immediately underneath the indenter with out of plane motion during the indentation and a dark region correspondingly appeared in the images. With the increasing load more shear bands initiated and then turned to be cracks with radial emanation from the indenter. However, there are only several major cracks propagating further along the crack paths during the indentation test and lots of microcracks emanating in the glass matrix phase along the indentation direction.

The final microstructure of this normal loading composite was examined by SEM and scanning electron micrographs for deformation and damage zone closed to the indenter are shown in Fig.5. 5, where shear bands and cracks originated at the interface of the BMG and brass phase with some evidence indicated by arrows in Fig .5a, c. We also observe an extensive bridging of those well-developed microcracks that are parallel to the indentation

direction by the brass phase. Because of the compression stress state in the radial direction, there are no delamination found when the cracks encountered the brass fibers and Fig.5. 5b has indicated how the major crack passed through the brass fibers. More details about the evolution of microcracks in the BMG matrix are summarized in Fig.5. 6, in which some of the microcracks appeared in the middle of the brittle matrix (Fig.5. 6c) and some consequent contact between the microcracks surfaces are observed, as shown in Fig.5. 6 a, b, d.

For the parallel loading BMG composite, the recorded images about the evolution of the deformation zone are shown in Fig.5.7. In the force-displacement curve Fig.5. 7a, different loading stages are marked with different letters and Fig.5. 7 b-g show the sequence of images. As observed from Fig.5. 7b, the damage initiation took place at an early stage with the debonding along the interface of the reinforcing phase. This interfacial cracks quickly developed into major cracks (Fig.5. 7 c-g) that became unstable very quickly without permitting evolution of usual deformation zone below the indenter. The SEM image about the final damage zone of the parallel loading composite is indicated in Fig.5. 8a, in which shows the details of the major crack leading fracture (Fig.5. 8b). After the composite failed, the broken parts didn't separate from each other and they are connected by some intact brass fibers which are illustrated in Fig.5. 8c.

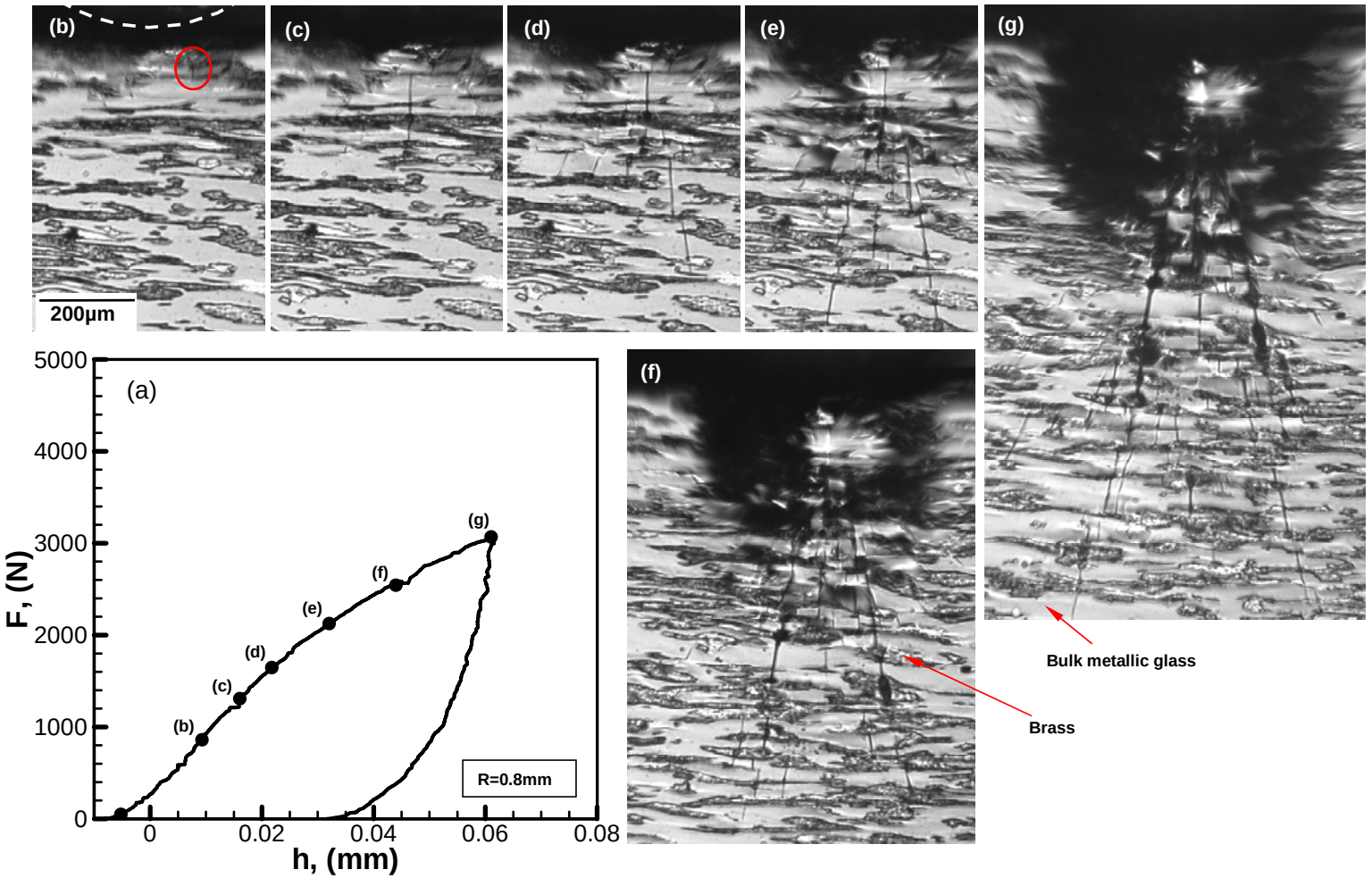

Figure 5.4 The evolution of the deformation zone, for the normal loading composite under cylindrical indentation test with indenter radius of 0.8mm. (a) the force-indentation depth curve. (b)-(h) images immediately underneath the indenter corresponding to different loading stages, which are marked in the force-displacement curve.

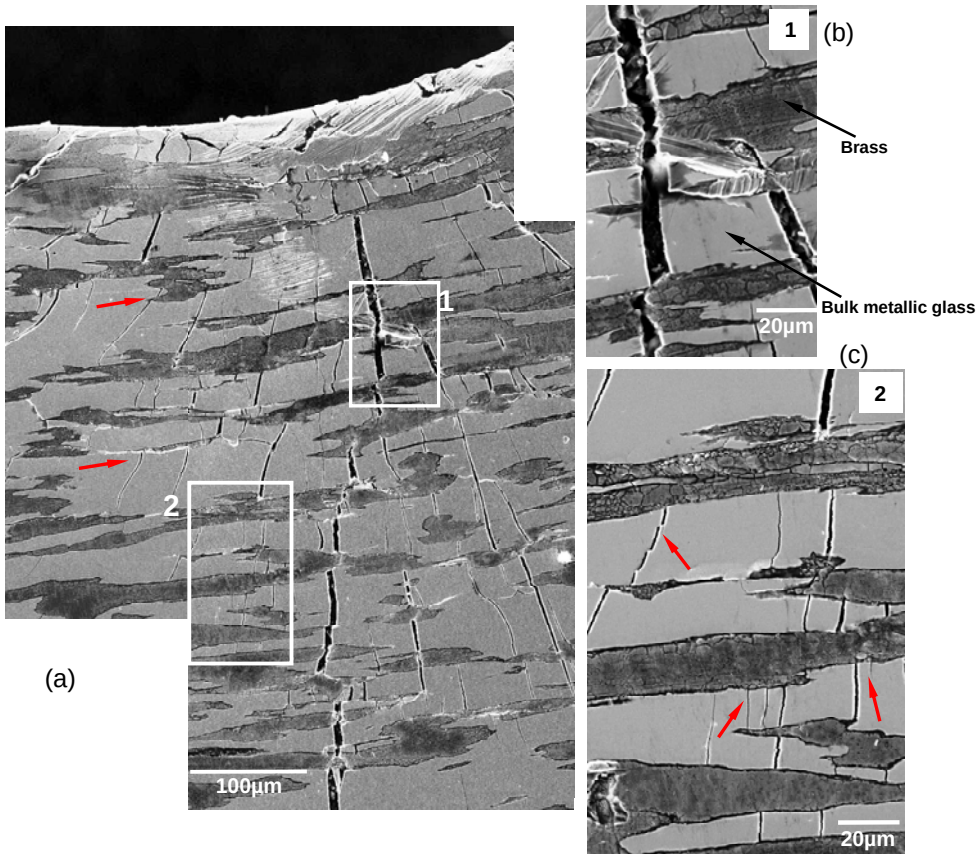

Figure 5.5 SEM images of the deformation zone for the perpendicular loaded specimen with indenter radius of 0.8mm after unloading. (a) SEM images for the finite deformation zone underneath indenter. (b) major crack propagation by ductile rapture of brass fibers, which is the detail of the window 1 in (a). (c) microcracking evolution in the glass matrix of the deformation zone, which is the detail of the window 2 in (a).

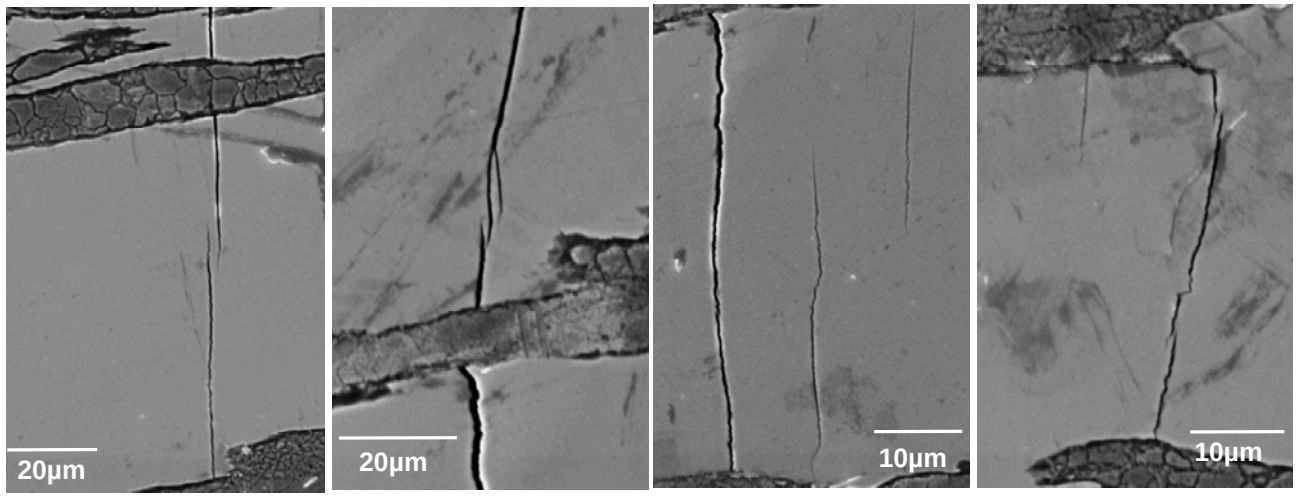

Figure 5.6 SEM results show more details about the microcracks evolution in the metallic glass matrix

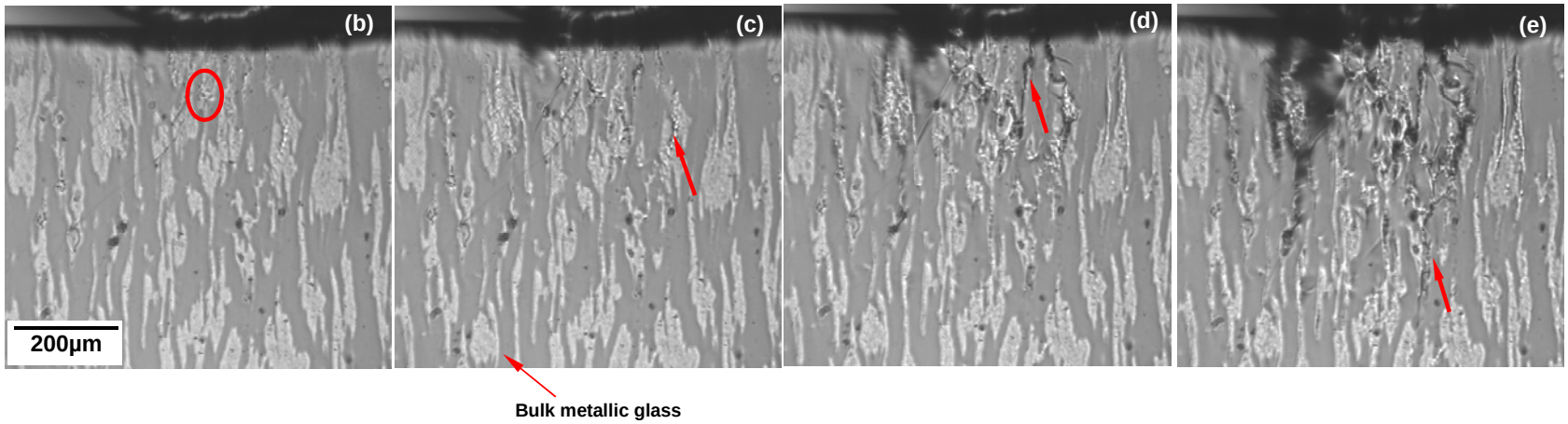

Figure 5.7 The evolution of the damage zone, for the parallel loading composite under cylindrical indentation test with indenter radius of 0.8mm. (a) The force-indentation depth curve. (b)-(h) images immediately underneath the indenter corresponding to different loading stages, which are marked in the force-displacement curve.

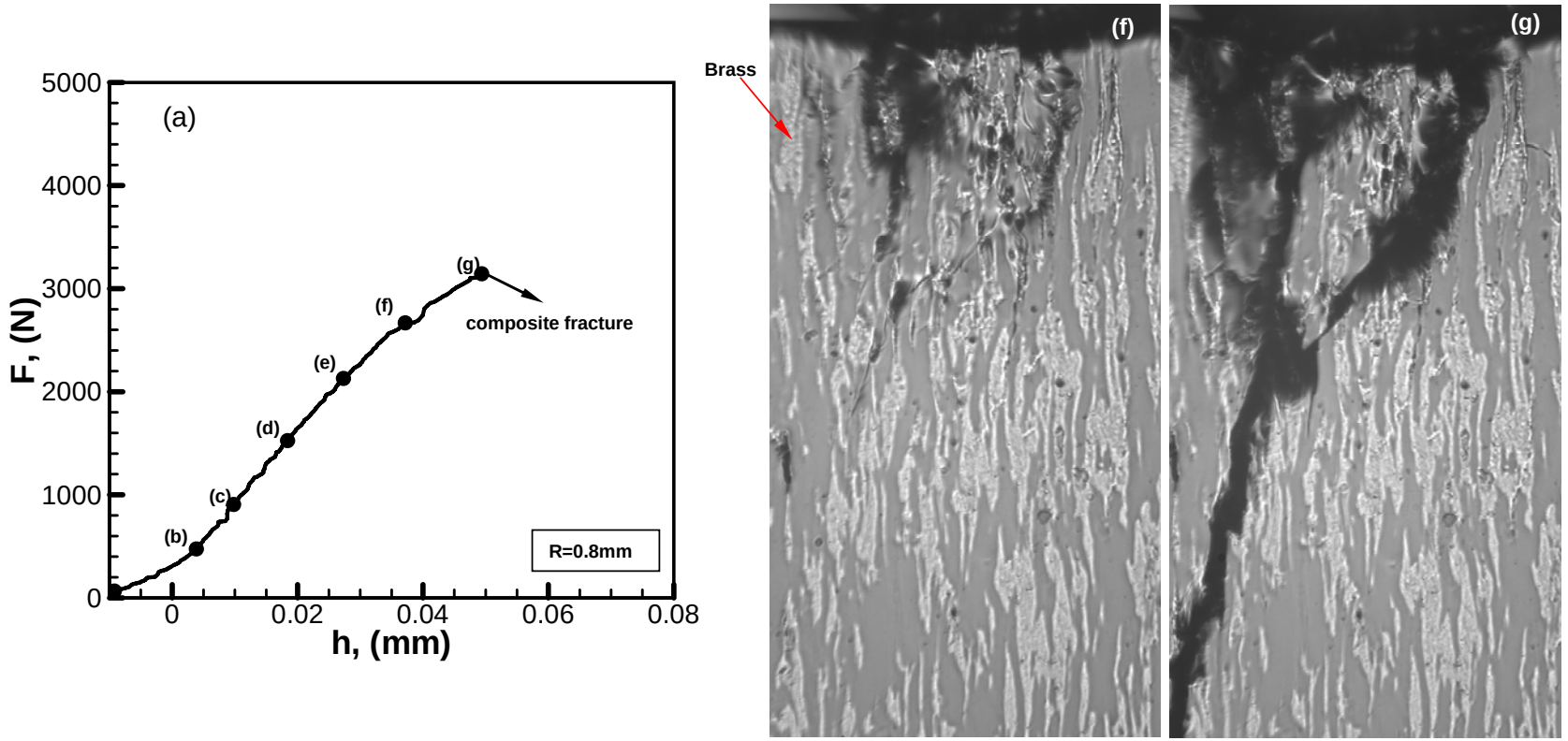

Figure 5.7 The evolution of the damage zone, for the parallel loading composite under cylindrical indentation test with indenter radius of 0.8mm. (a) The force-indentation depth curve. (b)-(h) images immediately underneath the indenter corresponding to different loading stages, which are marked in the force-displacement curve.

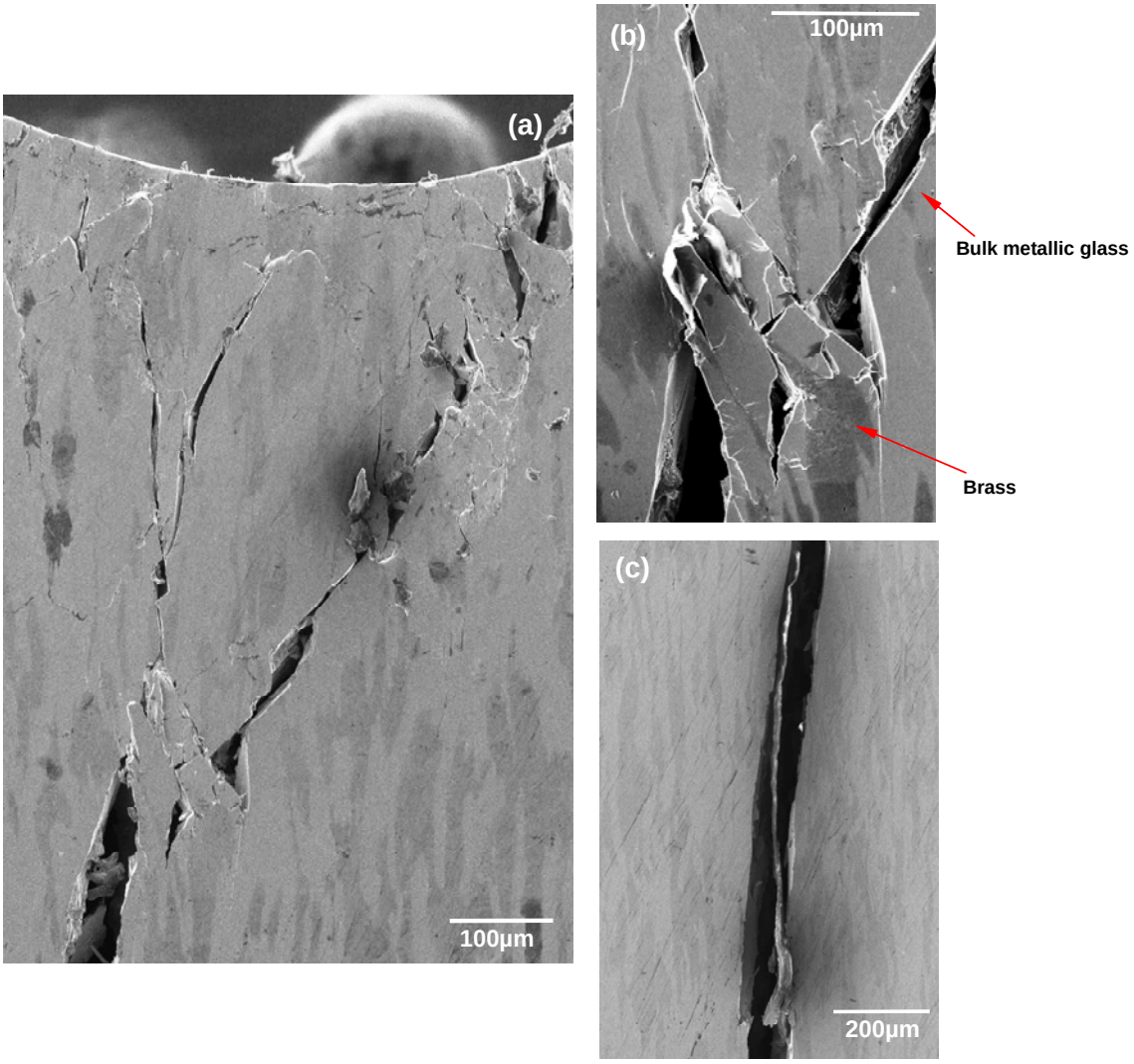

Figure 5.8 SEM images of the deformation zone for the parallel loaded specimen with indenter radius of 0.8mm after fracture without separation. (a) SEM images for the finite deformation zone underneath indenter. (b) the details about the mergence of two major cracks (c) intact brass fibers connected two broken parts of the composite along the failure crack .

Deformation mechanism

Fracture Toughness

The macroscopic load-indentation in conjunction with the monitored crack trajectories under the indenter are used to estimate the fracture toughness of the composites. Then energy release rate, G (or J-integral) as measure of the energy available for a crack extension is given by:

$$G = J = -\frac{d\Pi}{dA} \qquad (1)$$

where Π is the potential energy of the tested specimen and A is the crack area [14,15]. The evolutions of the crack underneath the indenter were determined from the images that were simultaneously recorded during the course of the indentation. Although, the measured crack lengths from the front surface cracks may not be the through-thickness cracks as implied by the Eq.1, however, we assumed the measured surface crack length would provide an average estimate of the total crack length per unit specimen thickness. The driving energy for fracture is estimated as total energy supplied to the system by the indenter (area under load-indentation depth curve) and subtracting the elastic unloading energy at each load. In doing so, the specimen compliance was assumed not to change significantly with the crack advances and thereby the slop of unloading curves at different stages of crack advance could be assumed to remain the same as that of the final unloading curve in Fig.5. 3. The variation of energy and incremental total crack length for each indentation test of the BMG composite are summarized in Fig.5. 9a. As can be seen, the energy dissipated in the normal loading cases for the composite is much higher than the parallel loading case. Fig.5. 9b illustrates the

derivative of the energy with incremental crack area based on Fig.5. 9a. The energy release rate (G=J) at the steady state crack propagation was around 10 KJ/m^2 for the normal loading, while for the parallel loading ,this value was around 5 KJ/m^2. Since the energy release rate can be related to the stress intensity factor K:

$$G = J = \frac{K^2}{E'} \quad (2)$$

where $E' = E/(1-\nu^2)$ for plane strain, ν is the Poisson's ratio and E is the Young's modulus of the composite. Both E and ν were estimated from the law of mixtures based on the volume fraction of two phases in the composite. There for the critical stress intensity factors for the composite are around to be 34 $MPa\sqrt{m}$ and 24 $MPa\sqrt{m}$ for normal and parallel loading cases, respectively.

Process zone size

The loading levels of the first shear band initiations have been marked in the force-indentation depth curves (Fig.5.3) for each indentation test. Therefore, the nucleation pressure P underneath the indenter can be estimated by [16]:

$$P = \frac{F}{2aw} \quad (3)$$

where F is the applied loading level, w is the width of the sample and $a = \sqrt{2Rh}$, which is the contact radius. The indentation depth h could be measured from Fig.5. 3 and R is indenter radius. The normalized process zone size (c/R) for the first shear band nucleation also could be approximated by the Cavity Expansion Model:

$$\frac{c}{R} = \left\{\frac{h}{R}\left(\frac{E/k}{\pi(1-\nu^2)}\sqrt{\frac{h}{2R}} + \frac{1-2\nu}{1-\nu}\right)\right\}^{1/2} \qquad (4)$$

Here, Tresca Criteria is assumed and $k = 0.5\sigma_y$ where $\sigma_y$is the yield stress, E is the Young's modulus, R is the indenter radius and ν is the Poisson's ratio. The variation of the nucleation pressure P and the normalized process zone size (c/R) for all of the indentation tests are summarized in Fig.5. 10a. The yield stresses for both of the BMG composite and the monolithic BMG are approximated by the uniaxial compression yield stress along extrusion direction shown in Fig.5.1 [10] and the indentation depths are measured form the force-displacement curves (Fig.5.3) when the first shear bands initiated. We observe that the nucleation pressures for all of the BMG composites are independent on the loading direction and almost at the same level, which is around $1200MPa$. On the other hand, the monolithic BMG has much higher nucleation pressure about 3200 MPa, comparable to the one of cast BMG [12]. It also has the largest normalized process zone size, which is around 0.4. For the BMG composite with different loading directions, the normalized process zone size are 0.14 and 0.24 for the parallel loading and normal loading, respectively.

Since the images, for the moment when first shear band appeared, were taken during the course of the indentation tests, the distance (z) between the location of the first shear band and the center of the indenter could be approximately measured from the images. Fig10.b illustrates the distances (z) for the BMG composites and monolithic BMG, which are normalized by the process zone size c based on Eq. 4. As can be seen, the monolithic BMG has almost the same z/c value (0.35) as the composite of normal loading, for which the value

z/c is independent on the indenter radius R. On the other hand, the normalized distance z/c for the parallel loading composite is around 1.1 much higher than the rest.

5.5 DISCUSSION

The utilization of the wedge like cylindrical indentation has ensured the stable evolution of the deformation mechanism under the indenter by confined plastic flow. The variation of the macroscopic responses for all situations has shown that the monolithic BMG has higher stiffness with little ductility and very small zone of shear bands started under the indenter, leading to the development of major cracks that traversed the entire sample in an unstable manner. However, both of the macroscopic response and the microstructure of the damage zone have indicated that the BMG composite has high anisotropic properties with loading orientations. For the normal loading case, an extensive nucleation of cracks emanating in a radial direction can be seen and the network of cracking does not resemble the usual net-work of shear band formation that is usually seen for homogeneous cast BMG [12]. Based on the evolution of the damage zone, all of the cracks started as shear band first emanating from the BMG/Brass interface, while the broken brass fibers along the crack trajectory and the crack bridging mechanism by the brass fibers were observed during the crack propagation, which have a significant contribution to the fracture toughness. In the parallel loading case, once the interfacial cracks along the BMG/Brass phase were nucleated, they turned into the major cracks and lead the fracture in an unstable way. It appears that the increase of ductility and toughness in the normal loading direction is a result of both dilation originating from the nucleation of a large number of radial cracks and bridging of the main cracks by the ductile reinforcing phase.

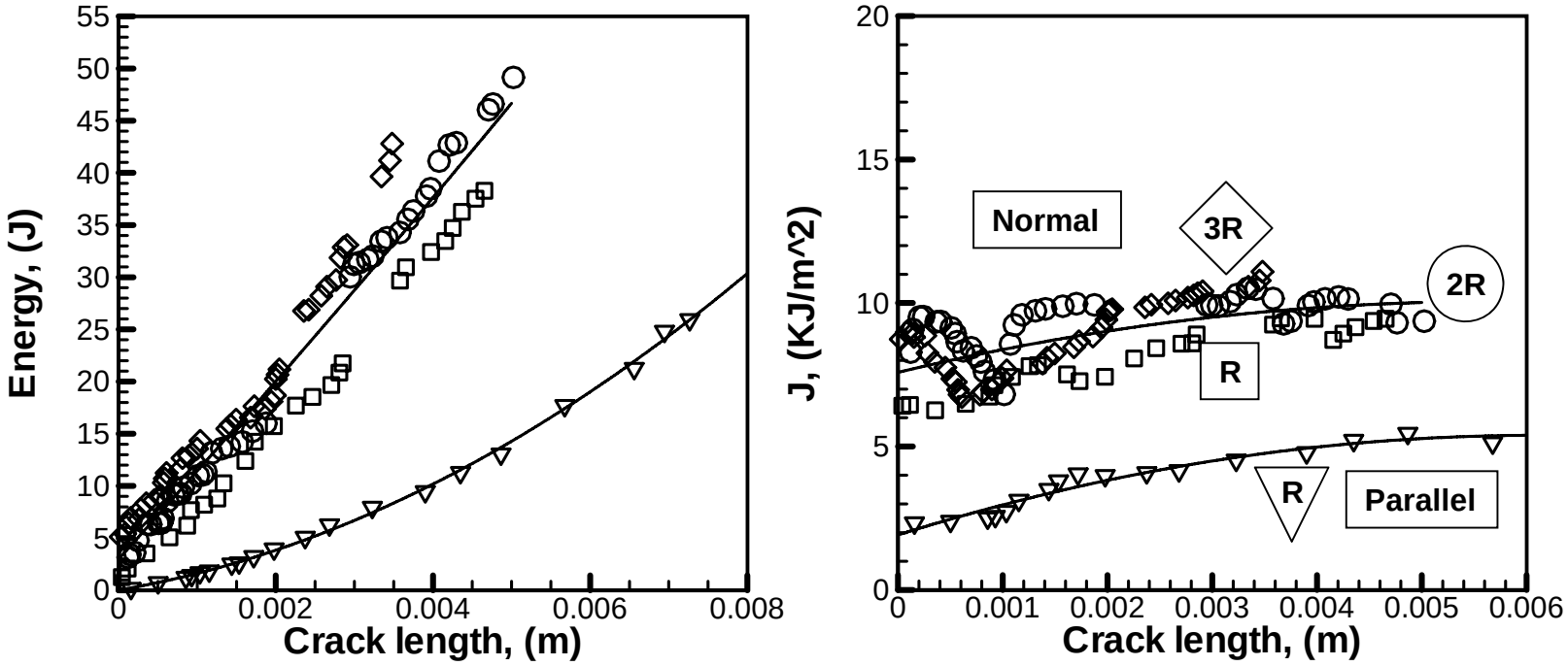

Figure 5.9 (a) Variation of total fracture energy and incremental total crack length obtained from the indentation test of BMG composite. (b) The energy release rate G=J and crack increments curve for BMG composite for the different loading orientations.

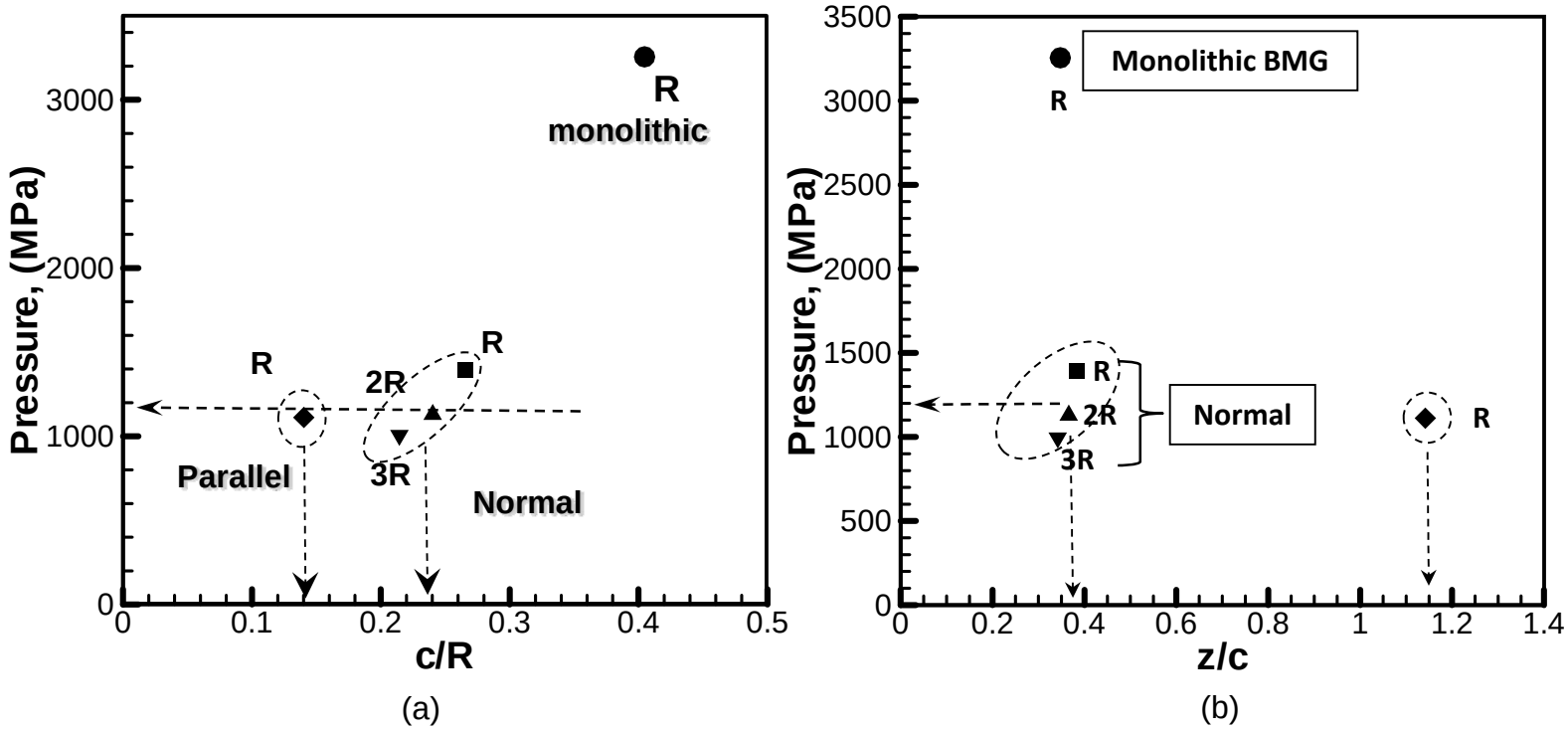

Figure 5.10 (a) the variation of the pressure and the ratio of the process zone size (c) normalized by indenter radius, when the first shear band nucleated in different specimens. R is the indenter radius which is 0.8mm. (b) the variation of the pressure and the ratio of the first shear band initiation position normalized by the corresponding plastic zone size.

At ambient temperatures, the reported fracture toughness values for most of the BMGs are in the range of 15~20$Mpa\sqrt{m}$ [17, 18]. In this study, as discussed in Section 3. 3.1, the fracture toughness values of the normal and parallel loading composites are proximately 34 $Mpa\sqrt{m}$ and 24 $Mpa\sqrt{m}$, respectively. These values are also comparable to the one of Zr-rich metallic glass composite [5]. Although, the facture toughness values for the composites reported here may not be exactly equal to the fracture toughness values that can be provided by standard fracture toughness tests, nevertheless, a significant toughening can be inferred by simple inspection of the load vs. indentation depths (Fig.5.3).

To understand the essence of the facture, the investigation of the local fracture is very important, from which the occurrence of macroscopic fracture is accumulated. In the BMG composite as shown in Fig 10.a, when the normalized process zone size (c/R) is 0.14 and 0.24 for the parallel and normal loading, respectively, the local fracture commenced with shear band initiation , which is independent on the mean pressure. For the indentation with radius R of 0.8mm, the plastic zone size of the parallel loading composite C_P is about 2λ and the one of the normal loading composite C_N is about 3λ, where λ (65μm) is the interparticle spacing of the brass fibers in the indentation direction. Meanwhile, a FEM model with 3D hexagon elements by ABQUS was developed to simulate this wedge like cylindrical indentation with different radii, in which the composite is assumed to be isotropic, perfect plastic and Tresca Criteria was utilized. The FEM results showed that for the radius R of 0.8mm, when the local fracture loading levels were achieved, the aspect ratio of the process zone that the width (B) over the height (A) is around 0.585, which agrees with the ratio of $C_P/C_N = 0.583$ from the experimental estimation. This result has indicated that both critical

pressure and the size scale are needed to trigger the local fracture commence, similar results were reported about the cleavage fracture in front of the sharp crack tip of mild steel [19].

As shown in Fig10.b, we observed that sites of the initiation shear band from the indenter tip have a same normalized value (0.35) in the homogeneous BMG and the normal loading composite, in which the z/c is independent on the radius R. On the other hand, the composite of parallel loading case, the location is at 1.15 of the ratio z/c. From the FEM results with different radii, at the loading levels that shear band initiated, a radial line was extracted under the indenter center, and the stress and strain distributions along this line with different radius are summarized in Fig.5. 11. It shows that the maximum tensile strain takes place at 0.35 of the ratio z/c for all of three indenter radii and for the R of 0.8mm case, the maximum tensile stress is at 1.1 of the z/c ratio. There are two kinds of local fracture mechanisms, critical stress control and strain control. Base on the experimental observation and the FEM simulated results, it indicated that both the homogeneous BMG and the normal loading composite are critical strain controlled, while the composite of parallel loading is critical stress controlled. Therefore, with certain pressure under the indenter, for the parallel loading composite, when the critical debonding force was achieved over a characterized size scale, the local fracture commenced. However, for the normal loading composite, the local fracture started at maximum tensile strain over a critical distance from the indenter tip.

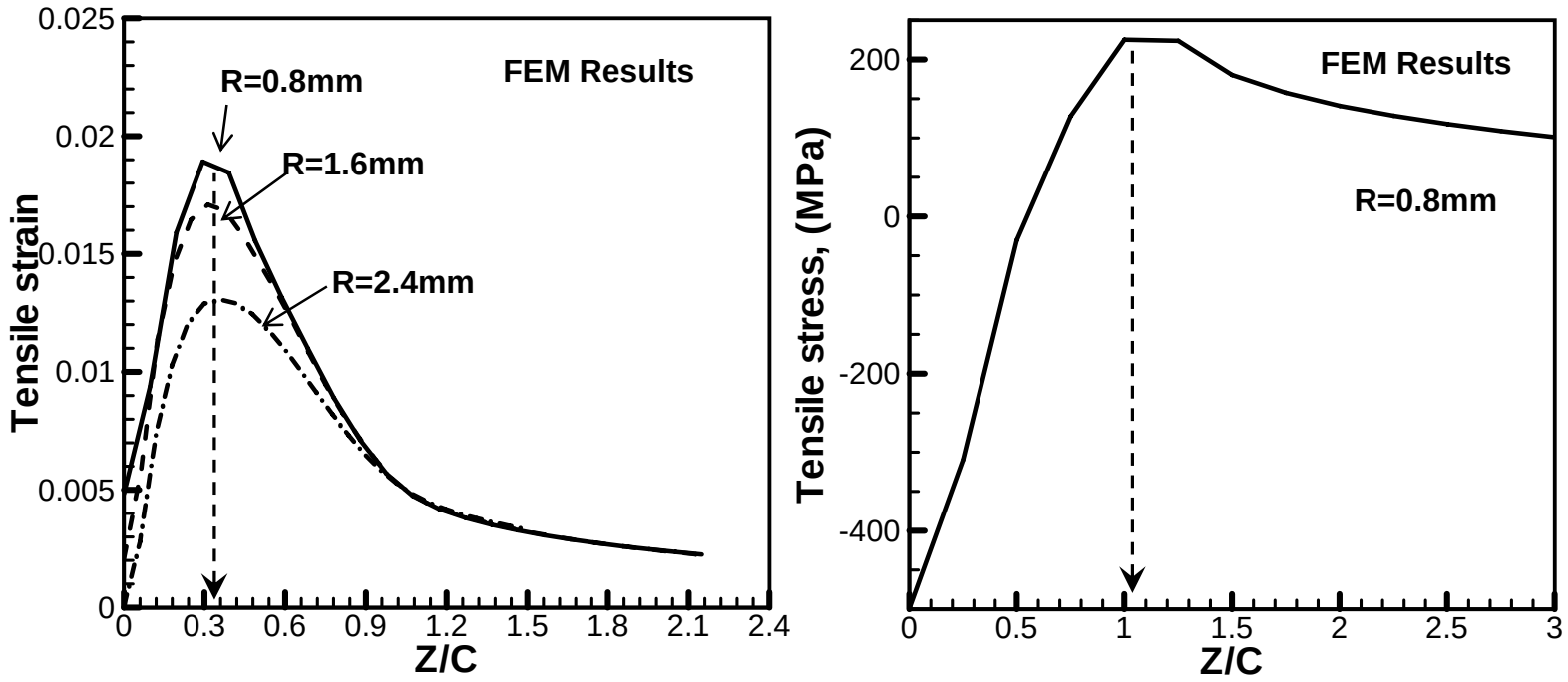

Figure 5.11 (a) the variation of the strain component to the ratio of z/c, where z is the distance between the indenter tip and the points on the radial line underneath the indenter, c is the plastic zone size at the nucleation stage. (b) the variation of the tensile stress to the ratio of z/c at the parallel loaded composite crack nucleation stage.

5.6 CONCLUSION

The deformation mechanism in Ni-based bulk metallic glass composite has been studied by cylindrical indentation tests. The metallic glass composite containing brass reinforcing phase shows strong anisotropy in terms of deformation and damage evolution behavior. It appears that ductile reinforcements not only promote early nucleation of the localized shear bands, but they also intrinsically modify crack growth behavior with crack bridging mechanisms. The agreements of the experimental observation and the FEM simulation results have shown that the local fracture is stress and strain controlled for the parallel and normal loading composites, respectively, over a critical size scale.

5.7 ACKNOWLEDGEMENT

This work is supported by US-National Science Foundation NSF through grant No. CMS-0134111. The author SBB was supported by the Department of Energy-Basic Energy Sciences under Contract No. DE-AC0207CH11358. The authors thank Dr. D.J. Sordelet for providing the samples.

5.8 REFERENCES

1. Bruck H.A., Christman T., Rosakis A.J. and Johnson W.L., "Quasi-static constitutive behavior of $Zr_{41.25}Ti_{13.75}Ni_{10}$ $Cu_{12.5}Be_{22.5}$ bulk amorphous alloys", Scripta Metallurgica et Materialia, v30, n4, Feb 15, 1994, p429-434.

2. Bruck H.A, Rosakis A.J., Johnson W.L., "Dynamic compressive behavior of beryllium bearing bulk metallic glasses", Journal of materials Research, v11, n2, Feb, 1996, p503-511.

3. Gilbert C.J, Ritchie R.O, Johnson W.L, “Fracture toughness and fatigure-crack propagation in a Zr-Ti-Ni-Cu-Be bulk metallic glass”, Applied Physics Letters, v71, n4, Jul28, 1997, p476.

4. Szuecs F., Kim C.P., Johnson W.L., “Mechanical properties of $Zr_{56.2}Ti_{13.8}Nb_{5.0}Cu_{6.9}Ni_{5.6}Be_{12.5}$ ductile phase reinforced bulk metallic glass composites”, Materials Science Forum, v360-362, 2001, p43-48.

5. Flores K.M, Dauskardt R.H., “Fracture and deformation of bulk metallic glasses and their composites”, Intermetallics, v12, n7-9 SPEC. ISS., July/September, 2004, p1025-1029.

6. Flores, K.M., Johnson, W.L, Dauskardt, R.H., “Fracture and fatigue behavior of a Zr-Ti-Nb ductile phase reinforced bulk metallic glass matrix composite”, *Scipta Mater.*, 49 (12), 2003, 1181-1187.

7. Choi-Yim, H., Busch, R., Koster, U., Johnson, W. L., “Synthesis and characterization of particulate reinforced $Zr_{57}Nb_5Al_{10}Cu_{15.4}Ni_{12.6}$ bulk metallic glass composite”, *Acta Mater*., 47 (8) , 1999,2455-2462.

8. Conner R.D., Dandliker R.B., Johnson W.L., 1998, “Mechanical properties of tungsten and steel fiber reinforced $Zr_{41.25}Ti_{13.75}Cu_{12.5}Ni_{10}Be_{22.5}$ metallic glass matrix composites, *Acta Mater*., 46 (17), 6089-6102.

9. Lee M.H., Bae D.H., Kim D.H., Sordelet D.J., “Synthesis of Ni-based bulk metallic glass matrix composites containing ductile brass phase by warm extrusion of gas atomized powders”, Journal of Materials Research, v18, n9, September, 2003, p2101-2108.

10. Lee M.H., Lee, J.Y., Bae D.H., Kim W.T, Sordelet D.J., Kim D.H., “ A development of Ni-based alloys with enhanced plasticity”, Intermeallics, v12, n10-11, October/November, 2004, p1133-1137.

11. Donovan P.E., “Plastic flow and fracture of $Pd_{40}Ni_{40}P_{20}$ metallic glass under an indentor”, Journal of Materials Science, v24, n2, Feb, 1989, p523-535.

12. Antoniou A., Bastawros A.F, Lo C.C.H., Biner S.B., “Deformation behavior of a zirconium based metallic glass during cylindrical indentation: In situ observations”, Materials Science and Engineering A, v394, n1-2, Mar 15, 2005, p96-102.

13. Antoniou A., Bastawros A.F., Biner B., “ Experimental observations of deformation behavior of bulk metallic glasses during wedge-like cylindrical indetation”, Journal of Materials Research, v22, n2, February, 2007, p514-524.

14. Irwin, G.R, Sagamore Research Conference Proceedings, v2, 1956, p289-305

15. Rice J.R, Rosengren G.R., “Plane strain deformation near a crack tip in a power-law hardening material”, Journal of Mechanics and Physics of Solids, v16, n1, Jan, 1968, p1-12.

16. Johnson K.L., 1987, contact mechanics.

17. Flores K.M., Dauskardt R.H., “Enhanced toughness due to stable crack tip damge zone in bulk metallic glass”, Scripta Materiallia, v41, n9, Oct, 1999, p937-943.

18. Lowhaphandu P., Lewandowski J.J., “Fracture toughness and notched toughenss of bulk amorphous alloy: Zr-Ti-Ni-Cu-Be”, Scripta Materialia, v38, n12, May12, 1998, p1811-1817.

19. Ritchie R.O., Knott J.F., Rice J.R., “On the relationship between critical tensile stress and fracture toughness in mild steel”, Journal of Mechanics and Physics of Solids, v21, n6, Nov, 1973, p395-410.

CHAPTER 6: CONLUSIONS

6.1 SUMMARY

In this study, we investigate the inhomogeneous deformation of the BMGs under confined geometry loading configuration and their composites' fracture toughness and the toughening mechanism. Wedge-like cylindrical indentation has been used in this study and in-house developed digital image correlation program is established to assistant the analysis of the plastic deformation evolution.

Firstly, the DIC technique has been explained and the subset method has been calibrated by artificial tension band to exam the localized deformation. Based on the investigation of a sequence of artificial bands with different width, it indicates that DIC technique overestimates the width of the localization, which is the result from several length parameters used in this technique. By exploring the parameters' contribution during the DIC process, an empirical equation has been summarized and the spacing between two continuous sub-windows L_g is very important to determine the resolution. Also, the post DIC process biases the width and strain level within the localization, in which the strain gauge length effects the width estimation and the strain level is much lower than the exact value. Therefore, the strain map just could qualitatively highlight the localization but over estimate the band width especially for the thin localization band. Generally, to understand the localization character by DIC technique, we have to focus on specific localization and analyze the DIC result manually to explore the corresponding properties.

Secondly, experimental study of the plastic flow characterization with ductile metals is used to calibrate the validity of current experimental setup and DIC technique. By digital image correlation technique, the strain maps underneath the indenter have been plotted. The experimental observation of the shape of the plastic zone has confirmed by the one reported in the previous findings about Vickers indentation tests and a unique correlation of the strain distribution has been observed along radial line with different angular positions. Self-similar manner has been proved in both of the radial dependence of the effective strain and the in-plane total strain vectors on reduced Mohr-plane at different loading stages. FEM numerical solution and analytical solution have been utilized to evaluate the experimental measurements. Non-homogeneous plastic deformation and large rotation built up the gradient of plastic deformation which requires introducing geometrically-necessary dislocations. Such constraint deformation could be the reason that introduces extra hardening capability of the material inside of the plastic zone.

Thirdly, experimental study of the inhomogeneous deformation of bulk metallic glass on microscopic level has investigated the evolution of single shear band by fixing the observation location inside of shear band, which includes the nucleation strain level, strain increments inside of the shear band and the situation of the surroundings. The shear band and the surroundings alternatively show their activity and the accumulated strain level inside of the shear band is higher than the one of the surroundings about 3 order magnitudes. To explain the experimental observation about the shear band nucleation, a theoretical model has been used by initializing the experimental parameters and the simulation results are comparable with the experimental measurements, which characterizes the shear band

initiation and post yield response on the microscopic level. Also, the nature of the shear band deformation is simple shear, while the surrounding matrix has pure shear deformation to accommodate the shear band propagation. At the same time, the in-plane mean strain measurement within the shear band shows the dilatation during the shear band evolution.

Finally, the deformation mechanism in Ni-based bulk metallic glass composite containing brass reinforcing phase shows strong anisotropy in terms of deformation and damage evolution behavior. It appears that ductile reinforcements not only promote early nucleation of the localized shear bands, but they also intrinsically modify crack growth behavior with crack bridging mechanisms. The agreements of the experimental observation and the FEM simulation results have shown that the local fracture is stress and strain controlled for the parallel and normal loading composites, respectively, over a critical size scale.

6.2 FUTURE WORK

This dissertation presents an experimental evaluation of Vitreloy-1 the typical BMG's microscopic plastic deformation mechanism, by observing shear band initiation and propagation and relating the experimental measurements with the numerical and analytical models to explain this BMG's microscopic response. Also, by same experimental method, the Ni-based BMG composite by warm extrusion of gas atomized powders has been studied to explain the enhanced ductility and toughening mechanism. In additional, the previous study about Vitreloy-1 [1] had already examined how instabilities in amorphous metals form and propagate under the cylindrical indentation by examining the validity of various

constitutive models and calibrating relevant parameters that are confirmed from BMG's macroscopic experimental response.

As the typical BMG, Vitreloy-1 have a unique combination of properties such as high strength, large elastic strain limit, good formability and corrosion resistance, but fails in an unstable manner by a single shear band propagation at room temperature. Therefore, to improve the ductility and increase the fracture toughness is of scientific as well as industrial interest for the BMGs' development. Very recently, high strength BMGs with enhanced room temperature ductility have been developed [2-5] that show high yield strength (1272~1830MPa) and a "work-hardening-like" behavior. A Cu-based BMG with macroscopic hardening under compression test is shown in Fig. 6.1 [2]. The Scanning electron microscopy (SEM) observation [2] (Fig. 6.2) of surfaces of deformed samples reveals high density of shear bands which are organized in two networks: primary shear band parallel to the fracture plane and secondary shear band perpendicular to the previous ones. Different reasons have been proposed to explain this intrinsic ductility of BMGs: large Poisson's ratio[3], nanocrystalline during deformation [4,6], the presence of distinct short-or medium- range order, and an irreversible production of free volume due to external stress has been claimed to be the reason for work-hardening in BMG[7]. At the same time, a large number of glassy matrix composites with quasicrystalline, crystalline and nanocrystalline second phase dispersions on the nanometer-micrometer length scale have been produced with improved mechanical properties by tuning compositions and the volume fraction of the second phase dispersions through different fabrication processes. However, optimizing the properties require further investigations concerning alloy design and processing conditions.

About the monolithic BMG, although the new developed hardening BMGs have been developed; the deformation mechanisms are still rather poorly understood. Lots of work needs to be done to elucidate the mechanisms of the observed enhanced ductility and hardening phenomenon.

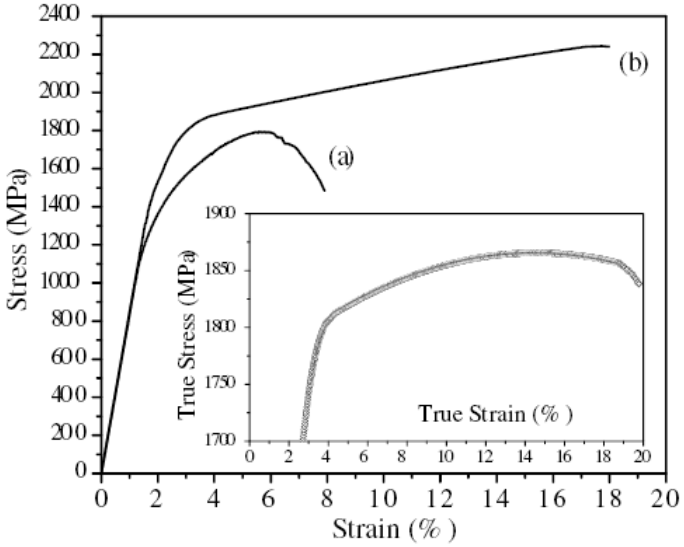

Figure 6.1 Stress-strain curves of (a) Cu50Zr50 and (b) Cu47:5Zr47:5Al5 under compression at a strain rate of 8 _ 10_4 s_1, showing a highly ‘‘work-hardenable’’ metallic glass up to 18% strain. The inset shows the true stress-true strain curve of alloy (b) Cu47:5Zr47:5Al5 as obtained from conversion of the engineering stress-strain values.[2]

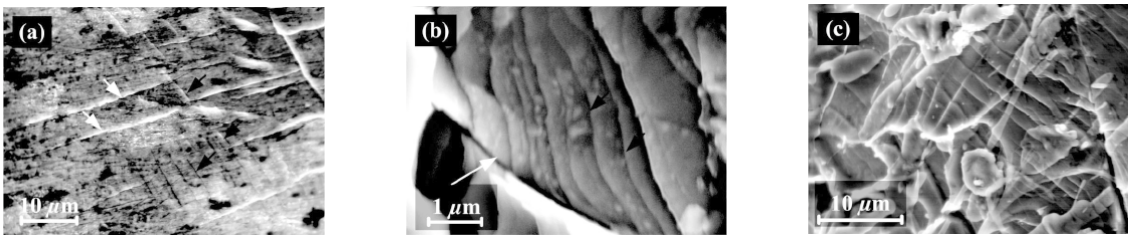

Figure 6.2 (a) SEM secondary electron image of shear bands of Cu50Zr50 representing their high density and interactions between primary (black arrows) and secondary (white arrows) shear bands, (b) very narrow intershear band spacing observed under high resolution scanning electron microscope in a Cu47:5Zr47:5Al5 specimen, and (c) strong interactions of shear bands observed on the fracture surface of Cu47:5Zr47:5Al5.[2]

6.3 REFERENCE

[1] A.M. Antoniou, *Experimental observations of shear band nucleation and propagation in a bulk metallic glass using wedge-like cylindrical indentation*, Thesis (Ph.D.)--Iowa State University, 2006.: 2006.

[2] J. Das, M.B. Tang, K.B. Kim, R. Theissmann, F. Baier, W.H. Wang, and J. Eckert, ""work-hardenable" ductile bulk metallic glass," *Physical Review Letters*, vol. 94, 2005, pp. 1-4.

[3] J. Schroers and W.L. Johnson, "Ductile bulk metallic glass," *Physical Review Letters*, vol. 93, 2004, pp. 255506-1-255506-4.

[4] J. Saida, A.D.H. Setyawan, H. Kato, and A. Inoue, "Nanoscale multistep shear band formation by deformation-induced nanocrystallization in Zr-Al-Ni-Pd bulk metallic glass," *Applied Physics Letters*, vol. 87, 2005, pp. 1-3.

[5] D. Sung, O. Kwon, E. Fleury, K. Kim, and J. Lee, "Enhancement of the glass forming ability of Cu−Zr−Al alloys by Ag addition," *Metals and Materials International, vol.10, No.6 (2004),*pp.575-579.

[6] M. Chen, A. Inoue, W. Zhang, and T. Sakurai, “Extraordinary plasticity of ductile bulk metallic glasses,” *Physical Review Letters*, vol. 96, 2006.

[7] Q. Li and M. Li, “Molecular dynamics simulation of intrinsic and extrinsic mechanical properties of amorphous metals,” *Intermetallics*, vol. 14, 2006, pp. 1005-1010.

APPENDIX: SPECTRAL ANALYSIS OF THE 3D FRACTURE SURFACES FOR ENHANCED MATCHING

A.1 BACKGROUND

The National Institute of Justice (NIJ) has identified high-priority criminal justice technology needs[1] to aid in confirming the guilty and protecting the innocent. NIJ has indentified the need for improved capability to expand the information that can be extracted from traditional types of forensic evidence and to quantify its evidentiary value. One of the identified areas is the impression evidence, where identification of tools is required for quantitative measure and statistical evaluation of forensic comparisons.

The basis for physical matches is the assumption that there are an infinite number of matches all along the fracture break. The factors used in forensic physical matches include 1) dimensional consistency, 2) color, 3) shape of the line of the break i.e., zigzag, curved, straight, etc.; 4) irregularities from point to point along the line of the break; and 5) any toolmarks or imperfections crossing the broken edge[3]. A few studies have attempted a systematic effort to establish a basis for a physical match. Katterwe[4], who examined glass and metal samples, concluded that the fracture surface is highly stochastic with randomly distributed fracture-branches due to the randomness of the microstructure and the grain sizes. Bradley et al.[5] performed a study using duct tape as the fractured medium to determine the validity and error rate associated with conducting fracture match examinations. When the ends were torn by hand (more jagged), the number of matches was higher; 92% versus 81%

for cut ends (smoother ends). There were no errors or misidentifications by the team of forensic scientists for the jagged hand-torn samples. The authors indicated that some of the smooth ends had "insufficient points of comparison to definitively conclude an end match." For fracture surfaces of variety of materials, *an additional method is needed* to compare fractured ends, whenever there are *insufficient features* for optical comparison to link one end to another. Such method should utilize the wealth of the knowledge base for materials microstructure and the fracture process zone characteristics.

Microstructure Feature Scale

The topographic features of a fracture surface are dictated by the details of the material microstructure, as depicted on Fig.A 1. Starting with the general materials' classification, solid materials are crystalline (metals and ceramics), semi-crystalline (polymers) and amorphous (polymers and glasses)[7]. To limit the discussion, let us focus on the class of crystalline materials and more specifically; metals. A chunk of crystalline material is typically a polycrystalline aggregate, which is comprised of a collection of crystals or grains, having ***distributions*** of sizes and rotation or orientation of the crystal lattices relative to each other. These distributions have unique statistical features that could enable the forensic fracture feature differentiation process. For example, grain sizes typically show log-normal distribution[8-13], with the ratio of the diameter of the largest grain in a distribution to the median diameter is roughly constant, equal to 2.5 to 3[8,14].

Grain Orientation Distribution Functions[15] (ODF's) in polycrystalline aggregate are also bounded. Most structural metals have a cubic crystal structure which exhibit the highest

degree of crystal lattice symmetry and thereby reduces the complexity of the orientation-relationship between grains through symmetry operations. A orientation mismatch between two crystal lattices defines the crystal boundary or the grain boundary[16-22]. A single grain would be defined as a collection of crystals with a similar orientation or misorientation below a set value of 3^{o}-5^{o} [23-27]. Orientation of each grain is characterized by means of three parameters such as the Euler angles. The ODF's are graphically represented by what is termed in material science; the pole plot[26]. In addition, most of structural materials experience final stage of mechanical and thermal processing that leaves significant crystalline distortion, or texture. In this process, the grains within the bulk of the specimen undergo local rotation to realign the most favorable slip or deformation direction with the direction of the macroscopic loading. As a result, the material becomes highly textured, with majority of the gains exhibiting almost the same crystallographic orientation. Each finishing process (e.g. rolling, extrusion forging, stamping) presents unique ODF's that could be utilize to screen the main class of the material[26]. The combined measurements, characterizations and utilizations of data library from earlier studies for the microstructural details of the material will provide many statistical features that could enable the forensic fracture matching process.

Fracture Process Scale

The fracture surface topography is dependent on the microstructure details of the material and the dynamics of the fracture event. The size of deformed features on the fracture surface is associated with patterns of local primary shear bands that form in areas defined by the size and spacing of individual dendritic (solidification) features that arrest the crack extension[28]. Crack initiation and growth depends on the crystallographic structure,

orientation and the plastic strain amplitude to failure.[29,30] Any method to characterize fracture surfaces needs to capture and model the interplay between the external load imposed length scale and the microstructural feature scale.

In mechanics, mathematical descriptions of fracture depend on establishing a representative material element[32-33] to approximate the material microstructure (cf. Fig.A 1). The material resistance to fracture which includes crack nucleation, crack coalescence, and the growth of short cracks is dependent on the complex and random microstructure (e.g. distribution of defects and grain oreintation[33]). For example, statistics of cracks in concrete exhibit features of Brownian motion[34]. The statistics of crack growth varies with the average grain diameter. Intergranular crack trajectories are more predictable since the crack surface coincides with grain boundaries. To the contrary, transgranular fracture is more complex due to a larger set of possible crack trajectories[34]. Accordingly, the topographic features scale and amplitude on the fracture surface would be very different for the two cases. Moreover, these features are very different between ductile (associate with rough surface at the micron and submicron scale, dominated by dimples and void coalescence) and cleavage fracture (much smooth appearance that spans many microns upto the gain scale). Characterization of the interplay between the distribution patterns of the gain size and orientation, and the fracture process should provide features of the fracture surface topography that can be utilized in the forensic fracture match.

Current Study

This study focuses on ascertaining that the fracture surface topology of different fractured segments is dependent on the ratio of the local stress state (i.e. load severity) vs. the local material resistance to fracture. The material resistance to fracture is dictated by the microstructure (grain size, grain boundary angles, and defect population; e.g. pores and inclusions) as well as the intrinsic local material chemistry and bond strength. These complex microstructure details, combined with the characteristics of the applied load, have the potential to provide a quantitative *signature* of the fracture surface in the form of spatial feature size and orientation. While physical characterization of material properties and processing conditions will guide the selection of appropriate data, careful attention must also be paid to the unavoidable "*noise*" associated with material variability and measurement error; validation of our method will require experimental evaluation to demonstrate that such variation is small enough to lead to potentially acceptable error rates.[35]

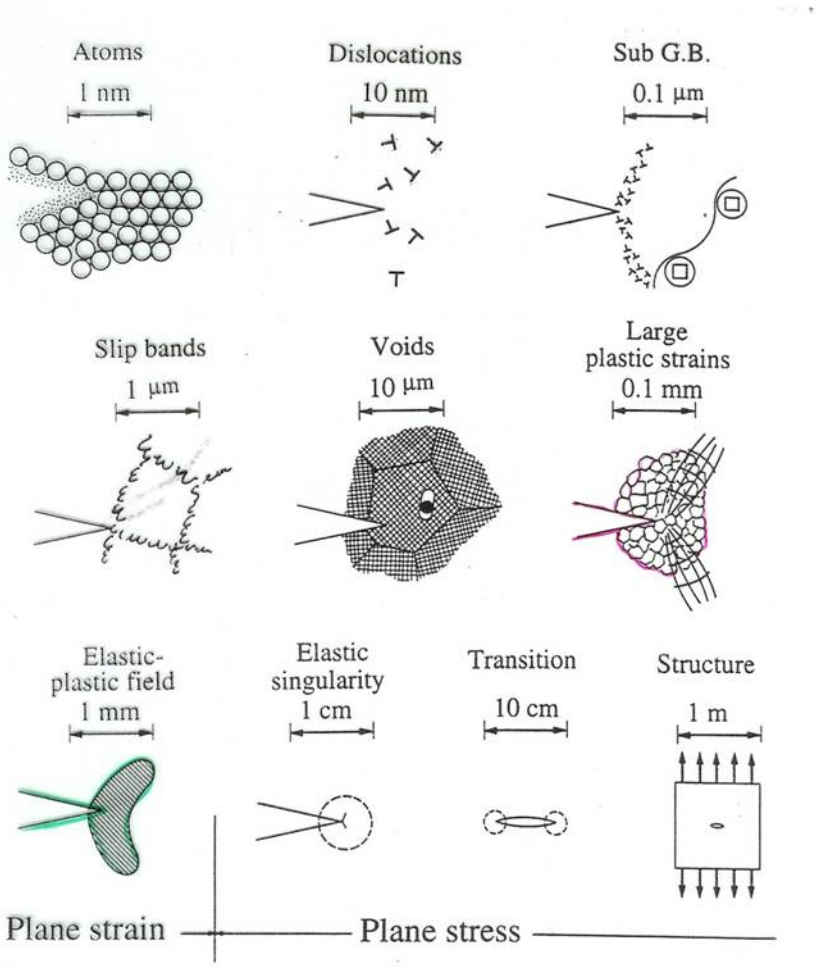

Figure A.1: Interaction of the crack trajectory with the material length scale, viewed at a progressively coarser scales (McClintock, 1966)[6]

We will establish a quantitative *figure of merit* and acceptance/rejection criteria to be used in the comparison. The bases of the procedure are derived from the quantitative details of the material microstructure and the established concepts of fracture process zones in the field of fracture mechanics[2]. We will focus on gathering data representative of the material grain size distribution, and the void and dimple scale of the fracture process zone. Primary efforts of identifying the population would focus initially on metal fragments, especially those alloys and processing conditions for typical knifes and pry tools. In principle, the

proposed method is very general and can be applied to metallic, polymeric, glass and ceramic fragments, especially since it can be *self-calibrated* for each new class of materials to establish the base-line and will be discussed in later section. The proposed framework should help determine the likelihood that certain broken pieces would/not match the broken piece found at the crime scene.

A.2 IMPLEMENTATION METHODOLOGY

Data Collection Protocol

The pairs of fracture surfaces will be analyzed by a standard non-contact 3D optical interferometer (Zygo-NewView 6300). The interferometer provides a height resolution of 20nm and spatial inter-point resolution of 0.45μm. Surface height topographic maps will be acquired from the pairs of fracture surfaces. These height topographic maps will be quantized using spectral analysis as shown in Fig.A 2 for a broken chisel fracture surface. From the 3D contour heights (Fig.A 2(a)) one can generate the spatial height distribution in any desired direction (Fig.A 2(c)). For illustration, the spectral analysis of such 2D data set (depicted on Fig.A 2(d)) has the potential to provide a discriminating distribution of features on the surface. For example, the river mark within the lower portion of Fig.A 2(a) yields characteristic spectra on Fig.A 2(d). Other feature characteristics are also marked.

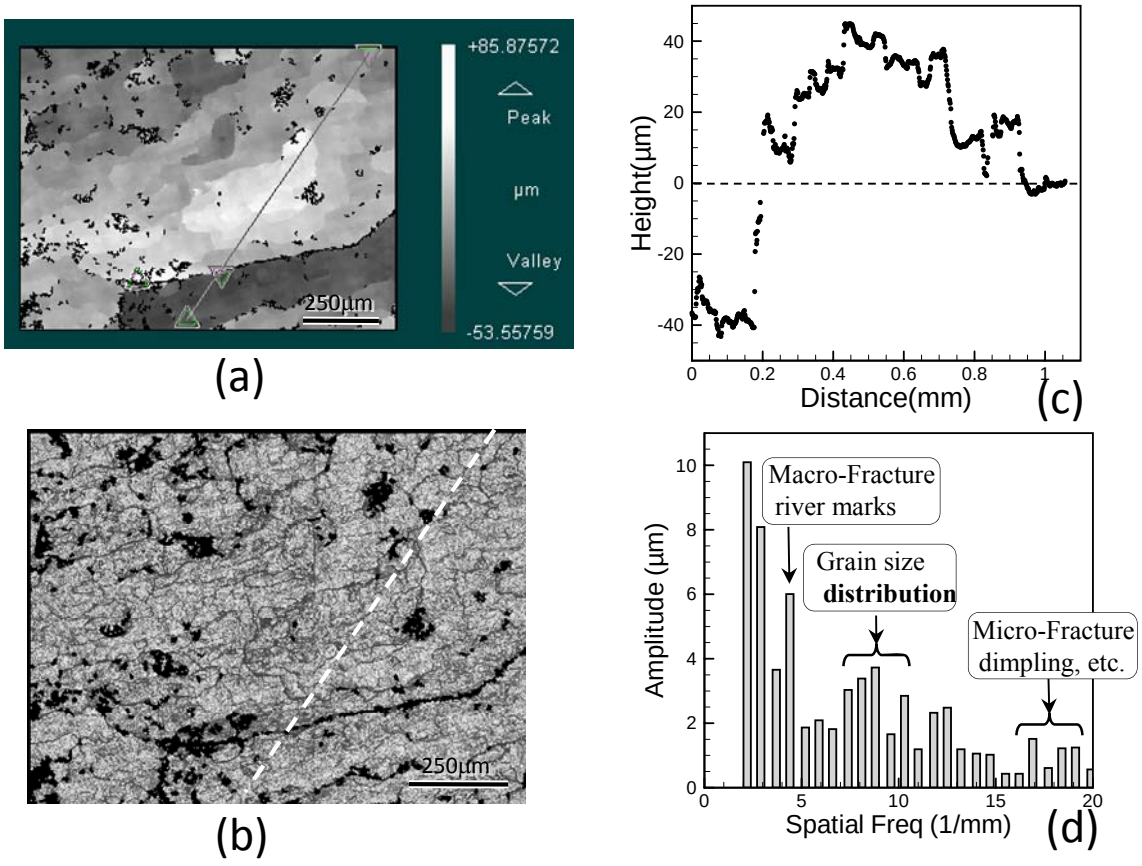

Figure A.2: Typical set of measurement and analysis for fractal surface showing the unique signature of the fractal surface. (a) 3D height map. (b) 2D rendering. (c) 1D line profile. (d) 1D spectral description.

Here we will explore the suitable mathematical expressions to identify the proper scales (or frequencies) for comparison as well as the degree of similarities and the associated error. There is a trade-off between the size of the imaging window, which defines the largest wavelength to be detected (low-frequency cut-off), and the spatial resolution, which defines the smallest wavelength to be detected (high frequency cut-off). These two limits are dictated by the mesoscopic fracture surface features (100-1000µm), the microstructure grain size (1-100µm) and the details of the fracture mechanism (0.05-1µm). A balance between the two

frequency limits is achieved by selecting the proper magnification for the high frequency limit (fraction of the Nyquist frequency), then perform multiple image stitching to target the lowest required frequency.

Analysis and Physical Matching

The goal is to provide a basis for rendering an interpretation of whether or not the two fracture fragments originate from the same source (i.e. same body and same loading events). This process will be carried out by identifying the degree of similarity between the two spectra of the fracture pairs, and developing a representative measure for the degree of matching. The proposed uniqueness of this approach stems from matching three to five (or more) independent features on the surface; each of them has its own distribution and quality of the match. Each of these features would ascertain different issues for individuality of the match. For example, the river mark signature and the micro-fracture dimpling or cracking would ascertain that the pair of surfaces belongs to the same fracture event. The analysis will be carried out in the following steps.

Image Pair Alignment: On the plane of the crack surface, there are two principal axes, the crack propagation direction and the direction of the crack tip. The images of the fracture pairs ought to be aligned relative to this reference axes. In addition, for highly textured samples, there would be preferential misconstrue direction (direction of rolling or extrusion) that has to be considered in alignment. Otherwise, angular phase difference between the wave-numbers (a vector representation of 3D frequency spectra) will occur. Therefore, care should be given in visually aligning the fracture surface pairs, before acquiring the 3D

surface topography. Then, a macroscopic autocorrelation of the real 3D profile will be applied to the image pair to maximize their relative rotational alignment. Alternatively, a 2D spectral analysis would be utilized wherein a 2D vector wave number will be employed in the autocorrelation to find the angular separation between the two images.

Image Pair Spectra Analysis: Each feature on the fracture surface has a population. For example, grain size is not single frequency content within the spectrum as indicated in Fig.A 2(d), but rather has a distribution. The first step of the analysis will be to identify the scale of the significant features on each image pair and their populations. For a pair of fractured surfaces, the population of these features will incorporate relevant information about the physical processes present at each length-scale. After calculating the spectra of each pair of images, each spectrum will be divided into multiple radial and angular zones. The segmented angular sectors for the frequency range (-15^{o}, 195^{o}) will represent the entire data set, since the frequency space representation exhibit inversion symmetry (Fig.A3). The radial segments are to be chosen to reflect the physical process scales. The centroid of the wave number for each sector is evaluated as $\mathbf{K}(r,\theta)$. The difference of the corresponding wave numbers are evaluated and averaged over the angular sector to provide a correlation measure, $\tilde{\mathbf{K}}(r)$, for the match at different frequency (r is the radial distance on the frequency spectra, (1/mm)), $\tilde{\mathbf{K}}(r) = \sum_{\theta=1}^{n} \left| \left(\tilde{\mathbf{K}}_1(r,\theta) - \tilde{\mathbf{K}}_2(r,\theta) \right) \Big/ 0.5\left(\tilde{\mathbf{K}}_1(r,\theta) + \tilde{\mathbf{K}}_2(r,\theta) \right) \right|$.

Self Calibrated Matching: The correlation measure $\tilde{\mathbf{K}}(r)$ cannot be utilized to decide on the match, without understanding the distribution of the population for each of the fracture

and the microstructure length scales. To establish a reference, several pairs of images are recorded on the same fracture surface (one side only of the fracture pair) but at different spatial locations. The resulting correlation measure $\tilde{\mathbf{K}}_{ref}$ will approximately represent the statistical distribution of many of the material and fracture process scales. The proposed self-calibrated indices should greatly strengthen the methodology, and perhaps make it applicable across a wider variety of materials. Efforts will focus on the error rate in establishing this reference level. It will be carried out by finding the variance in the comparison indices for ten different pairs of images acquired on the same side of the fracture surface, and their variance relative to the other side. It should be noted that the established variance of the baseline should not be mistaken as directly address population-wide errors, as will be discussed in later sections.

Once a baseline is established, $\Delta\tilde{\mathbf{K}}(r) = \tilde{\mathbf{K}}(r) - \tilde{\mathbf{K}}_{ref}$ can be considered as a *figure of merit* for the match at each frequency. By definition, $\Delta\tilde{\mathbf{K}}(r)$ can have positive and negative values. Figure 4 shows the figure of merit distribution, $\Delta\tilde{\mathbf{K}}(r)$ as a function of the fracture surface topography frequency, relative to the established reference level, $\tilde{\mathbf{K}}_{ref}$ (marked by the dashed line), for two cases, a matched pair and a pair of the same class. Also shown on the same curve, the variation of $\Delta\tilde{\mathbf{K}}_{ref}(r)$ relative to the established reference at the frequency of interest to show the spread in the base line representation. For the matched fracture pair, Fig 4(a), most of the $\tilde{\mathbf{K}}(r)$ values fall within the reference level. For the same class pair, Fig 4(b) frequencies that represent the material microstructure are the only match.

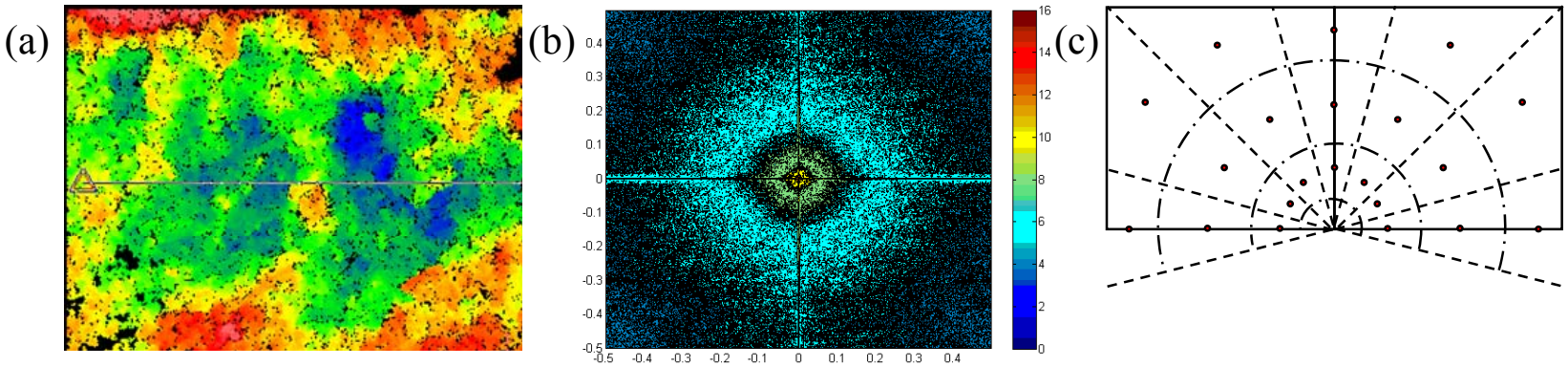

Figure A.3: (a) Color render of the surface topography. (b) Corresponding frequency spectra. (c) Division of the spectra to different sector for comparison based on the fracture process physical scales. (Data is from a 3point bend fracture of SS-440C steel).

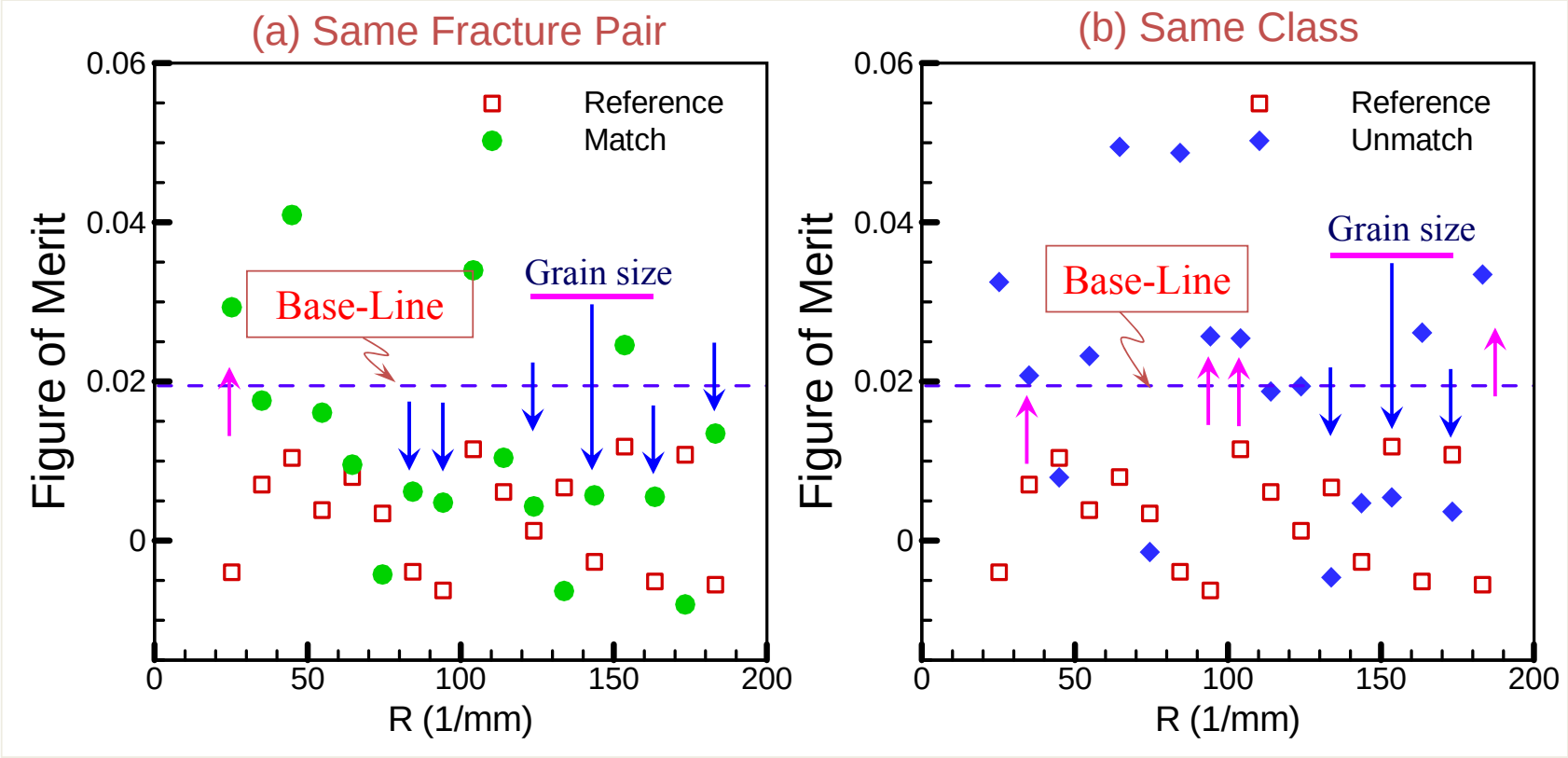

Figure A.4: Establishment of base line for the Figure of Merit comparison through self calibration (red symbols) (a) A fracture pair. (b) A pair of the same class but not matched.

A.3 CASE STUDY

A typical knife and tool material (SS-440C) with a precursor notch will be examined under defined loading conditions in a flexural 3-point bend test (Fig.A 5(a)). This configuration provides an unstable crack propagation to mimic the cleavage fracture, commonly found in a crime scene. Two paires of SS440C samples broken in two different directions, the first pair is P29-W08 and the second pair is K23-S01; the third surface is an unrelated copper fracture surface with the same grain size.

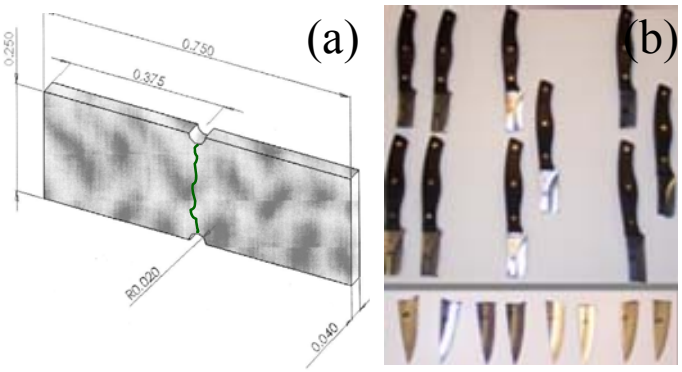

Figure A.5: Set of samples to be tested in the first phase. (a) Controlled 3 point bend fracture. (b) Set of representative knife breaking; *provided by J. Morris*.

For each sample, there is a statistical variation of the frequency. The amplitude of the difference grows with frequency. Thus we have to establish this band and its dependence on the frequency by comparing pairs of images on the same fracture surface, at each magnification as shown in Fig.A6. After establishing the base line of each surface, we compare their difference frequency relative to the base line of one for the surfaces for each pair of images. By analyzing a matched pair (P29-W08) and unmatched pair (with copper, but similar grain size), the established figure of merit indicates that the best accretive domain

is the range up to f=200(1/mm) or features of 5 microns or higher. This was quite clear on the 10x magnification (Fig.A7 a). At higher magnifications (Fig.A7 b), the trend is not clear at all since the signal to noise ratio is very low. Thus it appears that around 10x produces the best assertive field of view. Matching also may not be at all frequencies. Also, the analysis shows that the fracture surface topography provides assertive differentiation for the class (same type of knife material) and individual characteristics matches (fragment surface "should" belong to the same fracture event). To study the same materials but different events, a comparison is conducted for two different pairs: W08-P29 constitute match and W08-S01 constitute no match. The Fig.A8 shows that despite the similarity at 4 frequecey bands (same material, and similar fracture type), the W08-S01 still has more differences from the base line band than the W08-P29 pair. Thus we can formulate a figure of merit for the entire spectra to show the quality of the match.

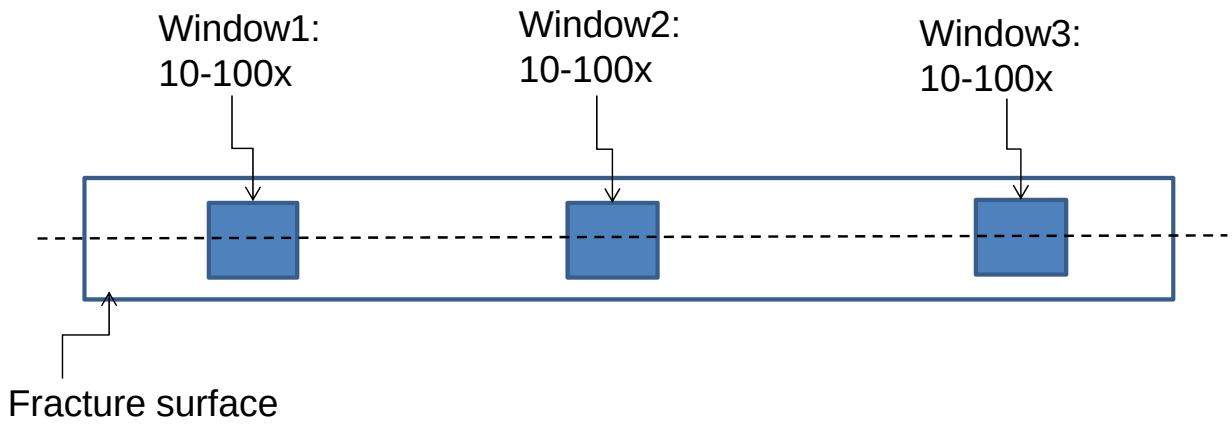

Figure A.6: Multiple comparing pairs of images taken on the same fracture surface, at different magnifications

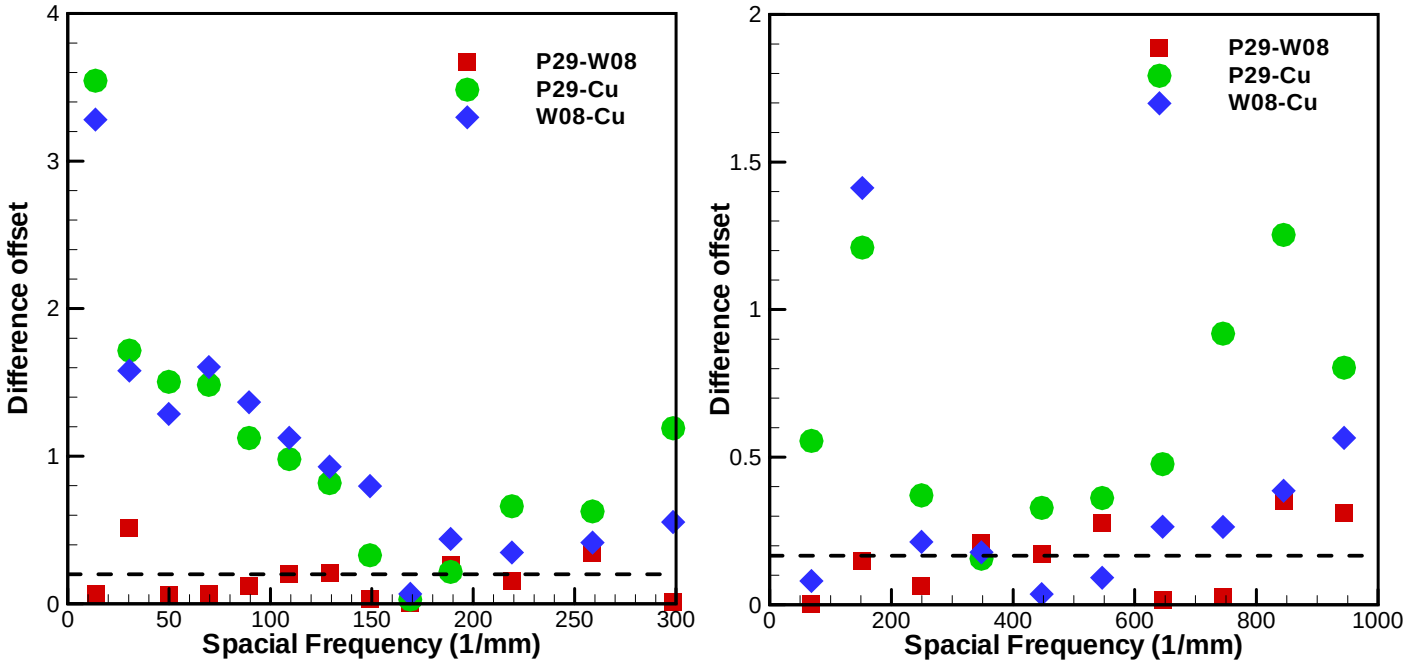

Figure A.7: The best accretive domain is range up to f=200 (1/mm) and it is clear on 10x Mag. (a) 10x magnification (b) 50x magnification.

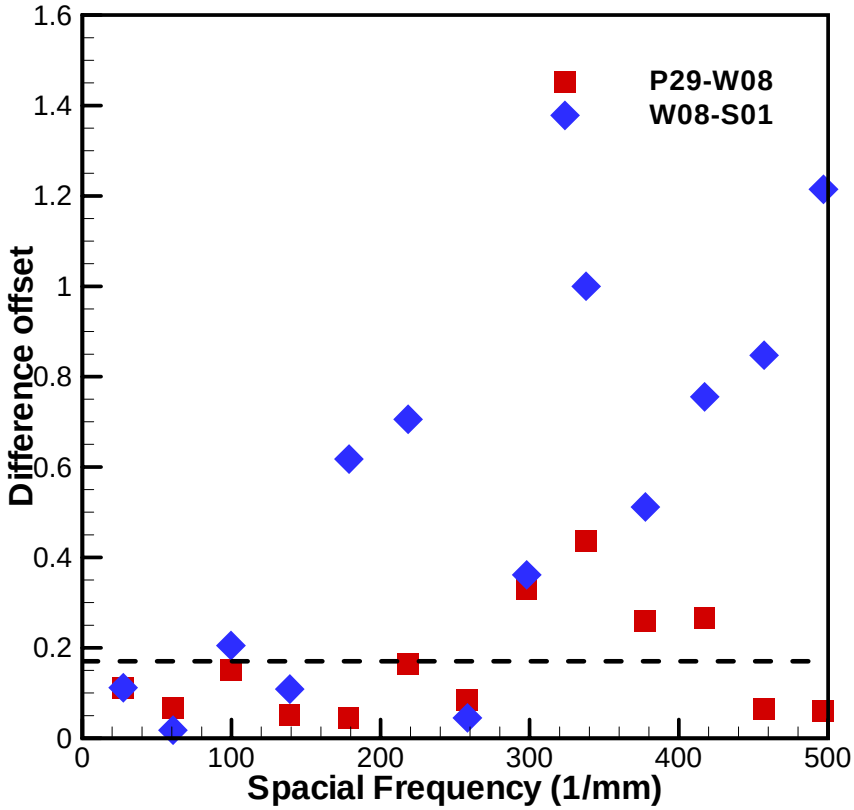

Figure A.8: The comparison of same material, but different events.

A.4 FUTURE WORK

Crime Scene Samples: Other material specimens, representing common crime scene pieces, will be surveyed such as wider range of irregular geometries. These include non-planar fractures, and those associated with significant bending of the fracture surface; commonly associated with breaking of knives and pry tools. Our forensic scientist collaborator will select and provide these sets of samples, similar to those depicted on Fig.A 5(b) of irregularly broken knives. These samples are provided with coded unmatched pairs for blind study. The specimen sets will be also matched through established protocol at the

forensic lab for comparison. Once the technique reaches maturation level, it would be also applied to fragments of broken plastics ceramic and glass with radial or circular topographic features on the fracture surface.

Technical Challenges and Image Limitations: Several issues or challenges remained to be addressed throughout the protocol development. First, trials will address placement of specimens for measurement of the fractures with wide macro-variation in surface features (Form factor >0.5mm), such as those associated with knife fracture with significant fracture surface curvature. The second issue is statistical significance of the known match versus the known non-match. This study will examine the size of the data set that would yield the proper surface topography population to identify each unique feature. The size of the data set expands quadratically with the required resolution. An optimization process should yield the proper size of the data set.

Analysis of Environmental and Weathering Effects: Degradation of forensic evidence over time, or exposure of an evidence to accelerated corrosive environment before being retrieved is one of the limiting factors for forensic match. The proposed 3D topographic fracture surface analysis will provide details of how ageing and environmental exposure deteriorates some of the microstructure and fracture process zone details overtime. It should be also noted that the corrosion rate is accelerated in the presence of residual stresses[39]. It has been shown that based on the iso-electric point of the corrosive environment, some wavelength on the surface can decay and others can grow (e.g. erosion of dimples and widening of crevasses). Studying the details of these factors is beyond the scope of the proposed framework, though it could be implemented in future studies.

A.5 REFERENCES

1. National Institute of Justice Report, 2009, "High-Priority Criminal Justice Technology Needs, U.S. Department of Justice Office of Justice Programs, NCJ 225375, Washington, DC 202531.

2. Sanford, R.J., 2003. Principles of Fracture Mechanics, Pearson Ed. Inc., NJ.

3. Curran, J. M., 2003, "The Statistical Interpretation of Forensic Glass Evidence," Int. Stat. Rev. 71(3):497-520.

4. Katterwe, H., 2005, "Fracture Matching and Repetitive Experiments: A Contribution of Validation," AFTE Journal 37(3):229-241.

5. M.J. Bradley, R.L. Keagy, P.C.Lowe, M.P. Richenbach, D.M.Wright, and M.A. LeBeau, 2006, "A Validation Study for Duct Tape End Matches," J. Forensic Sc., 51:504-508.

6. F. McClintock and A. Argon, 1968, Mechanical Behavior of Materials, Addison-Wesley Pub. Co, MA.

7. M.F. Ashby, D.R.H. Jones, 1981, Engineering Materials-I, Pergamon Press, Oxford

8. S.K. Kurtz, F.M.A. Carpay, 1981 "Microstructure and normal grain growth in Metals and ceramics. Part 1," J. Appl. Phys., 51(11):5725-5744.

9. M. Paulus and J.Rech, 1962, Phys. Status Solid, 2:1325.

10. H.E. Exner, 1972, International Met. Rev., 17:25.

11. P. Comte and W. Form, 1976, Practical Metallography, 13:9.

12. P. Feltha, 1957, Acta Metallogr. 5:97.

13. J. Aitchison and J.A.C. Brown, 1957, The Lognormal Distribution, Cambridge University Press, MA.

14. J. E. Burke, 1968, Ceramic Microstructures, Wiley, N.Y., Chapter 33.

15. I.V. Alexandrov et al., 1995, Modeling Simulations Mater. Sci. Eng., 3:149-159.

16. M. A. Bingham, D. J. Nordman, and S. B. Vardeman, 2009, "Modeling and Inference for Measured Crystal Orientations and a Tractable Class of Symmetric Distributions for Rotations in 3 Dimensions," (*to appear in Journal of the American Statistical Association*).

17. M. A. Bingham, S. B. Vardeman and D. J. Nordman, 2009, "Bayes One-Sample and One-Way Random Effects Analyses for 3-D Orientations with Application to Materials Science,"Preprint, Department of Statistics, Iowa State University.

18. M. A. Bingham, B. K. Lograsso and F.C. Laabs, 2008 "Statistical Analysis of the Variation in Measured Crystal Orientations Obtained through Electron Backscattered Diffraction," UltraMicroscopy, (*Submitted*).

19. B.K. Lograsso, T.A. Lograsso and R. Glamm, 2008, "Application of a Crystal Orientation Method for Matching Surfaces along a Fracture Line," IMECE2008-6763, ASME Congress.

20. M. A. Bingham, D. J. Nordman, and S. B. Vardeman, 2008, "A Tractable Class of Distributions for Rotations in 3 Dimensions and Some Applications to Measured Crystal Orientations," Preprint, Department of Statistics, Iowa State University.

21. O. Engler, 1994, "Statistics, evaluation and representation of single grain orientation measurements," *Materials Science Forum*, vol. 157-162, pp. 259-274.

22. B. L. Adams, 1997, "Orientation imaging microscopy: Emerging and future applications," *Ultramicroscopy*, vol. 67, pp. 11-17.

23. F. J. Humphries, 2001, "Review Grain and subgrain characterization by electron backscatter diffraction," *Journal of Materials Science*, 36:3833-3854.

24. J. K. Mackenzie, 1957, "Some statistics associated with the random disorientation of cubes," *Biometrika*, 44:205-210.

25. J. K. Mackenzie, 1958, "Second paper on statistics associated with the random disorientation of cubes," *Biometrika*, 45:229-240.

26. V. Randle, 2003, Microtexture determination and its applications, 2nd ed., pp. 113-114. London: Maney for The Institute of Materials, Minerals and Mining.

27. A. Morawiec, 2004, Orientations and rotations: Computations in crystallographic textures, New York: Springer, pp. 135.

28. D.C. Hofmann, J. Suh, A. Wiest, G. Duan, M, Lind, M.D. Demetriou, and W.L. Johnson, 2008, "Designing metallic glass matrix composites with high toughness and tensile ductility," Nat. Let., 451:1085 -1089.

29. J. Polak, 2007, "Mechanisms and Kinetics of the early fatigue damage in crystalline materials," Mat. Sc. Eng. A 468-470: 33-39.

30. R. O. Ritchie, J. F. Knott and J. R. Rice, 1973, "On the relationship Between Critical Stress and Fracture Toughness in Mild Steel," J. Mech. Phys. Solids, 21:395-410.

31. M. O. Starzewski, 2006, "Material Spatial Randomness: From Statistical to representative volume element," Probabilistic Engineering Mechanics 21:112-132.

32. G.C. Sih and R. Jones, 2003, "Crack Size and speed interaction characteristics at micro-, meso- and macro-scale," Theoretical and Applied Fracture Mechanics, 39:127-136.

33. K. Sobczyk, 2008 "Morphological complexity of material microstructures: From stochastic models to fracture estimation," Probabilistic Engineering Mechanics 23:44-455.

34. S.R. Arwade and M. Popat, 2009, "Statistics and Probabilistic Modeling of Simulated Intergranular Cracks," Probabilistic Engineering Mechanics, 24:117-127.

35. L.S. Chumbley, M. Morris, J. Craft, J. Kreiser, J., C. Fisher, S. Davis, D. Faden, J. Kidd, L. Genalo, 2009, "Validation of Toolmark Comparisons Obtained Using a

Quantitative, Comparative, Statistical Algorithm," Journal of Forensic Sciences, to appear.

36. National Research Council, 2004, Weighing Bullet Lead Evidence, National Academies Press, Washington, D.C.

37. S.B. Vardeman, and J.M. Jobe, 1998, Statistical Quality Assurance Methods for Engineers, John Wiley and Sons, New York.

38. L. Engel and H. Klingele, 1981, An Atlas of metal damage: surface examination by scanning electron microscope, Prentice-Hall, Englewood Cliffs, N.J.

39. K.-S. Kim, J. A. Hurtado, and H. Tan, 1999, "Evolution of a Surface-Roughness Spectrum Caused by Stress in Nanometer-Scale Chemical Etching," Phy. Rev. Let., 83:3872-3875.